63
65

Experimental Investigation of Reversed Flow in a Compressor Cascade

by

James P. Carneal

Thesis submitted to the Faculty of the Virginia Polytechnic Institute and State University in partial fulfillment of the requirements for the degree of

MASTER OF SCIENCE

in

Mechanical Engineering

APPROVED:

Walter F. O'Brien

W. F. O'Brien, Chairman

C. L. Dancey

C. L. Dancey

H. L. Moses

H. L. Moses

June, 1990

Blacksburg, Virginia

Experimental Investigation of Reversed Flow in a Compressor Cascade

by

James P. Carneal

W. F. O'Brien, Chairman

Mechanical Engineering

(ABSTRACT)

An experimental investigation of reversed flow performance characteristics in a compressor cascade was conducted. The purpose was to gain a fundamental understanding of reversed flow in a compressor blade cascade, and to determine the effects of stagger angle and angle of attack on the reversed flow behavior in the cascade.

Tests were conducted at two blade configurations, one to simulate reversed flow in a compressor rotor and one to simulate reversed flow in a compressor inlet guide vane. Three stagger angles were tested for each configuration with an absolute angle of attack range from 70 to 130 degrees. The investigation included total and static pressure measurements upstream and downstream of the cascade as well as blade surface measurements.

Aerodynamic performance parameters were presented for a reversed flow cascade. Comparison of corrected total pressure loss curves suggested that blade rows

of a compressor subjected to reversed flow may be treated as nearly equal loss producers. A comparison was made between total pressure loss coefficients from this investigation and experimental compressor performance. The total pressure loss coefficients compared favorably in magnitude and curve shape.

ACKNOWLEDGEMENTS

The author wishes to thank his advisory committee, Professors C. L. Dancey, H. L. Moses, and W. F. O'Brien, chairman of the committee. Dr. O'Brien's guidance was extremely helpful in completing this investigation.

The Mechanical Engineering Department is recognized for providing financial assistance and laboratory space.

The author thanks his friends who made life fun during the hours that he was not working.

Finally, the author thanks his parents for encouraging him throughout his entire life.

TABLE OF CONTENTS

LIST OF ILLUSTRATIONS vii

LIST OF TABLES ix

LIST OF SYMBOLS x

1.0 INTRODUCTION 1

2.0 LITERATURE REVIEW 4

3.0 BACKGROUND 10
- 3.1 SURGE CYCLE AND ROTATING STALL 10
- 3.2 REVERSED FLOW DISCUSSION 12
- 3.3 CALCULATION OF REVERSED FLOW ANGLES 15
- 3.4 PERFORMANCE PARAMETERS 18

4.0 EXPERIMENTAL EQUIPMENT 23
- 4.1 WIND TUNNEL 24
- 4.2 TEST SECTION 26
- 4.3 AIRFOILS 28
- 4.4 INSTRUMENTATION 30
  - 4.4.1 ANEMOMETRY EQUIPMENT 30
  - 4.4.2 PRESSURE MEASUREMENTS 31
  - 4.4.3 TRAVERSING MECHANISM 32
  - 4.4.4 DATA ACQUISITION SYSTEM 33

5.0 PROCEDURES AND METHODOLOGY 34
- 5.1 WIND TUNNEL AND TEST SECTION 34
- 5.2 PRELIMINARY DATA COLLECTION 35
- 5.3 SPLIT FILM INVESTIGATION 36
- 5.4 PRESSURE INVESTIGATION 36
- 5.5 DATA REDUCTION 39

6.0 RESULTS 41
- 6.1 ORGANIZATION OF RESULTS PRESENTED 41
- 6.2 NEGATIVE STAGGER ANGLE - GROUP I 43
- 6.3 POSITIVE STAGGER ANGLE - GROUP II 44

7.0 CALCULATED RESULTS FOR CASCADE PERFORMANCE 64

8.0 DISCUSSION OF RESULTS 82
8.1 SIMPLIFIED CASCADE MODEL 82
8.2 NEGATIVE STAGGER ANGLE (GROUP I) 87
8.3 POSITIVE STAGGER ANGLE (GROUP II) 90
8.4 DISCUSSION OF MASS AVERAGED LOSS ω_3 92
8.4.1 EXPERIMENTAL COMPARISON 92

9.0 CONCLUSIONS 98

10.0 RECOMMENDATIONS 100

REFERENCES 101

APPENDIX A 102

APPENDIX B 107

APPENDIX C 107
C.1 Split Film 109
C.2 5-Hole Probe 114

LIST OF ILLUSTRATIONS

Figure 1. Stall Cell Propagation 2
Figure 2. General Shape of a Stage Pressure Characteristic 8
Figure 3. Compressor Surge Cycle 11
Figure 4. Compressor Stage in Normal Forward-Flow Operation 13
Figure 5. Compressor Stage in Reversed Flow Operation 14
Figure 6. Definitions for Negative Stagger Angle Tests 16
Figure 7. Definitions for Positive Stagger Angle Tests 17
Figure 8. Cascade Measurement Locations 19
Figure 9. Experimental Wind Tunnel 25
Figure 10. Test Section Geometry 27
Figure 11. Airfoil Profile 29
Figure 12. Probe Position Variance 38
Figure 13. Individual Test Result, SA=-25, AOA=80 46
Figure 14. Individual Test Result, SA=-25, AOA=90 47
Figure 15. Individual Test Result, SA=-25, AOA=110 48
Figure 16. Individual Test Result, SA=-36.5, AOA=81.5 49
Figure 17. Individual Test Result, SA=-36.5, AOA=91.5 50
Figure 18. Individual Test Result, SA=-36.5, AOA=121.5 51
Figure 19. Individual Test Result, SA=-45, AOA=115 52
Figure 20. Individual Test Result, SA=-45, AOA=125 53
Figure 21. Individual Test Result, SA=25, AOA=-70 54
Figure 22. Individual Test Result, SA=25, AOA=-105 55
Figure 23. Individual Test Result, SA=36.5, AOA=-81.5 56
Figure 24. Individual Test Result, SA=36.5, AOA=-96.5 57
Figure 25. Individual Test Result, SA=36.5, AOA=-106.5 58
Figure 26. Individual Test Result, SA=36.5, AOA=-121.5 59
Figure 27. Individual Test Result, SA=45, AOA=-95 60
Figure 28. Individual Test Result, SA=45, AOA=-110 61
Figure 29. Individual Test Result, SA=45, AOA=-120 62
Figure 30. Individual Test Result, SA=45, AOA=-130 63
Figure 31. NSA Station 2 Mass Averaged Total Pressure Loss 67
Figure 32. NSA Station 3 Mass Averaged Total Pressure Loss 68
Figure 33. NSA Station 2 Mass Averaged Turning Angle 69
Figure 34. NSA Station 3 Mass Averaged Turning Angle 70
Figure 35. NSA Blade Tap Normal Force Coefficient 71
Figure 36. NSA Momentum Equation Normal Force Ceofficient 72
Figure 37. NSA Axial Velocity Ratio 73
Figure 38. PSA Station 2 Mass Averaged Total Pressure Loss 74
Figure 39. PSA Station 3 Mass Averaged Total Pressure Loss 75

Figure 40. PSA Station 2 Mass Averaged Turning Angle 76
Figure 41. PSA Station 3 Mass Averaged Turning Angle 77
Figure 42. PSA Blade Tap Normal Force Coefficient 78
Figure 43. PSA Momentum Equation Normal Force Ceofficient 79
Figure 44. PSA Axial Velocity Ratio 80
Figure 45. NSA Station 2 MATPL versus Reynolds Number 81
Figure 46. Simplified Cascade Model; A_2/A_1 is Small 83
Figure 47. Simplified Cascade Model; A_2/A_1 is Large 84
Figure 48. Cascade Area Ratio 86
Figure 49. Corrected Loss Coefficient ω_3 Results 93
Figure 50. Comparison of Loss Predictions with Experimental Results 97
Figure 51. Variable Contraction Nozzle 103
Figure 52. Variable Contraction Nozzle Details 104
Figure 53. Variable Contraction Nozzle Boundary Layer Results 106
Figure 54. Split Film Probe Angles 111
Figure 55. Split Film Calibration Curve 1 112
Figure 56. Split Film Calibration Curve 2 113
Figure 57. 5-Hole Probe Sketch 115
Figure 58. Five Hole Total Pressure Calibration Curve 117
Figure 59. Five Hole Static Pressure Calibration Curve 118

LIST OF TABLES

Table I. Summary of Experiments and Results 42
Table II. Summary of Calculated Results 66

LIST OF SYMBOLS

A	area
AVR	axial velocity ratio
c	blade chord
Cp	coefficient of pressure
C_{Fn}	coefficient of force normal to blade chord
F	force
H	cascade height
L	cascade length
p	pressure
s	blade spacing
u	component of velocity in x-direction
v	component of velocity in y-direction
U	compressor wheel speed
V	absolute velocity
W	relative velocity
y	traverse position

GREEK CHARACTERS

α	angle of attack
$\alpha_{1,2}$	absolute flow angle
β	relative flow angle
γ	stagger angle
ε	turning angle
θ	angle
ρ	density
ψ	coefficient
ω	mass averaged total pressure loss

SUBSCRIPTS

1	station 1, approximately 2 chords upstream of the cascade center line
2	station 2, 0.543 chord downstream of the cascade center line
3	station 3, imaginary downstream location with uniform velocity and pressure profiles
c	compressor
corr	corrected for compressor wheel speed
m	mean

n	normal to blade chord
p	pressure
ps	pressure side static condition
s	static condition
ss	suction side static
t	total condition
x	component of velocity in the x-direction
y	component of velocity in the y-direction

1.0 INTRODUCTION

When a compression system is operated at low mass flow rates, the high angles of attack on the blades (due to off design conditions) cause instabilities that lead to blade stall and compression system stalling or surge. Stall is undesirable due to the cyclic loading and unloading of the blades, along with the decreased compressor efficiency which leads to decreased engine performance.

Blade stall results in two phenonema, rotating stall and surge. Rotating stall exists when a blade passage is stalled, causing blockage of the passage. The blockage causes the adjacent blade to develop a high angle of attack, thereby stalling that blade, while unstalling the previous passage, as seen in Figure 1. As this process continues, the stalled passage moves or 'rotates' around the annulus of the compressor at approximately 0.5 times the compressor's rotational speed. Rotating stall is undesirable since the compressor will find steady state operation in the stalled region (of the performance curve) without going back to normal operation. There is always some recovery hysteresis with rotating stall. That is, the compressor flow control (throttle) must be opened to a larger value than that which produced rotating stall to allow recovery to normal operation. In extreme cases, an engine with the compressor in rotating stall must be shut down and restarted to regain normal operation.

Surge is a different type of phenomenon usually involving the entire compressor instead of just a few blade passages. A surge is characterized by the fluid oscillating between forward flow (normal and rotating stall operation) and reversed flow in the

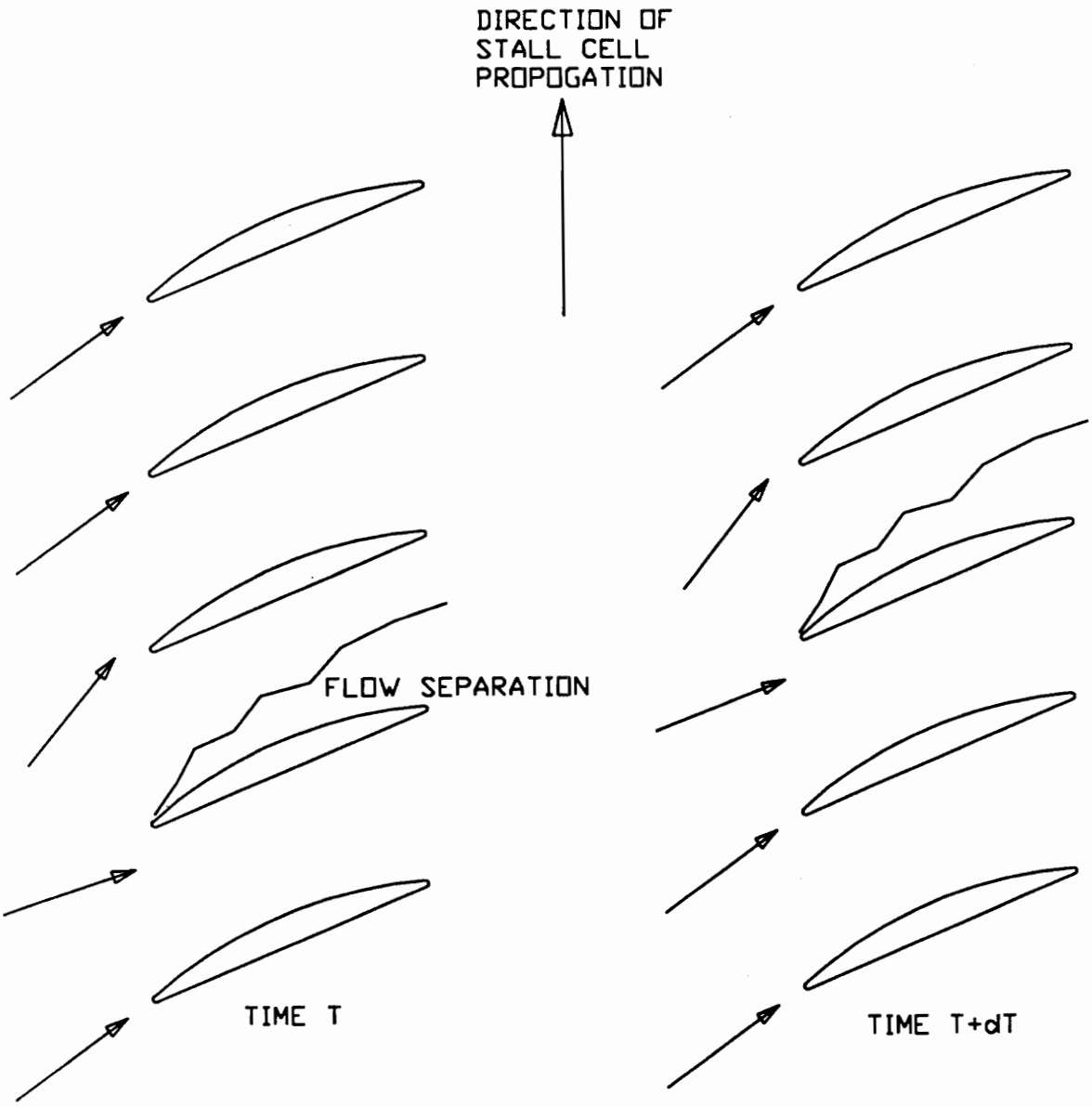

Figure 1. Stall Cell Propagation

compressor. If a compressor surges, it does not find steady state operation. Instead, it cycles between normal operation and stalled operation, which allows recovery if the cause of surge is eliminated. For this reason, surge is the more desirable of the two instabilities.

Several methods involving computer models have been developed to simulate compressor system operation in stall. These models use steady state performance characteristics generated from theory, compressor tests, or cascade tests of blades to simulate unsteady performance. Although there is available information about the normal and stalled forward flow regions, reversed flow characteristics are usually estimated for use in the models.

To support modelling efforts, a study of the reversed flow characteristics of a linear compressor cascade was done. The investigation included the testing of a simulated rotor and inlet guide vane subjected to reversed flow. Results for stagger angles of 25, 36.5 and 45 degrees, angles of attack from -130 to -70 degrees, and 3 Reynolds numbers at the maximum, median and minimum angles of attack are included. The results of the study are presented, and conclusions are deduced for the effect of stagger angle and Reynolds number on reversed flow behavior.

2.0 LITERATURE REVIEW

The 2 different types of compressor stall were first recognized and classified by Emmons[1] as rotating stall and surge.

In an effort to understand the underlying principles behind this phenomena, attempts were made to describe stall and surge mathematically. Greitzer[2] developed a non-linear mathematical model that accurately predicts rotating stall and surge performance. The model consisted of a plenum and throttle connected downstream of a compressor. He used non-linear equations coupled to a compressor characteristic curve found by experiments described below. The results showed that the response is strongly dependent upon the shape of the compressor characteristic curve as well as the non-dimensional B parameter. This parameter is defined as:

$$B = \frac{U}{2a}\sqrt{\frac{V_p}{A_c L_c}}$$

where U is the compressor wheel speed, a is the speed of sound, V_p is the plenum volume, A_c is the compressor flow-through area, and L_c is the effective length of the compressor. The B parameter relates the geometry of the compressor to the possibility of the compressor operating in rotating stall or surge. Depending on the magnitude of the B parameter, it is predicted that a compressor will operate in rotating stall or surge. If the B parameter is large, then the compressor will surge. Stall will occur when the B

parameter is relatively small. Another important result from this work concerns surge behavior of a compressor. In surge, the predicted compressor response follows the quasi-steady reversed flow characteristic curve closely for a B value of 5, but does not follow the curve closely for a B value of 1.58. The present research was designed to produce information about the quasi-steady reversed flow characteristic.

Greitzer[3] also presented experimental results done on a three stage axial flow compressor using a plenum and a throttle downstream for comparison with the model. From this experimental work, he generated a steady state compressor characteristic for positive and negative non-dimensional axial velocity (NDAV). Other observations from this work included:

1) There was a major discrepancy at near zero flow that is not well understood.

2) Reversed flow is very effective at generating losses.

3) In deep surge, the compressor spends a significant part of the cycle in reversed flow.

From these results it is evident that the reversed flow characteristic is an important part of stall and surge modeling. Since Greitzer[3] inferred the reversed flow compressor characteristic from the measured plenum pressure, it is thought that the major discrepancy near zero flow is a result of his chosen reversed flow characteristic. Therefore to obtain better modeling of a compressor, fundamental information on reversed flow characteristics is needed.

Turner and Sparks[4] generated complete characteristics of a single stage axial fan, which consisted of an inlet guide vane, a rotor, and a stator. Reversed flow was created

by blowing flow backwards through the stage. Separated flow was observed to occur in the rotor and inlet guide vane, while the flow left the stator trailing edge approximately parallel to the camber line.

Gamache[5] noted that a complete set of measured steady state characteristics including stalled and reversed flow for a multistage compressor did not exist in open literature, and that detailed experiments on reversed flow had never been performed or reported. He proceeded to research axial compressor reversed flow by running experiments on a three stage axial flow compressor operated to surge and stall. In addition to presenting a detailed study of the compressor's operation in stall and surge, he found that prediction of the forced response of a compression system can be drastically altered by changing the shape of the assumed steady state compressor reversed flow characteristic.

Koff[6] researched axisymmetrically stalled flow performance using a reversed flow characteristic generated by Turner and Sparks[4]. Koff proposed a reversed flow characteristic based on the fact that in axisymmetric reversed flow, the compressor acts as a throttling device, producing a pressure drop. He modeled reversed flow using a two dimensional cascade of thin plates as compressor blades. Koff observed that predictions for 2-D reversed flow agreed with measurements from a single stage compressor, but were less accurate in a 3 stage compressor. He concluded that the reversed flow portion of the characteristic is important, and that higher stagger angles provide a greater resistance to reversed flow.

Davis[7] created a one-dimensional, stage-by-stage compression system model that was applied to a three stage, low speed compressor and a nine stage high pressure compressor. The model used compressor characteristics that were generated from experimental data, but there was a lack of information for reversed flow characteristics. He estimated these from low speed compressor rig studies that were previously done by Gamache[5]. Using these characteristics, Davis was able to simulate surge and rotating stall in these compressors. Using experimental results from actual compressor testing, he validated the model. Needing actual stage characteristics in stalled and reversed flow, the Davis model emphasized the need for fundamental experiments with reversed flow.

The present state of the art in computer modeling of dynamic compression system behavior was recently presented by Boyer[8],et al. Boyer successfully applied a 1-D stage-by-stage modeling technique to a 10 stage compressor and successfully reproduced experimental results obtained by Copenhaver[9]. Boyer used backflow characteristics of the type shown in Figure 2. These characteristics were estimated from overall shapes obtained from compressor studies and surge transient performance. Again, reversed flow stage characteristic data were needed.

Due to the cost of testing an actual compressor rig, using computer models with stage characteristics developed with the help of wind tunnel cascade testing is desirable. Through cascade testing, a basic understanding of the flow processes is generated. Once these basic processes are better understood, improved stage performance models for compression system models can be built.

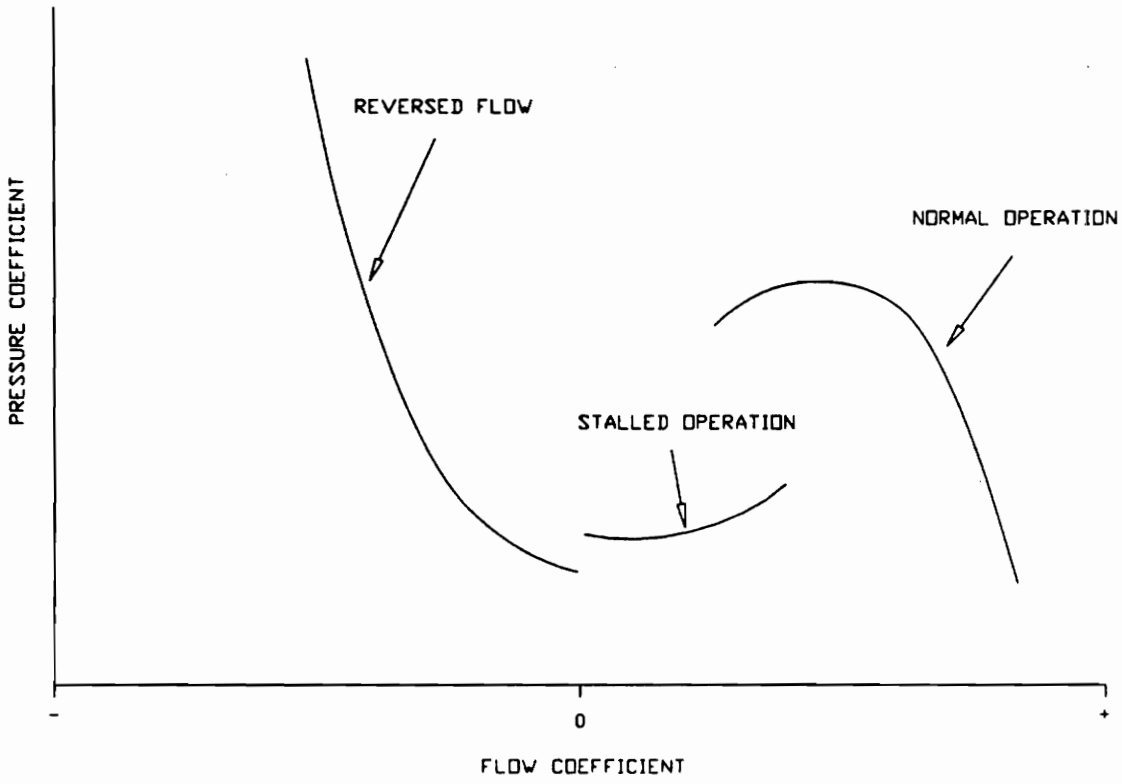

Figure 2. General Shape of a Stage Pressure Characteristic

As part of a current research effort at VPI&SU, Yocum[10] carried out a parametric study by testing a cascade in forward flow at a solidity of 1.0 and two stagger angles of 25 and 36.5 degrees. The goal was to investigate the cascade's stall and post-stall characteristics. Ainslie[11] continued this study by testing a cascade in forward flow at a solidity of 1.5 with the same stagger angles. The present investigation utilized the same cascade wind tunnel, adapted for reversed flow tests.

To further this parametric study, to understand the fundamental processes in reversed cascade flow, and to contribute to the database for reversed flow characteristics, this investigation is presented.

3.0 BACKGROUND

As noted in the Literature Review, the reversed flow characteristic curve is an important part of the overall compressor in-stall characteristic. To gain fundamental knowledge of reversed cascade flow, the test section of the low-speed compressor cascade wind tunnel at VPI&SU was set to test blades under reversed flow conditions.

In the material which follows, reversed flow is discussed in a global sense in relation to the stage characteristic and compressor operation. Equations representing relative flow in a rotor-stator system are developed to establish the test conditions for the cascade, and test procedures are described. Finally, the performance parameters for the reporting of cascade flow results are introduced.

3.1 SURGE CYCLE AND ROTATING STALL

A surge cycle is visualized as beginning on the normal operation line for a compressor, as pictured in Figure 3. Reducing the mass flow through the compressor forces operation to the left of the normal operation curve, in the stalled region. Compressor operation is then determined by the flow control, the stalled operation curve, and the dynamic response of the compression system.

If conditions are correct, the compression system may enter a surge cycle, as shown in Figure 3. Surge is a self-excited, cyclic phenomenon. Usually, reversed flow occurs for part of the cycle. The pressure-flow characteristic in the reversed flow region is very different from the forward flow characteristic. It is the subject of this thesis to examine the nature of reversed flow in a compressor cascade to develop some basis for

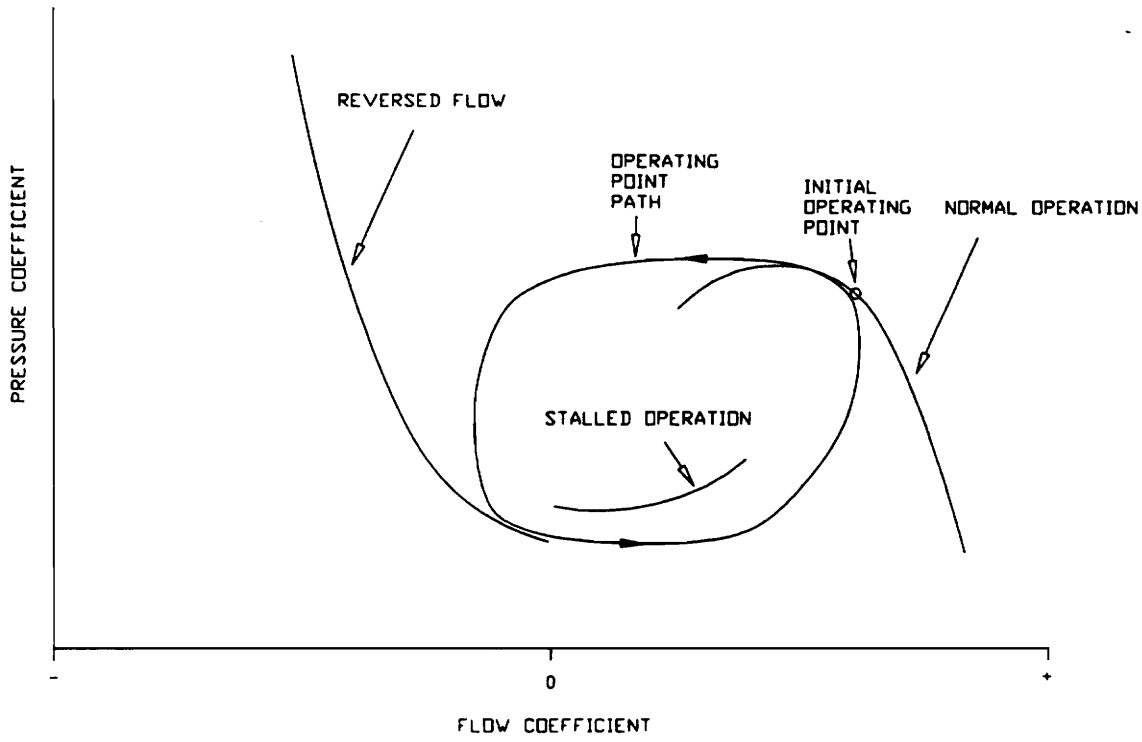

Figure 3. Compressor Surge Cycle

predicting the reversed flow characteristic.

Under other conditions, the compression system will enter stable rotating stall. In this case, the final operating point will lie near the stalled operation curve shown in Figure 3, and the compressor will be in rotating stall. While the net flow through the compressor is positive in stable rotating stall, there may be regions of locally reversed flow in the stages of the compressor.

3.2 REVERSED FLOW DISCUSSION

The arrangement of a typical compressor stage is shown in Figure 4. For normal forward-flow operation, velocity vector Vx is positive in the sense shown. Absolute velocity angles α_1 and relative angles β_1 are aligned with the blade metal angles, and operation is normal with low fluid total pressure losses.

Figure 5 shows reversed flow in the same stage. If it is assumed that reversed flow leaves the stator at approximately the stagger angle (following Turner and Sparks[4]), then the trailing edge of the rotor blade will see a relative flow W_2 at a very high angle of attack. For a range of magnitude of velocity vector V_2 in Figure 5, angle β_2 could range from 90 degrees for zero flow, to perhaps 60 degrees for a high value of backflow velocity.

For the inlet guide vane, backflow will result in negative angles of attack at the trailing edge of the vane. Assuming that velocity vector W_1 in Figure 5 is parallel to the stagger of the rotor blade, angle α_1 will range from 90 degrees to approximately 60 degrees for large backflow.

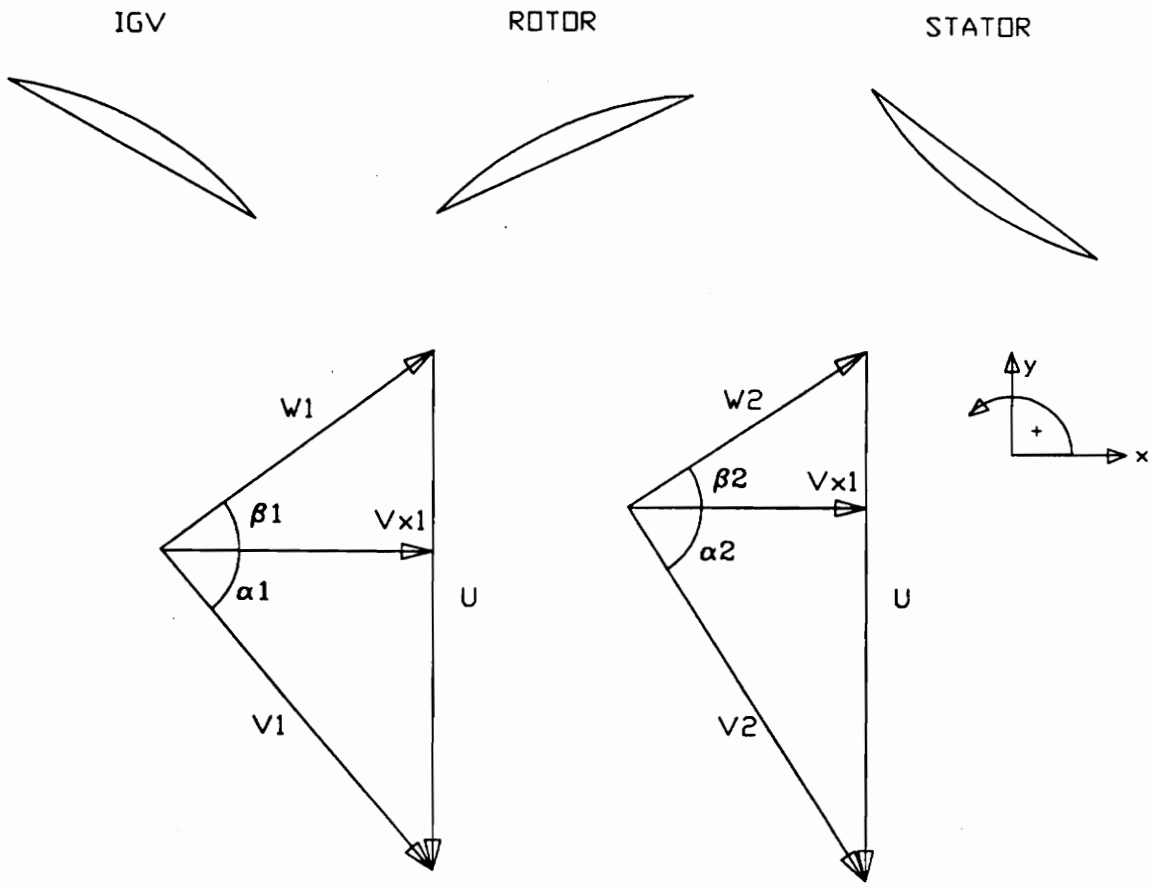

Figure 4. Compressor Stage in Normal Forward-Flow Operation

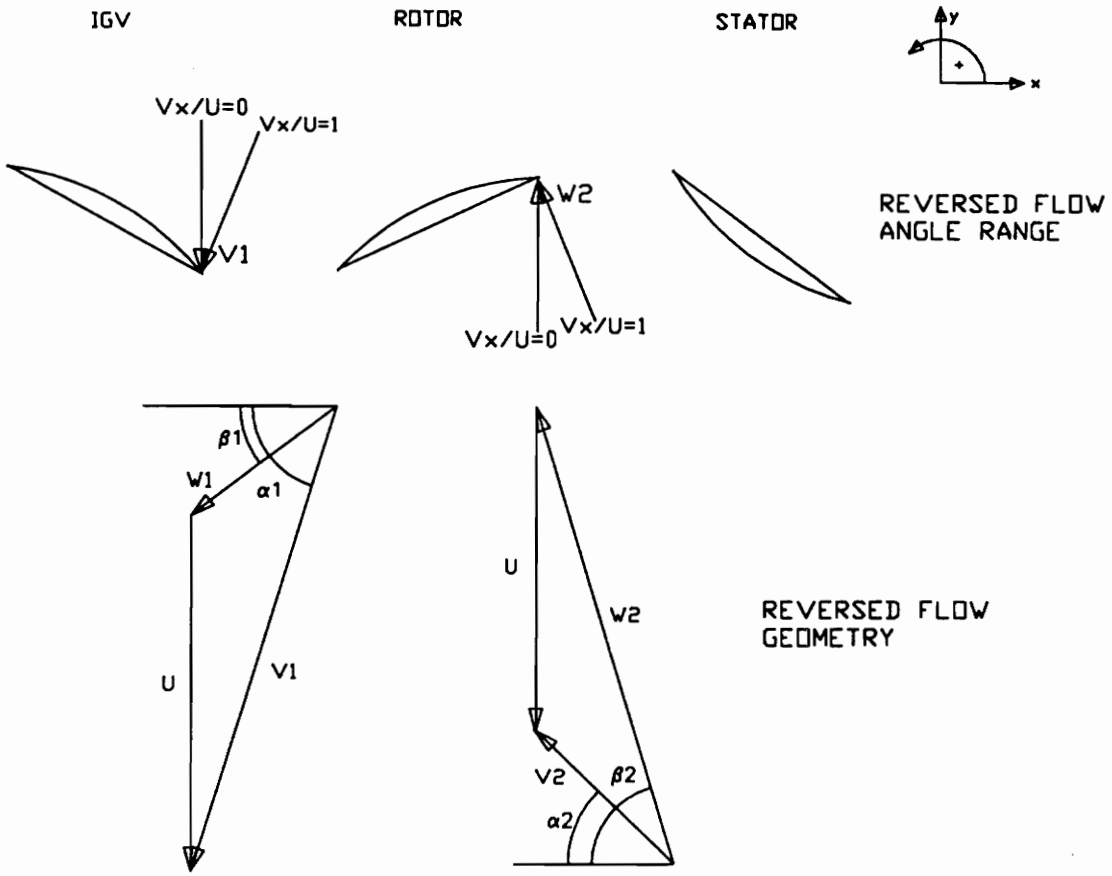

Figure 5. Compressor Stage in Reversed Flow Operation

The exact range of the reversed flow angles on the rotor and inlet guide vane blades will of course depend on the settings of the blade stagger angles and the magnitude of the backflow. It is clear from the above discussion that reversed flow will involve flow angles relative to the blades of a compressor stage ranging over very large positive and negative angles of attack.

3.3 CALCULATION OF REVERSED FLOW ANGLES

To generalize the angles tested for reversed flow, the flow angle relative to the rotor and inlet guide vane will be referred to in terms of stagger angle and angle of attack. Tests designed to investigate reversed rotor flow, seen in Figure 5, will be referred to as negative stagger angle tests with positive angles of attack. Tests of inlet guide vane reversed flow, seen in Figure 5, will be referred to as positive stagger angle tests with negative angles of attack. Reversed flow over a stator vane would be similar to the rotor flow.

For a given range of backflow and following the geometry of Figure 5, a value of the relative velocity vector W_2 can be determined. With vector W_2 and stagger angle γ, the reversed flow angle of attack α can be calculated using the geometry defined in Figure 6. Similarly, calculations of the angle α for the inlet guide vane may be made with the knowledge of flow vector V_1 and stagger γ, following Figure 7.

A cascade test to examine reversed flow would thus involve setting the blades so that the flow approached from the trailing edge of the blades, at the angles of attack defined by the above discussion in Figure 6 and Figure 7. Since reversed flow involves

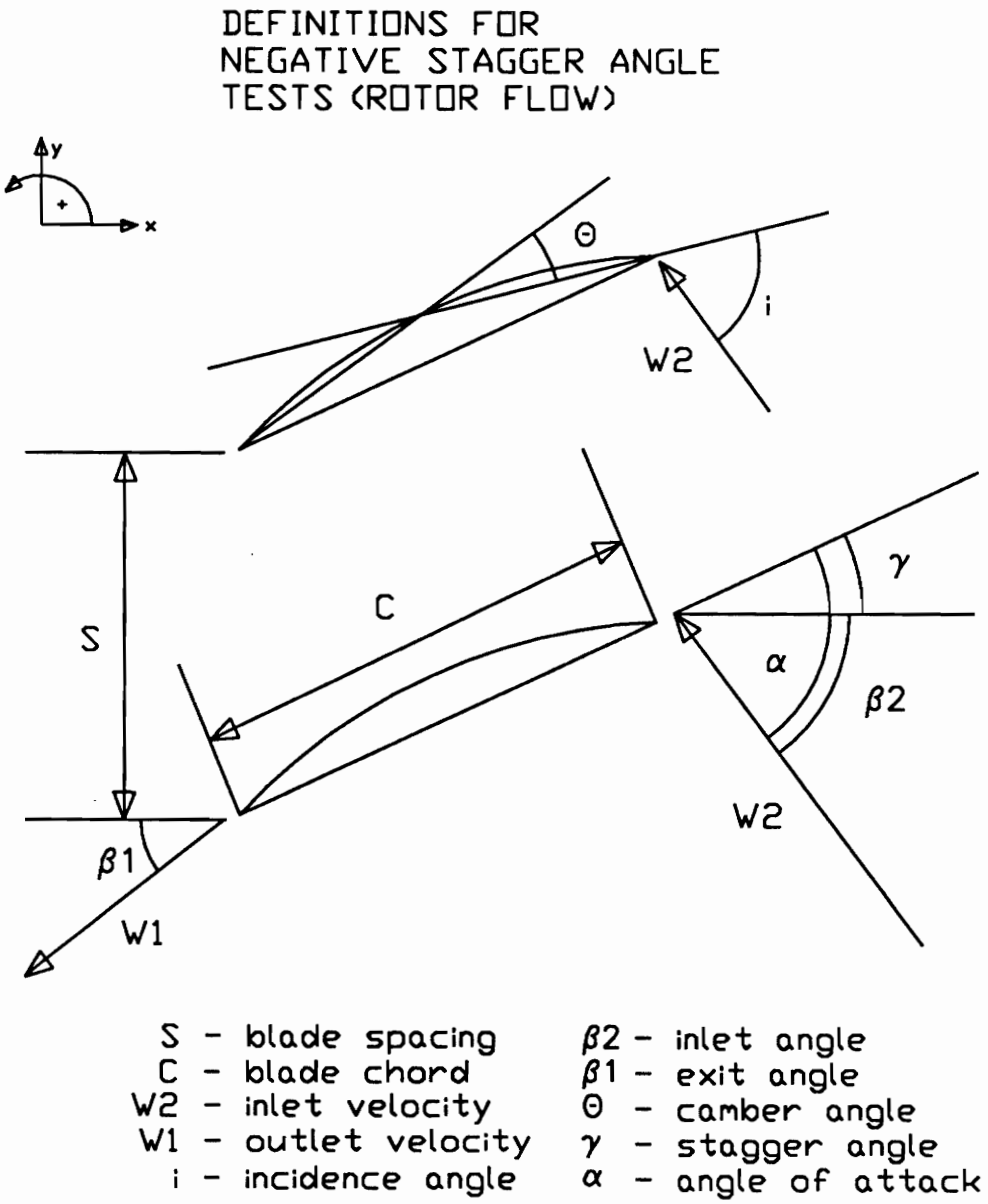

Figure 6. Definitions for Negative Stagger Angle Tests

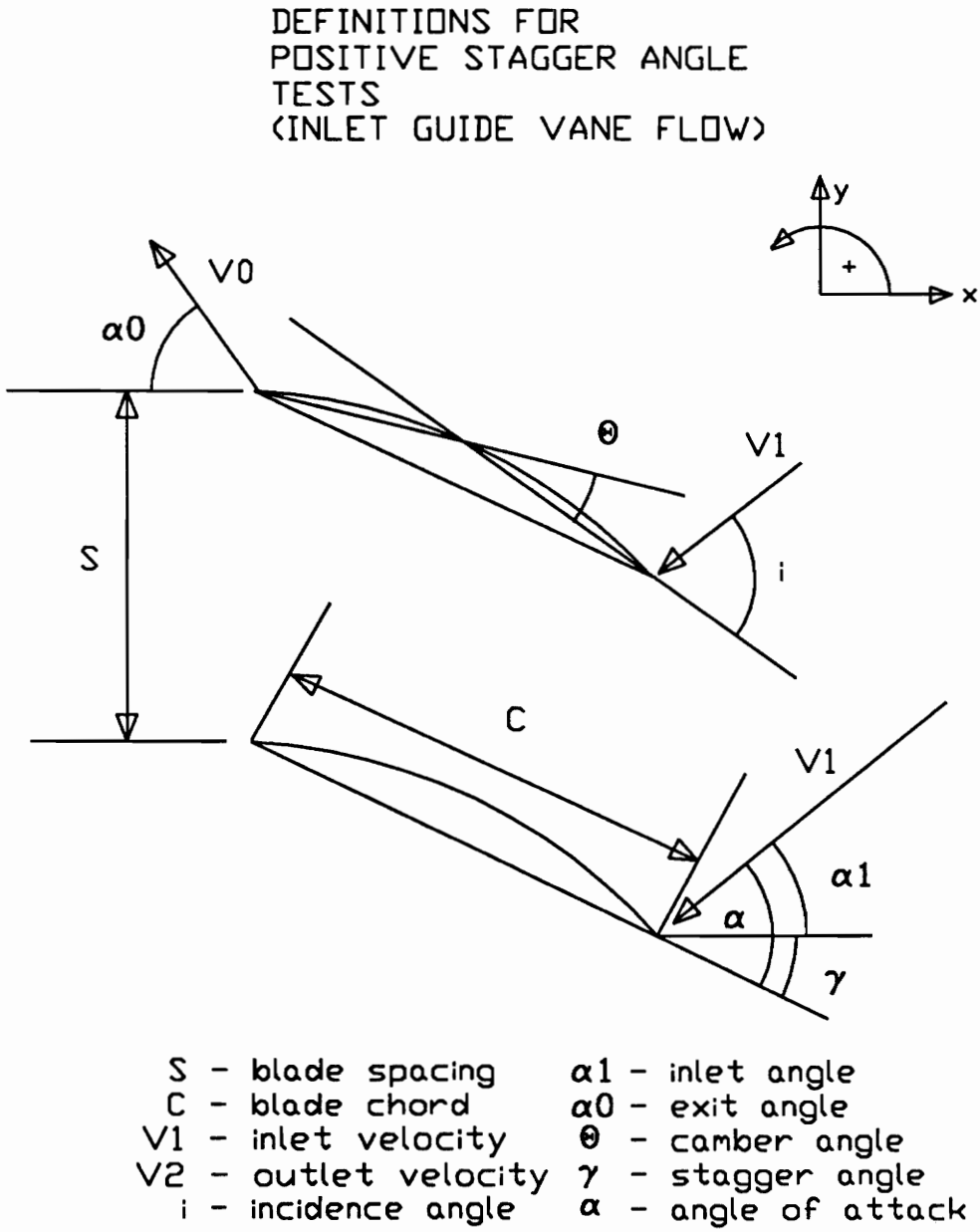

Figure 7. Definitions for Positive Stagger Angle Tests

uncertain flow behavior with separation and high losses, the range of flow angles tested should be extended beyond those calculated.

This investigation is organized into two groups. Group I includes negative stagger angles with positive angles of attack. Group I tests simulate conditions found in the rotor and stator in reversed flow. Group II includes positive stagger angles with negative angles of attack. Group II tests simulate conditions found in an inlet guide vane in reversed flow.

3.4 PERFORMANCE PARAMETERS

The investigation of cascade aerodynamics requires the definition of performance parameters and locations. Referring to Figure 8, station 2 is the location 0.543 chord downstream of the cascade. Station 3 refers to the point where flow has mixed sufficiently so that the pressure and velocity profiles are uniform. In subsequent equations, the letters u and v refer to the velocity components in the x and y directions, respectively.

For pressure measurements, a non-dimensional quantity expressing pressure is defined as:

$$C_p = \frac{p_{t_1} - p}{p_{t_1} - p_{s_1}}$$

where p is the pressure measured (total or static), p_{t1} and p_{s1} are the station 1 total and static pressures, respectively.

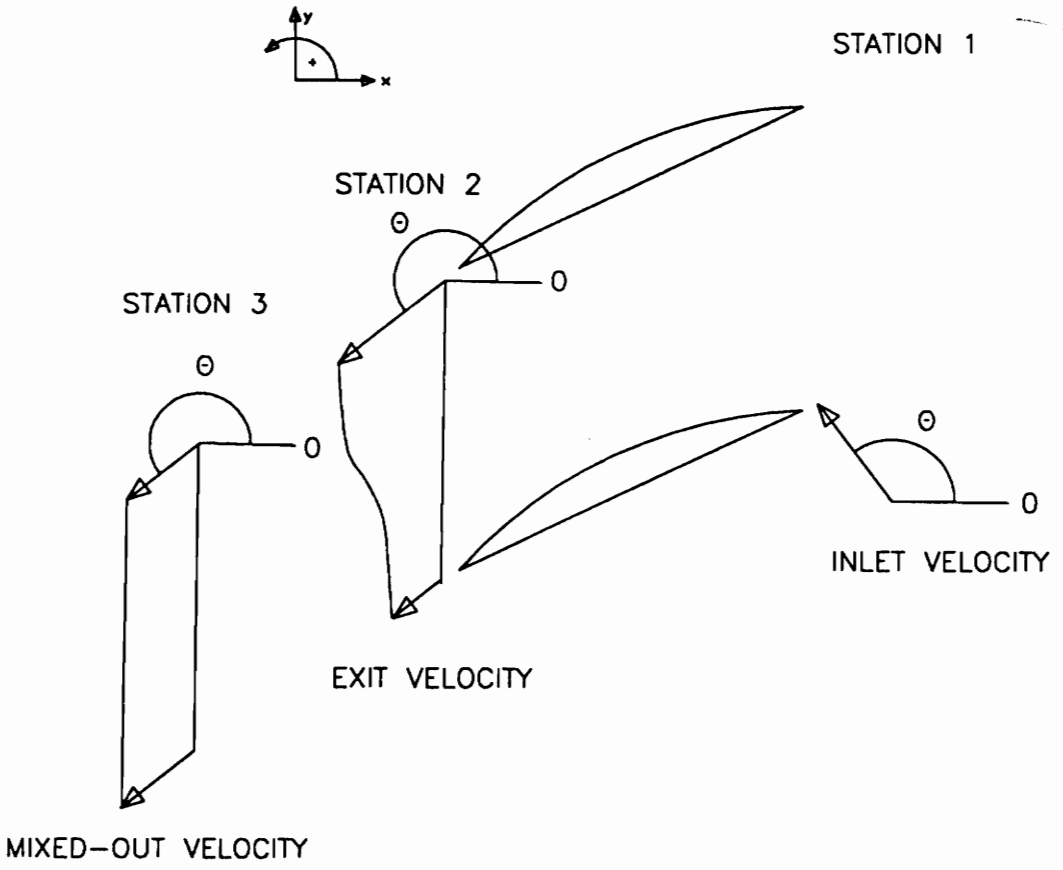

Figure 8. Cascade Measurement Locations

Mass averaged total pressure loss at station 2 is defined as the average total pressure loss from the inlet to the cascade to the measurement location at station 2 and is given by:

$$\omega_2 = \frac{\int_0^1 \left(\frac{p_{t1} - p_{t2}}{p_{t1} - p_{s1}} \right) u \, d\left(\frac{y}{s}\right)}{\int_0^1 u \, d\left(\frac{y}{s}\right)}$$

where y/s is the non-dimensionalized traverse coordinate.

Station 3 mass averaged total pressure loss is defined as the average total pressure loss from the inlet to the cascade to the point where the velocity and pressure profiles are uniform at station 3 and is stated:

$$\omega_3 = C_{p_{s3}} + \left(\frac{u_3}{V_1}\right)^2 + \left(\frac{v_3}{V_1}\right)^2$$

where C_{ps3} is derived from the momentum equation as:

$$C_{p_{s3}} = \int_0^1 C_{p_{s2}} \, d\left(\frac{y}{s}\right) + 2.0\left[\frac{1}{a}\int_0^a \frac{u_2}{V_1} \, dy\right]^2 - 2.0\left[\frac{1}{a}\int_0^a \left(\frac{u_2}{V_1}\right)^2 dy\right]$$

and:

$$u_3 = V_{x2} \qquad v_3 = \frac{1}{u_3 s}\int_0^s u_2 v_2 \, dy$$

Mass averaged turning angle at station 2 is the average angle the flow is turned at station 2. It is defined as:

$$\varepsilon_2 = \alpha_1 - \alpha_2$$

where:

$$\alpha_2 = \tan^{-1}\left(\frac{\int_0^s u_2 v_2 dy}{\int_0^s u_2^2 dy}\right)$$

Once the flow is mixed out, the Station 3 mass averaged turning angle is defined:

$$\varepsilon_3 = \alpha_1 - \alpha_3$$

where:

$$\alpha_3 = \tan^{-1}\left(\frac{v_3}{u_3}\right)$$

and, as before,

$$u_3 = V_{x2} \qquad v_3 = \frac{1}{u_3 s}\int_0^s u_2 v_2 \, dy$$

The axial velocities at stations 1 and 2 are not equal due to the boundary layer growth in an incompressible cascade. A measure of this phenomenon is the axial velocity ratio, as:

$$AVR = \frac{V_{x2}}{V_{x1}}$$

where:

$$V_{x2} = \frac{1}{s}\int_0^s u_2 \, dy$$

Normal force coefficient is the force on the blade in the normal direction to the blade. This force is generated by turning the flow and the resulting pressure differentials, and can be calculated from the static pressure taps on the blades as well as from the momentum equation. From the blade pressure taps, the normal force coefficient is:

$$C_{F_n} = \int_0^1 (C_{p_{ss}} - C_{p_{ps}}) \, d\left(\frac{x}{c}\right)$$

where C_{pss} is the blade tap suction side static pressure coefficient and C_{pps} is the blade tap pressure side static pressure coefficient.

From the momentum equation:

$$-F_x + \int_0^s (p_1 - p_2)\, dy = \rho \int_0^s \left(u_2^2 - u_1^2\right) dy$$

$$-F_y = \rho \int_0^s (u_2 v_2 - u_1 v_1)\, dy$$

$$C_{F_n} = \frac{F_y \cos\gamma - F_x \sin\gamma}{\frac{1}{2}\rho V_1^2 c}$$

4.0 EXPERIMENTAL EQUIPMENT

A variety of experimental equipment was used to complete this study. All of the equipment is briefly described, since details are given in preceding theses to this investigation, which are referenced.

4.1 WIND TUNNEL

The wind tunnel, shown in Figure 9, was designed and built by Tkacik[12]. It is the open circuit type, and has a conical air intake with a filter for removing dust in the atmosphere. The air intake is connected to a vortex damper which throttles the flow, allowing a range of flow velocities at the nozzle exit. The vortex damper throttles an Aerovent model 630 BIA centrifugal blower which is belt driven by a 15 HP 3-phase AC motor. The blower-motor has a capacity of 5.66 cubic meters per second with a 203 mm H2O pressure rise. The 0.321 square meter blower exit is attached to an 8 degree half angle diffuser having a length of 1.829 meters, leading to the 1.22 square meters settling section. Here the flow is straightened by a honeycomb section consisting of approximately 8000 cells, each having a diameter of 17.7 mm and measuring 76.2 mm in length. The flow is also conditioned by three screens to give uniform velocity and turbulence profiles spanning the cross-sectional area of the diffuser section. The diffuser section exits to two nozzle sections. The first nozzle contracts from 1.22 to 0.686 square meter in a 0.609 meter length. The second nozzle further contracts to the area of 0.09362 square meters, 304.0 mm high by 308.0 wide. To test the extreme angles required by reversed flow, another contraction section was added to provide for the effective cascade

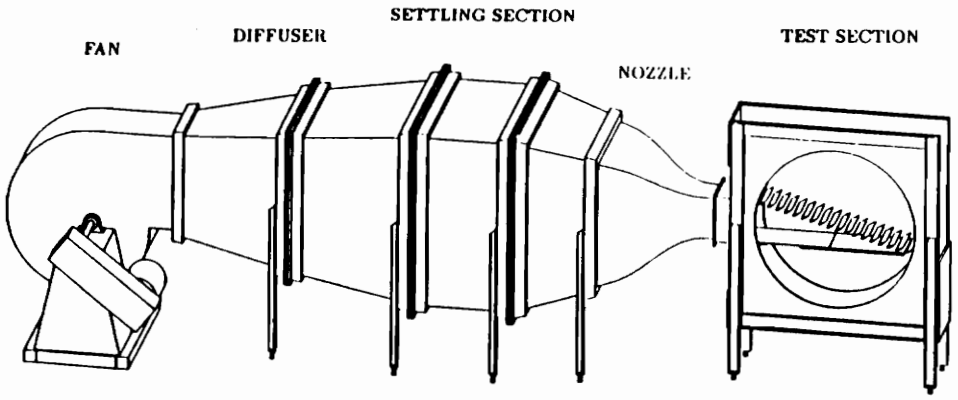

Figure 9. Experimental Wind Tunnel

height generated by setting the cascade at high angles of attack. This contraction section is referred to as the third nozzle. As can be seen in Figure 10, the effective height (H) is the cosine of the flow inlet angle (β_2) times the length of the cascade. At the maximum flow inlet angle, 90. degrees, the height would be zero, which is not practical for tests. Therefore the maximum flow inlet angle tested was 85 degrees giving a height of 79.69 mm with a cascade length of 0.914 meters.

The third nozzle was constructed to allow a variable height ranging from 0 to 237.3 mm. It incorporates 2 sheets of 0.812 mm thick aluminum cut to the shape of the second nozzle, inserted into it, and anchored. The ends of the sheet in the second nozzle were smoothed with putty and covered with a thin film to minimize the possibility of creating boundary layer separation. About midway, the sheets were rigidly attached to the second nozzle. The design is detailed in Appendix A.

Boundary layer tests were run when the third nozzle was set to an effective height of 79.69 mm. The boundary layer thickness was found to be 15.24 mm which leaves 49.21 mm of uniform flow in the center of the duct. The test measurements were made in the center 26.56 mm of the duct, leaving 11.32 mm between the edge of the boundary layer and the test area.

4.2 TEST SECTION

The test section was designed to allow for virtually any combination of stagger angle and angle of attack. For varying stagger angle, the blades rotate about their spanwise axis. The blades are mounted on two plexiglass disks that measure 1.22 meters

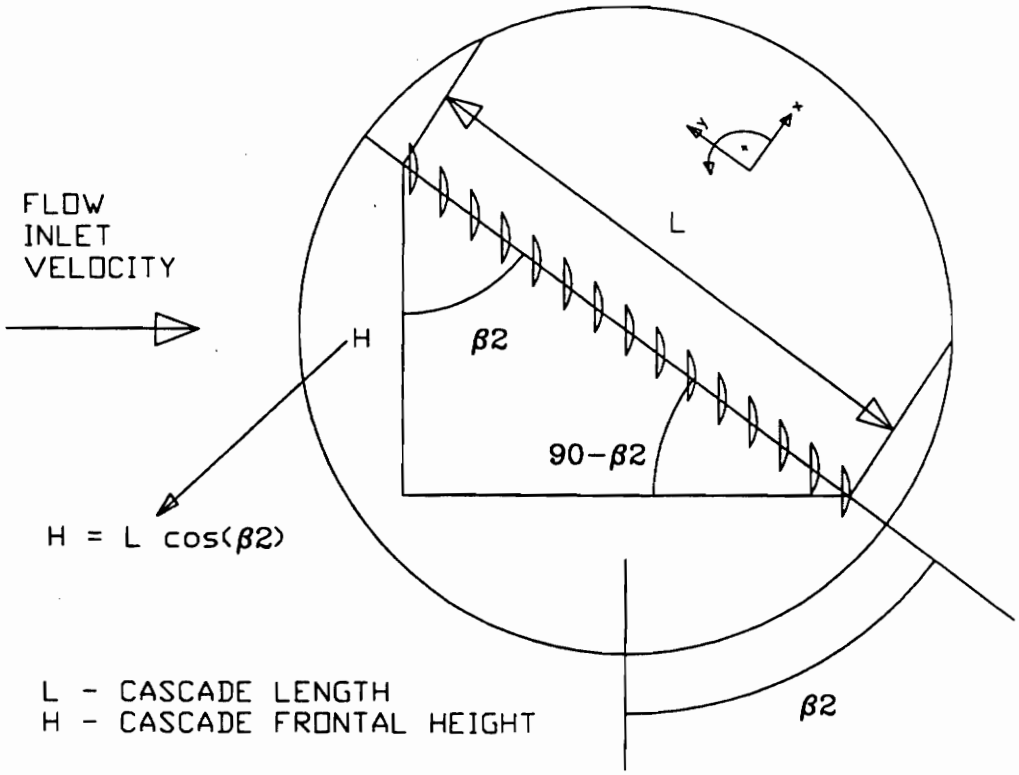

Figure 10. Test Section Geometry

in diameter and 12.7 mm thick. These disks are mounted on a plywood carrier that allows the disks to rotate, thereby setting the angle of attack. The plywood carrier has flow inlet angles inscribed upon it, and the disks have pointers to allow easy angular measurement.

To connect the third nozzle to the test section, movable walls were designed by Yocum[9]. These walls are constructed of plexiglass, are self supporting, and seal off the area between the third nozzle and the actual cascade from air leakage. Since the pressure of the accelerated flow from the wind tunnel is below atmospheric, leakage will cause air to leak into the tunnel causing the boundary layer to grow.

The tunnel has no active boundary layer control, but incorporates a smoke visualization system, which was not used in this investigation. Active boundary layer control systems would obstruct the view of the blades, inlet and outlet of the cascade. Instead, high aspect ratio blades combined with a large number of blades reduce the effects of boundary layers to an acceptable level. The test section turbulence is approximately 1.1%, as measured by Yocum[9].

4.3 AIRFOILS

The airfoils, seen in Figure 11, are constructed of polished aluminum to reduce the effects of surface roughness. The blade shape is defined by a flat pressure surface, a suction surface with a radius of 103.6 mm, and two rounded corners with a radius of 0.7 mm. This gives the blade a chord of 65.53 mm, a thickness of 6.5 mm, and a camber angle of 18 degrees.

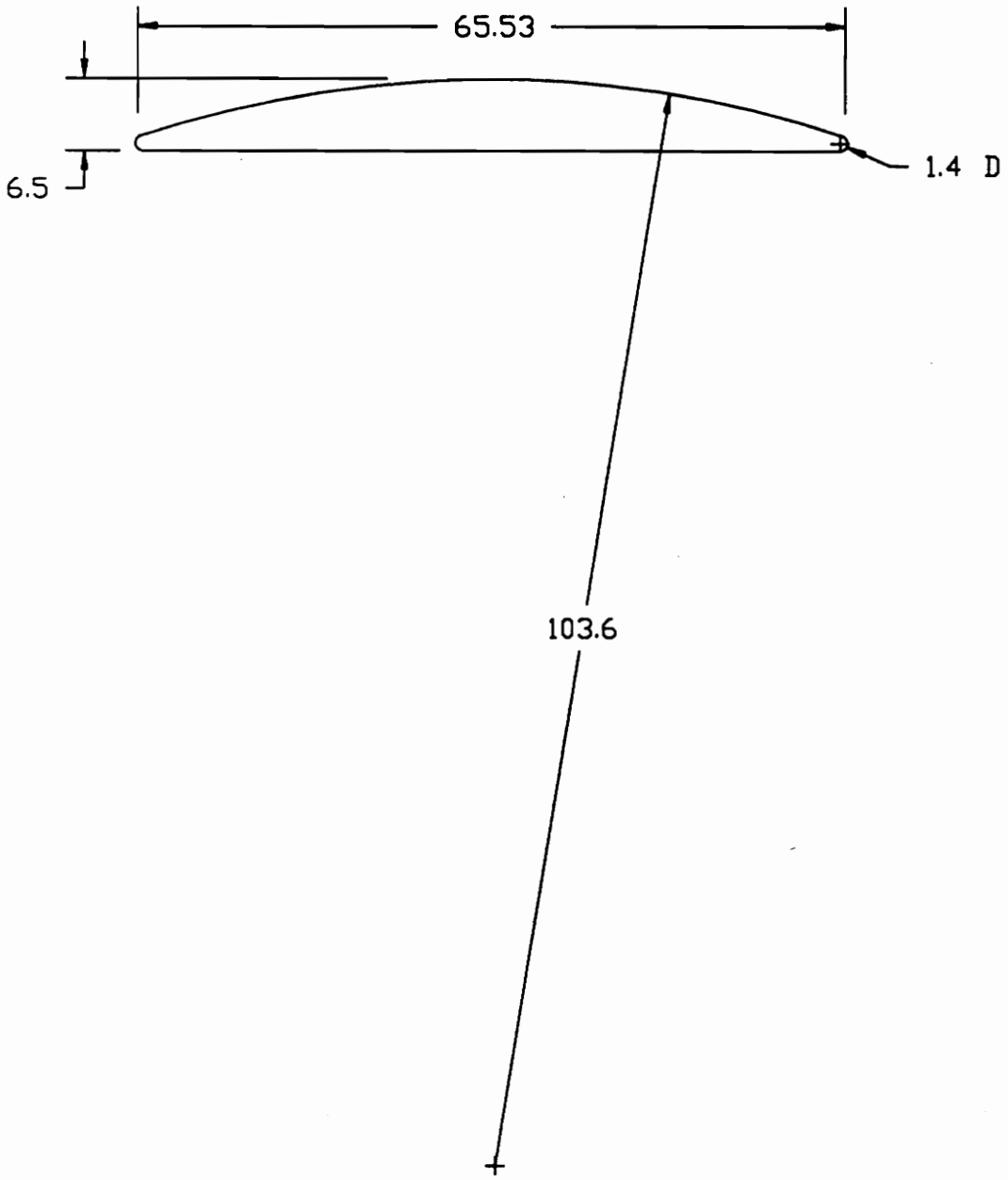

Figure 11. Airfoil Profile

The blades have no twist and a span of 304.8 mm. Since the width of the test section is 308 mm, there is a 3.2 mm gap between the blade and the plexiglass disk. This gap eases installation and removal of the blades, and must be filled with a fiberglass spacer to preserve the two dimensionality of the flow. This span, including the spacer, gave the blades an aspect ratio of 4.7.

Using a solidity of 1.5, the spacing between the blades is 43.69 mm. Putting 22 blades in a row gives a cascade length of 0.961 meters center to center.

Two adjacent blades were drilled for static pressure taps. The holes are 0.508 mm in diameter and are located at 5%, 10%, 20%, 30%, 40%, 50%, 60%, 70%, 80%, 90%, and 95% of chord, giving a total of 11 taps per blade. One blade was tapped on the suction surface, while the other was tapped on the pressure surface. These blades were installed with the tapped surfaces facing each other to form an instrumented passage.

4.4 INSTRUMENTATION

Several types of instrumentation were used to conduct this investigation. Hot film anemometry equipment was used to determine the angle of the flow, then this data was used to set the angle for the pressure measurements.

4.4.1 ANEMOMETRY EQUIPMENT

Flow angles and velocities behind the cascade were measured by a TSI split film probe model 1287 connected to a TSI intelligent flow analyzer model IFA-100. The probe has a diameter of 0.14 mm and was operated in constant temperature mode. The probe works on the principle of heat transfer from a cylinder. Since heat transfer is a

function of Reynolds number, measuring the heat transfer from the probe will give an indication of velocity. With two films split at 180 degrees, angular indications can be found knowing that the heat transfer is greater at the leading point of the probe (stagnation point) than at the trailing point of the probe. By calibrating the probe to Reynolds number and angle, the flow velocity and angle can be found.

The IFA-100 uses a 4 resistor bridge with the probe acting as one of the resistors. It also has signal processing capabilities to modify the output of the bridge to meet data acquisition demands. The signal processor was set to a gain of 1, a DC offset of 1 volt, and a low pass filter of 4 Hz. The gain and DC offset allow maximum resolution when the signal is read by a 5 volt analog to digital converter. The low pass filter rejects frequencies above 4 Hz allowing only steady state measurements to be taken. Ainslie[10] performed an error analysis of uncertainty in the anemometry system. The uncertainty in magnitude and direction was found to be ±1.2 m/s and ±1.6 degrees respectively.

4.4.2 PRESSURE MEASUREMENTS

To ascertain the aerodynamic performance of the cascade, total and static pressure measurements were performed upstream and downstream of the cascade and static pressures were measured on the blade surfaces. Upstream measurements were performed using a 3-hole cylindrical probe, model YA-120 made by United Sensor. The side holes were used to align the probe, making sure that an accurate total pressure was read by the center hole. Velocity upstream was found by measuring the total and static pressure, calculating true static pressure from a static pressure calibration curve, then calculating

velocity from Bernoulli's equation. Utilizing the same method but using the settling section pressure and a wall static tap upstream of the cascade gave results which matched the velocity from the 3-hole probe. Since the results matched, the velocity was calculated using the settling section pressure and wall static pressure taps upstream of the cascade.

Downstream measurements used a 5-hole probe, United Sensor model DC-125, that has one total pressure hole and 4 static pressure holes mounted on a goose neck. The probe was aligned using the angles from the split film tests. Velocity calculations were similar to those done for the 3-hole probe. The error associated with the pressure measurements, calculated by Ainslie[10], was ±0.28 m/s.

Instrumented blades are described in the Airfoils section.

All pressure measurements were made using one pressure transducer, a Scanivalve model SCSG/D ±5V/VG signal conditioner, and five Scanivalve model W1260/12P-12T fluidic switches. The 48 pressure tubes were connected to the 12 ports of the fluidic switches, then the output of those was connected to the fifth fluidic switch. The output of the fifth switch connects to the pressure transducer. The output of the transducer is linearized by the signal conditioner. The pressure transducer was calibrated at the beginning of each test by a 60 degree inclined manometer bank filled with red gauge oil having a specific gravity of 0.86.

4.4.3 TRAVERSING MECHANISM

The traversing mechanism, model DI-3R manufactured by L. C. Smith Company, is a closed loop device controlled by an IBM-PC. The position is determined by

potentiometers and read by the PC. The PC then sends the digital output to the positioner and the traverse is moved accordingly, until the desired potentiometer values are read by the PC. The traverse has both rotational and translational capabilities, with accuracies of ±0.8 degrees and ±0.03 mm, respectively.

4.4.4 DATA ACQUISITION SYSTEM

An IBM-PC utilizing a Data Translation DT-2811 data acquisition card acquired outputs from the IFA-100, the pressure transducer, and the traverse translational and rotational position. The card contains 8 differential analog to digital inputs and two digital outputs. The 12 bit analog to digital input has a range of 0-5 volts giving a resolution of 1.221 mv. The PC was running a data acquisition program that controlled the DT-2811, and processed and stored the data.

5.0 PROCEDURES AND METHODOLOGY

The procedures for the set-up of the wind tunnel, the preliminary data collection before the test, and the collection of the actual data are described in this section. The data reduction methodology is detailed due to an unforseen complication in matching probe position.

In general the procedure for running a test was:

1) set the test section stagger angle and angle of attack.
2) set the wind tunnel third nozzle.
3) insert either the split film probe or the 5-hole probe into the test section and configure probe support equipment.
4) acquire preliminary data.
5) run the data acquisition program and enter preliminary data.
6) turn on the wind tunnel and set Reynolds number.
7) traverse the probe in increments of 1.27 mm across the test range, reading and recording data at each position.

5.1 WIND TUNNEL AND TEST SECTION

The first step in the setup of any test was to set up the wind tunnel and test section parameters. After detaching the test section from the wind tunnel, the blades were moved, if needed, to achieve the desired stagger angle. The third nozzle was positioned, if needed, to account for the frontal area of the cascade. Reattaching the test section to the wind tunnel, the flow inlet angle (β_2) was adjusted. The plexiglass disks were then

clamped to the plywood carrier to prevent deviation from the desired flow inlet angle.

The wind tunnel itself controlled the velocity of the flow at the exit of the third nozzle. The velocity was adjusted once the wind tunnel had been turned on and the data acquisition program had been run. As described in section 4.4.2, the upstream velocity was calculated from the settling section pressure and the test section wall tap using Bernoulli's equation. Reynolds number (based on blade chord) was then calculated from the definition of Reynolds number. For the reported test data, the Reynolds numbers were set to a maximum for all flow inlet angles and stagger angles. For the study of Reynolds number effect, the Reynolds number was varied from the maximum (~200000), to a median (~130000) and to a minimum value (~60000). The maximum, median and minimum Reynolds numbers varied with the area of the third nozzle, as would be expected from the continuity equation.

5.2 PRELIMINARY DATA COLLECTION

After the tunnel was set up, the preliminary data collection was done before the data acquisition program was run. The Scanivalve was positioned to allow for the calibration of the pressure transducer. An air tube was inserted in a column of water that was at ambient room temperature to provide a steady pressure for the pressure transducer calibration. This tube was connected to the 60 degree inclined manometer bank and the pressure transducer (through the Scanivalve). After allowing time for the manometer bank to settle, readings were taken from the manometer and of the voltage produced by the pressure transducer.

Other pertinent information was collected in this period of time, including barometric pressure, relative humidity, and room temperature.

5.3 SPLIT FILM INVESTIGATION

Flow magnitude and direction were found by using the split film. Setting up the split film required attaching the probe to the IFA-100, configuring the IFA for the probe and connecting it to the computer. Configuring the IFA involved selecting the proper bridge resistance, entering the cable resistances, setting the sensor operating resistances, entering the signal conditioner parameters, and adjusting the frequency response. Once this was done, the probe was ready for taking measurements.

The split film was located mid-span in the cascade and traversed for a distance of 132.1 mm in increments of 1.27 mm, which covered 3 blade spacings. At each location, the computer sampled two channels 50 times each (one channel for each sensor in the split film probe), then recorded the average of the samples. After the test, the recorded data were processed giving velocity magnitude and direction, using the calibration curves seen in Appendix C. The velocity magnitude and direction were later used by the computer to position the 5-hole probe.

5.4 PRESSURE INVESTIGATION

Aerodynamic performance parameters were determined by measuring the upstream and downstream total and static pressures as well as the blade static pressures. Setup of the pressure probes consisted of installing them in the test section and connecting them to the scanivalve using Tygon tubing.

First, the upstream total pressure was recorded from the settling section, then the static pressure was recorded from the wall tap. Total and static pressures were also recorded from the 3-hole probe. Three measurements were taken from the 3-hole probe at 3 different locations upstream. It was noticed that the results from the settling section and wall tap pressures coincided with the 3-hole measurement results. Therefore these pressures were used for convenience instead of the 3-hole readings.

The 5-hole probe was located mid-span in the cascade and traversed for a distance of 96.52 mm in increments of 1.27 mm, which covered 2 blade spacings. At each location, the computer sampled the pressure transducer channels 50 times, then recorded the average of the samples. After the test, the recorded data were processed, giving performance parameters described in section 2.

An unforseen complication occurred in the matching of the split film and 5-hole probe positions. Specifically, the maximum flow velocities from the 5-hole and split film data were found to occur at two different locations along the traverse path. This meant that the angles used to position the 5-hole would also be incorrect. The problem was attributed to the angle of the flow with respect to the probes. Referring to Figure 12, if the probe position varies in the x direction, the variance in the y direction is much greater due to the large flow angle. This would suggest that the sensing elements of the split film and 5-hole probe were at two different locations. To correct the problem, the 5-hole data were taken at a specified average angle determined from the maximum and minimum angles seen in the reduced split film data across the entire traverse. The 5-hole data then

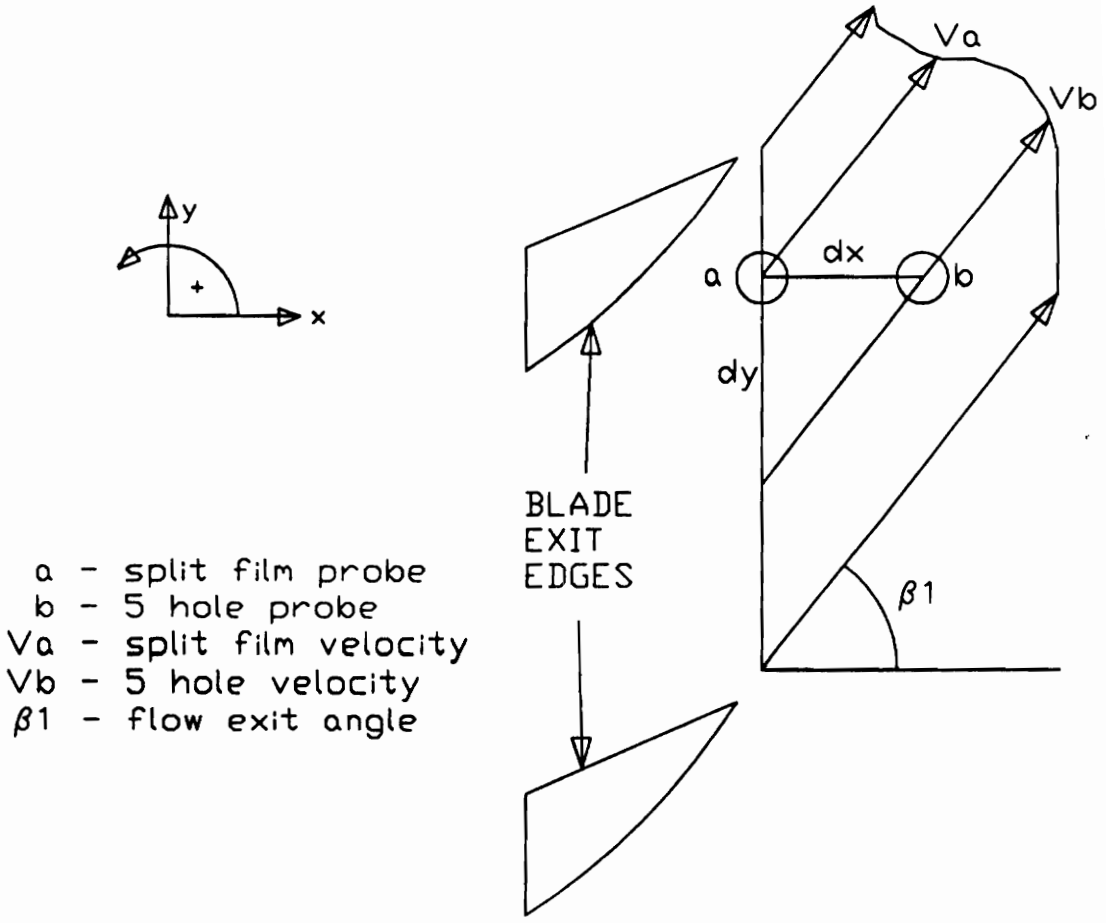

Figure 12. Probe Position Variance

had to be processed to account for a variance between the angle at which the data were taken and the angle described by the split film. The 5-hole calibration curves are presented in Appendix C.

After the 5-hole traverse was performed, the blade static pressures were sampled 50 times, averaged, and stored. The blade static pressure readings were obtained at the same flow conditions as the 5-hole traverse.

5.5 DATA REDUCTION

Several types of data reduction were performed to complete this investigation. Split film data were reduced from two voltages to velocity magnitude and direction. This was done using calibration data for the split film and an interpolation routine (Appendix C). The calibration data were organized to give Reynolds number (based on probe diameter) and angle as a function of added and subtracted channel voltages from the split film, E1+E2 and E1-E2, respectively. The program calculated these voltages, then interpolated to find the results using a spline fit routine.

Pressure data reduction was more involved. The program read in the 5-hole calibration curves as well as the split film reduced data. The calibration curve for the 5-hole probe gave total and static correction factors as a function of variance in angle. The angular variance was the tested angle minus the split film angle. The program then read in the raw data from the 5-hole traverse.

First the program calculated the velocity using an angular variance of zero, since the traverse position of the maximum velocity from the 5-hole measurements was

unknown. The maximum velocity from the 5-hole data was then matched with the maximum velocity from the split film data, thereby giving the split film angle. The program used the angular variance and the calibration curve to correct the total and static pressures, then calculated velocity from the corrected pressures. This process was iterated until there was no change in the position or magnitude of the maximum velocity.

Once the total and static pressures were corrected, the cascade performance parameters described in section 2.3 were calculated from the data.

6.0 RESULTS

Results obtained from this investigation are summarized in Table I. Individual test results are presented in this Chapter, followed by calculated results in Chapter 7.

6.1 ORGANIZATION OF RESULTS PRESENTED

As previously explained, reversed flow in a compressor stage involves very large positive angle of attack with respect to the trailing edge of a rotor blade, and very large negative angle of attack with respect to the trailing edge of an inlet guide vane. Also, for reversed flow, the rotor blades present a negative stagger angle to the relative flow, while the stationary inlet guide vane appears to have the usual stagger angle, defined as positive with respect to the flow.

Thus, the flow data obtained were organized into two groups:

Group I) data for negative stagger angle and positive angle of attack.

Group II) data for positive stagger angle and negative angle of attack.

Three absolute values of stagger angle, 25, 36.5, and 45 degrees, were tested in each group. A wide range of angle of attack was tested, from 70 to 130 degrees, and from -70 to -130 degrees.

Measured results are presented in Figures 13 through 30, which are placed at the end of the chapter. The upper left graph exhibits non-dimensional blade static pressure tap results. The abscissa, fraction of chord, is denoted 0 at the (normally) trailing edge of the blade, where the reversed flow would enter the blade passage. A fraction of chord

Table I. Summary of Experiments and Results

Experiments Performed	
Stagger Angle	**Angle of Attack**
-25	70 to 110
-36.5	81.5 to 121.5
-45	90 to 130
25	-70 to -110
36.5	-81.5 to -121.5
45	-90 to -130

Individual Test Results
Blade Tap C_{Pt} and C_{Ps}
Blade Velocity Vectors
5 Hole Probe C_{Pt} and C_{Ps}
Blade Exit Angle

Reduced Results
Station 2 Mass Averaged Total Pressure Loss
Station 3 Mass Averaged Total Pressure Loss
Station 2 Mass Averaged Turning Angle
Station 3 Mass Averaged Turning Angle
Blade Tap Normal Force Coefficient
Momentum Equation Normal Force Coefficient
Axial Velocity Ratio

equal to 1 denotes the (normally) leading edge of the blade, where the reversed flow exits the blade passage.

The 5-hole probe non-dimensional, total and static pressure results are included in the lower left graph. The abscissa, y/s, is defined as the traverse location divided by the blade chord. Velocity vectors in the upper right graph pictorially show the actual flow that is entering and exiting the blade passage. The velocity vectors are obtained from the combination of split film data and 5-hole probe data, and are scaled 1 cm to approximately 29 m/s. Finally, blade exit angle from the split film tests is shown in the lower right graph. All 5-hole probe data, velocity vectors, and exit angles are for station 2, 0.543 chords downstream of the stagger line.

The data represented by the blade pressure profile, total, static pressure and turning angle curves of Figures 13 through 30 are the measurements used to develop the computed cascade performance parameters. These parameters are presented in Chapter 7. Discussion and interpretation of these results and trends follows in Chapter 8.

A short discussion of the behavior of the measured velocity vector patterns follows.

6.2 NEGATIVE STAGGER ANGLE - GROUP I

Figures 13-20 show a sample of individual test results obtained from the negative stagger angle testing.

As seen in the velocity vector diagram, the 25 degree negative stagger angle results exhibit backflow at the blade passage exit at an angle of attack of 80 degrees

(Figure 13). The exit flow for an angle of attack of 90 degrees (Figure 14) contains less backflow and a less parallel velocity profile than the flow for an angle of attack of 80 degrees. At 110 degrees angle of attack (Figure 15), the backflow disappears, which can be seen by the exit angle variations.

For the 36.5 degree negative stagger angle, the wake region of the exit flow grows with increasing positive angle of attack (the wake is defined as the general region of retarded exit flow). Finally, the exit flow pattern dissolves into chaotic flow at very high angles of attack. At an angle of attack of 81.5 degrees (Figure 16), the exit flow is straight, and nearly parallel with a small wake. At an angle of attack of 91.5 degrees (Figure 17), the wake starts to spread and widen. After the angle of attack of 91.5 degrees, the wake widens further and continues to spread. Finally at angles of attack near 120 degrees, the exit flow pattern becomes chaotic and non-parallel, as shown for an angle of attack of 121.5 degrees (Figure 18).

The exit flow for the 45 degree negative stagger angle tests exhibits the same type of behavior as for the 36.5 degree negative stagger angle. Below an angle of attack of 115 degrees, the exit flow is straight, and nearly parallel with a small wake. At an angle of attack of 115 degrees (Figure 19), the exit flow becomes disorganized, then, unexpectedly, appears to reorganize at an angle of attack of 125 degrees (Figure 20). The 125 degree angle of attack exit flow appears to be quite uniform.

6.3 POSITIVE STAGGER ANGLE - GROUP II

Figures 21-30 show a sample of individual test results obtained from the positive

stagger angle testing.

For all negative angles of attack tested, the exit flow from the 25 degree positive stagger angle cascade exhibits backflow in the velocity vector diagram. Increasing the angle of attack beyond -100 degrees, the exit flow pattern becomes non-parallel with increased backflow. The results for an angle of attack of -70 degrees (Figure 21) and -105 degrees (Figure 22) illustrate these points.

The exit flow for the 36.5 degree positive stagger angle tests presents small wakes at the angle of attack of -81.5 degrees (Figure 23). The wakes in the exit flow profile enlarge and the exit velocity profile shows sharp areas of maximum velocity at -96.5 degrees angle of attack (Figure 24). As angle of attack decreases to -106.5 degrees (Figure 25), the exit flow pattern becomes non-parallel with backflow. At the final angle of attack of -121.5 degrees (Figure 26), the exit flow pattern is non-parallel without backflow.

A uniform and parallel exit velocity profile is seen in the 45 degree positive stagger angle results at an angle of attack of -95 degrees (Figure 27). Non-parallel exit flow develops at an angle of attack of -110 degrees (Figure 28), continuing to very non-parallel exit flow at an angle of attack of -120 degrees (Figure 29). Finally the exit flow profile, becomes parallel and uniform at -130 degrees angle of attack (Figure 30).

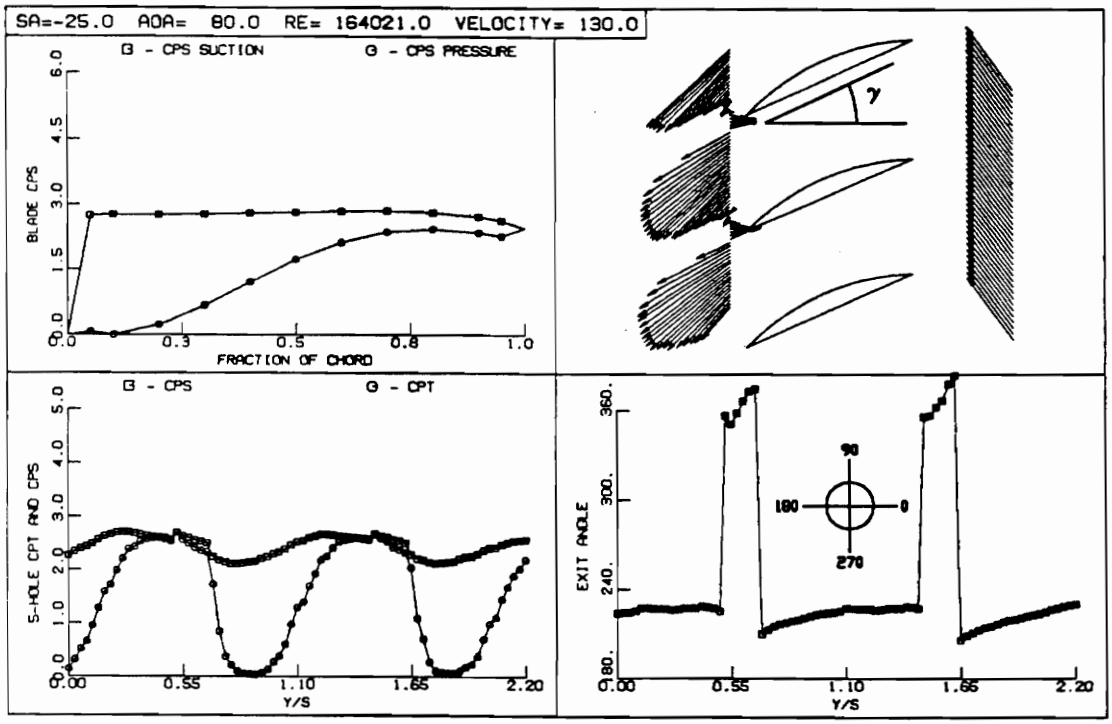

Figure 13. Individual Test Result, SA=-25, AOA=80

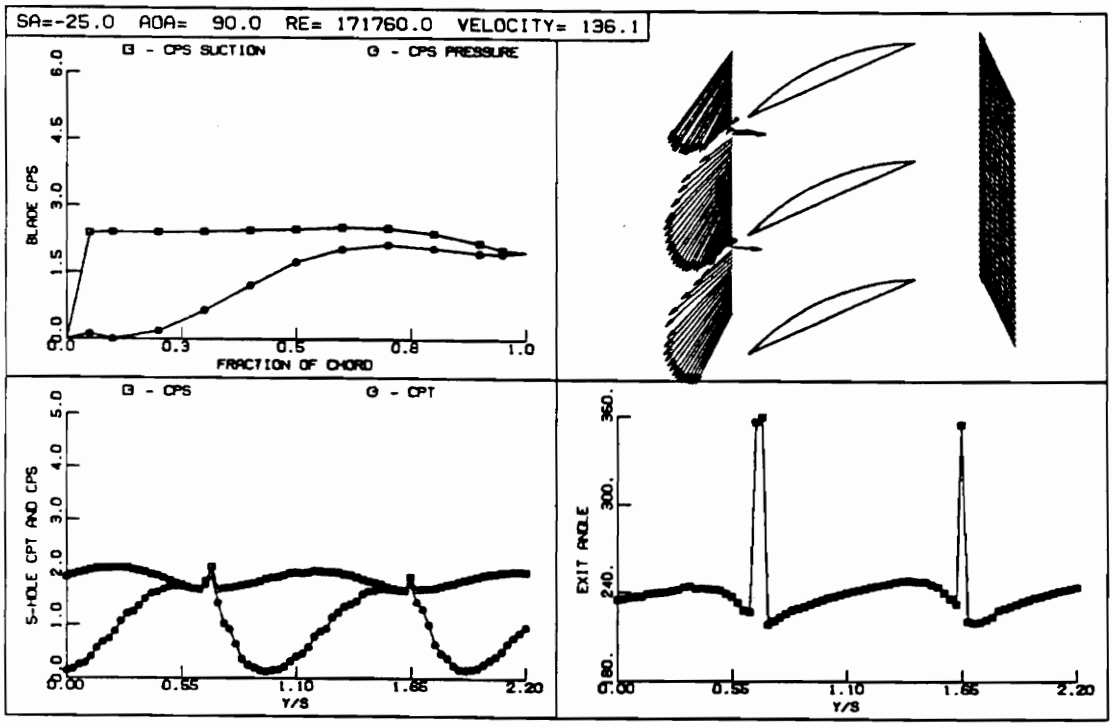

Figure 14. Individual Test Result, SA=-25, AOA=90

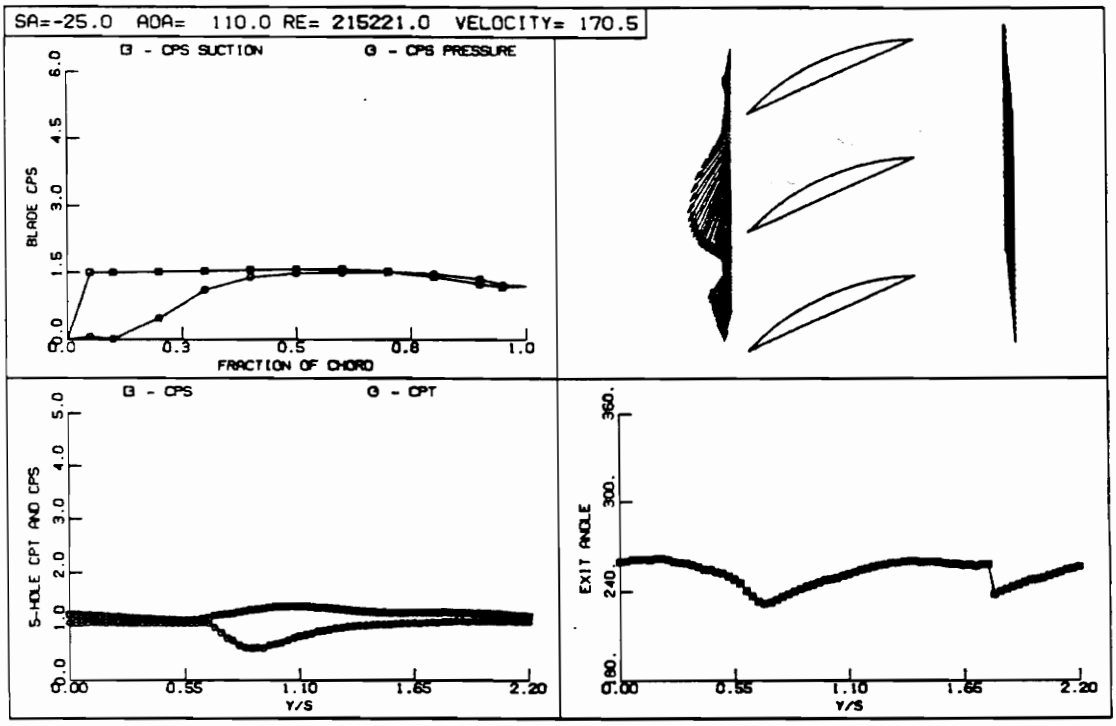

Figure 15. Individual Test Result, SA=-25, AOA=110

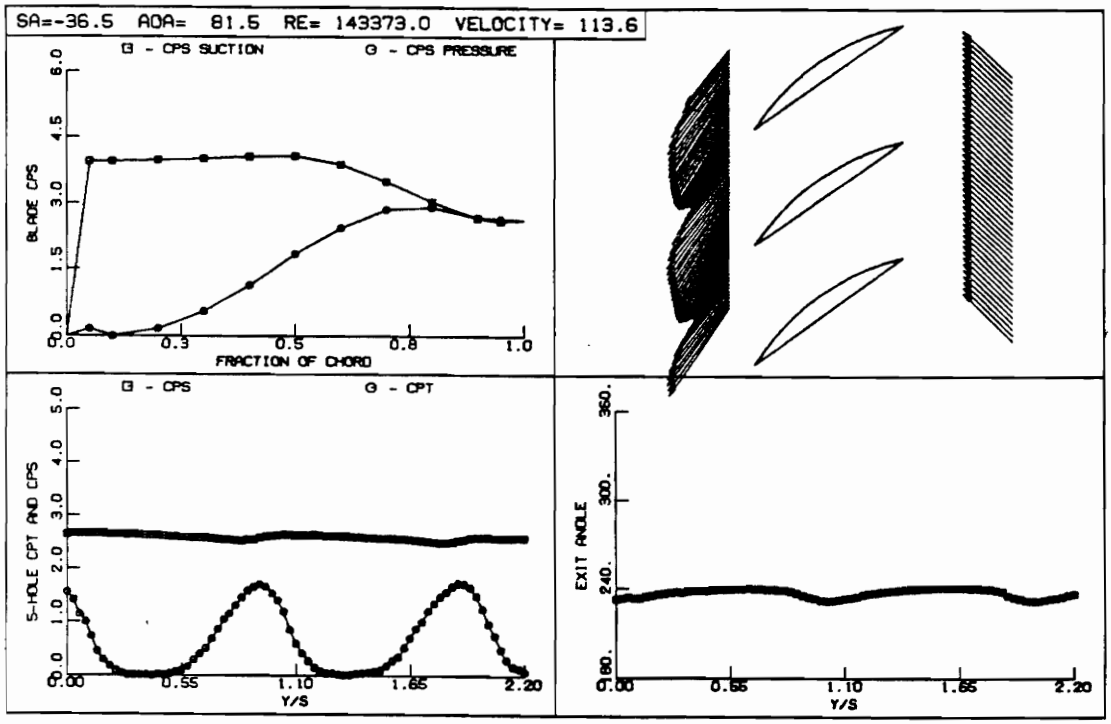

Figure 16. Individual Test Result, SA=-36.5, AOA=81.5

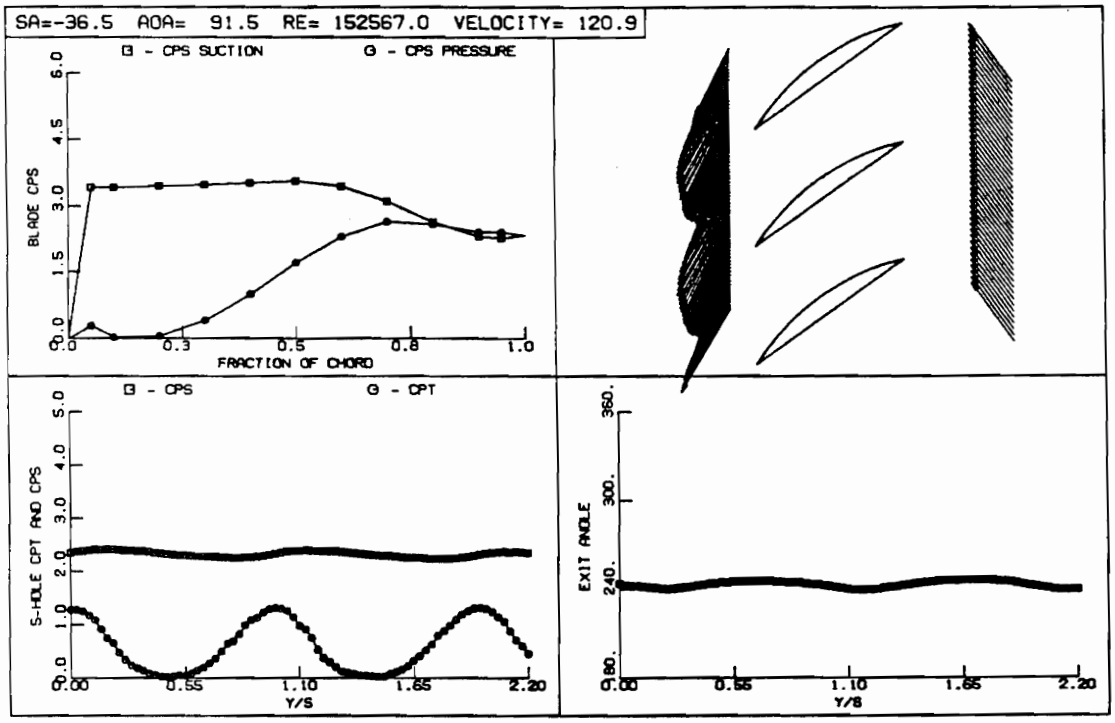

Figure 17. Individual Test Result, SA=-36.5, AOA=91.5

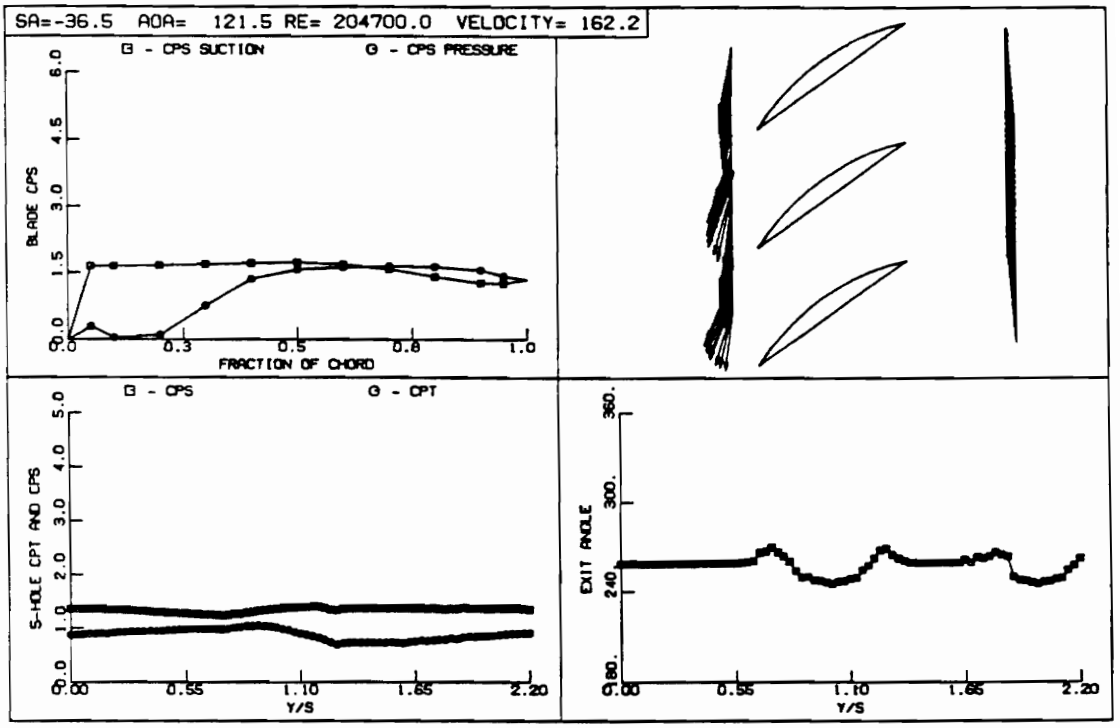

Figure 18. Individual Test Result, SA=-36.5, AOA=121.5

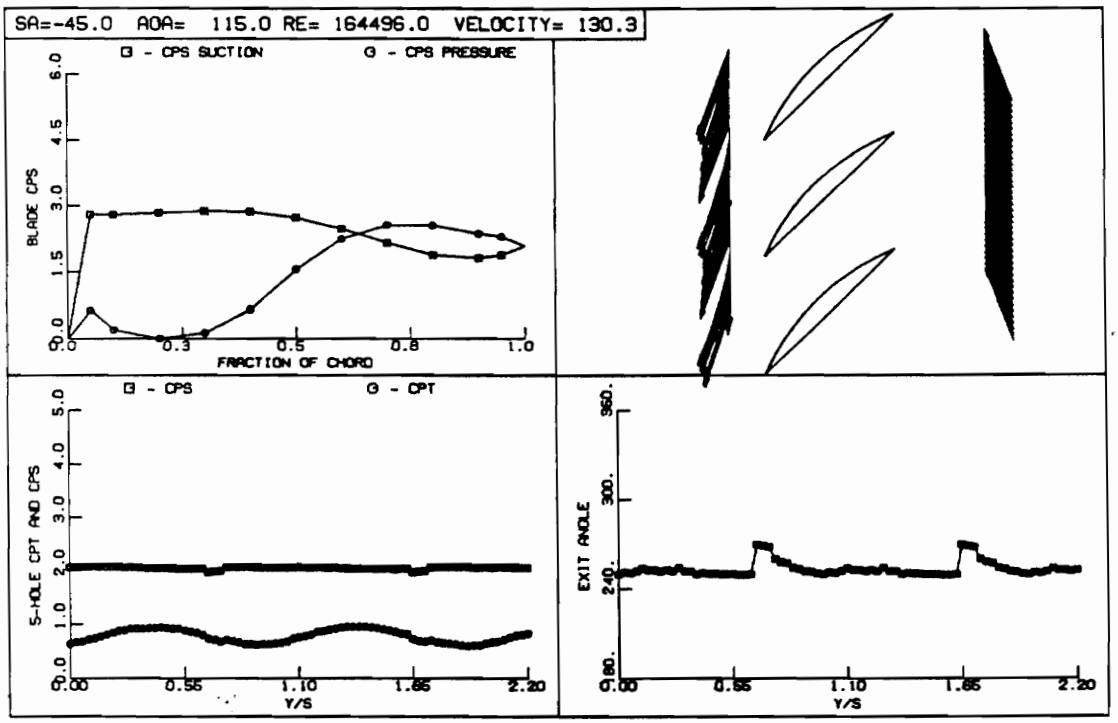

Figure 19. Individual Test Result, SA=-45, AOA=115

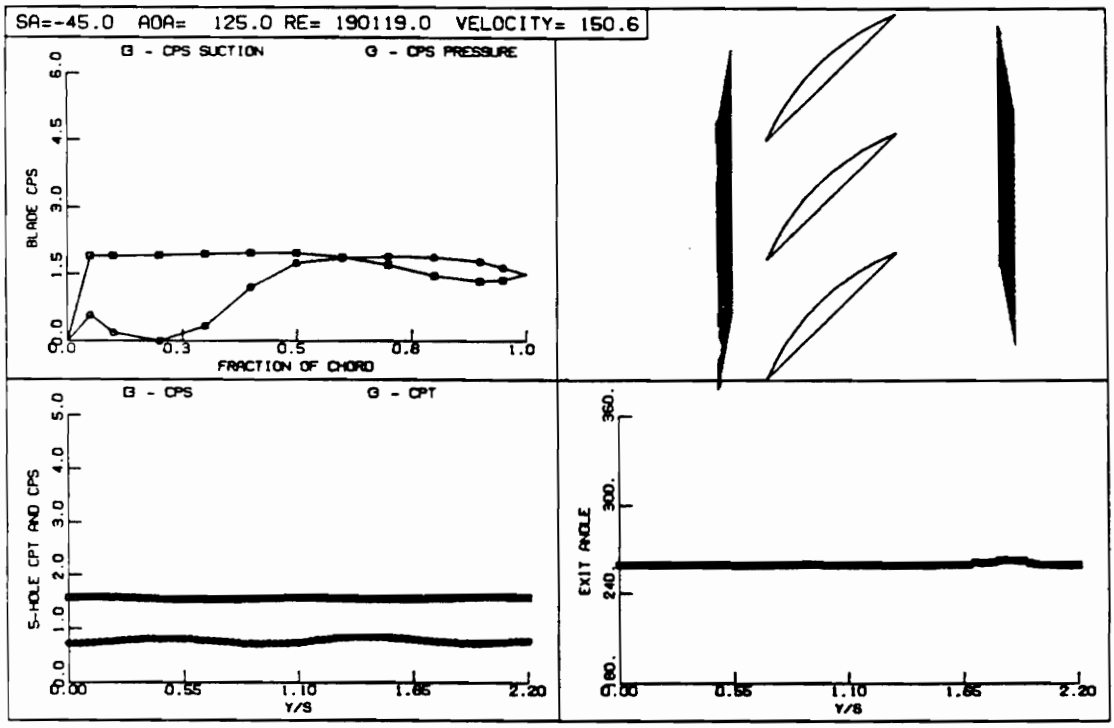

Figure 20. Individual Test Result, SA=-45, AOA=125

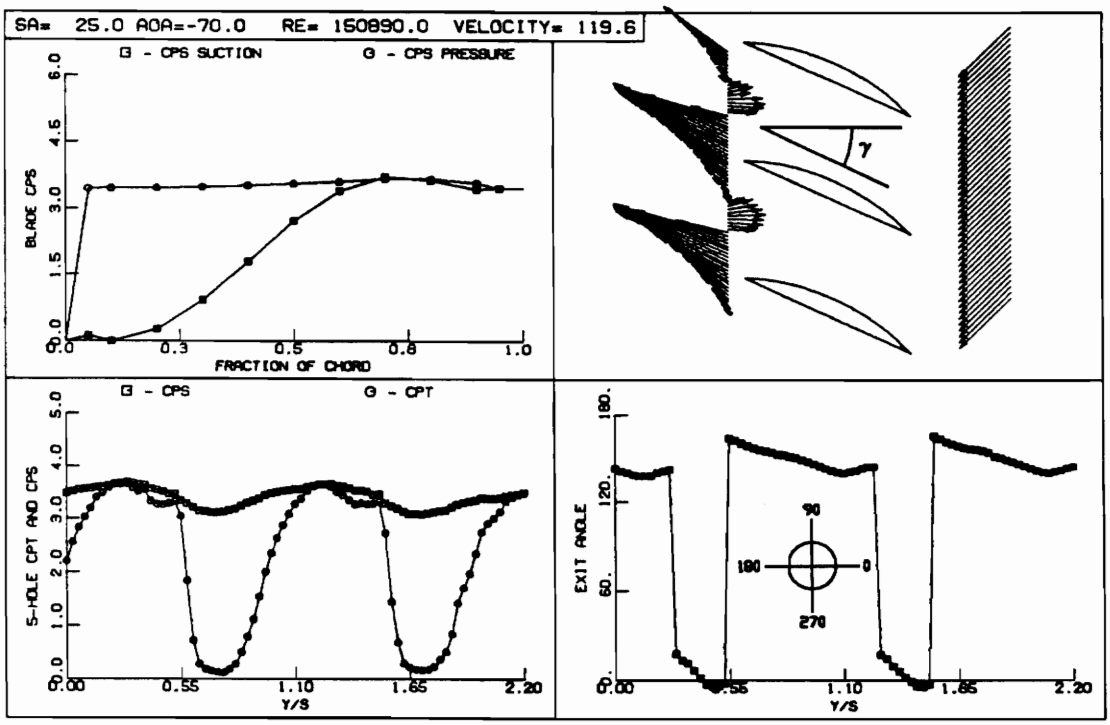

Figure 21. Individual Test Result, SA=25, AOA=-70

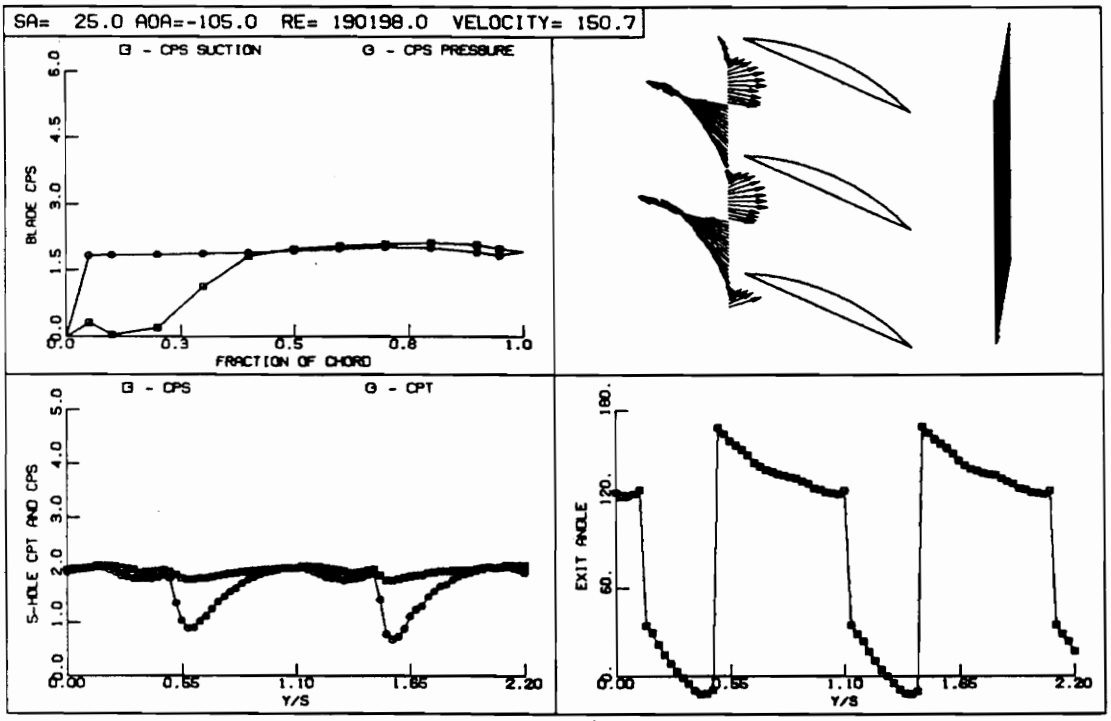

Figure 22. Individual Test Result, SA=25, AOA=-105

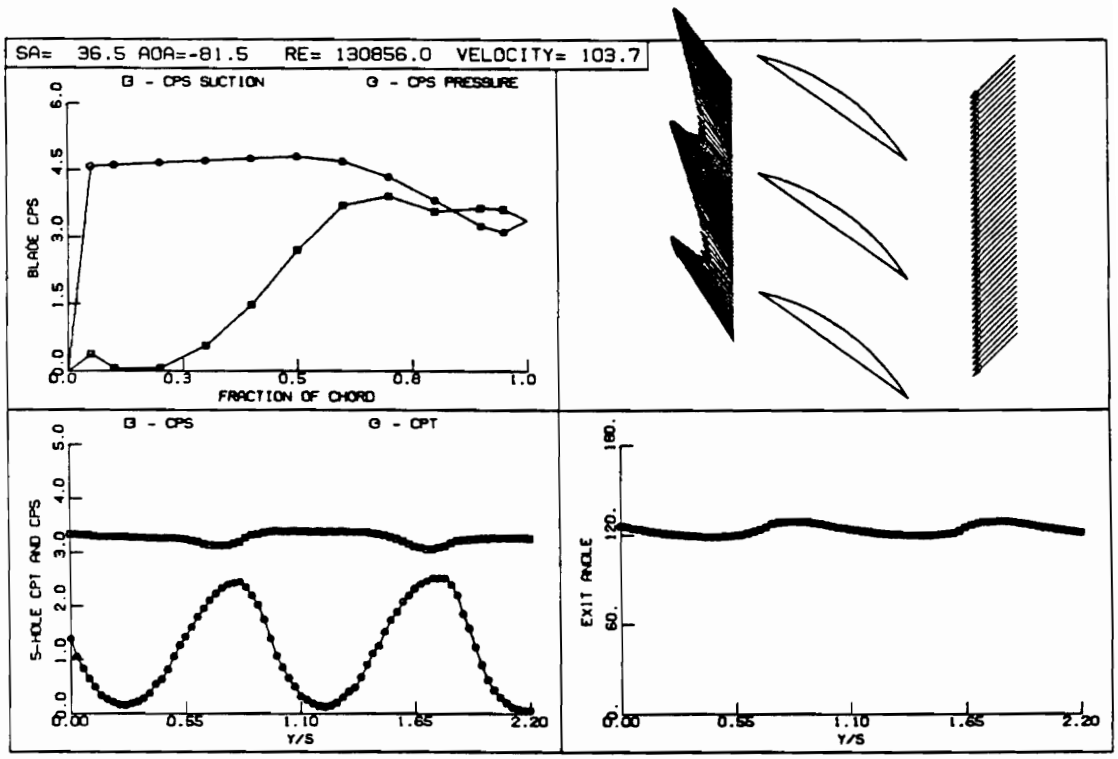

Figure 23. Individual Test Result, SA=36.5, AOA=-81.5

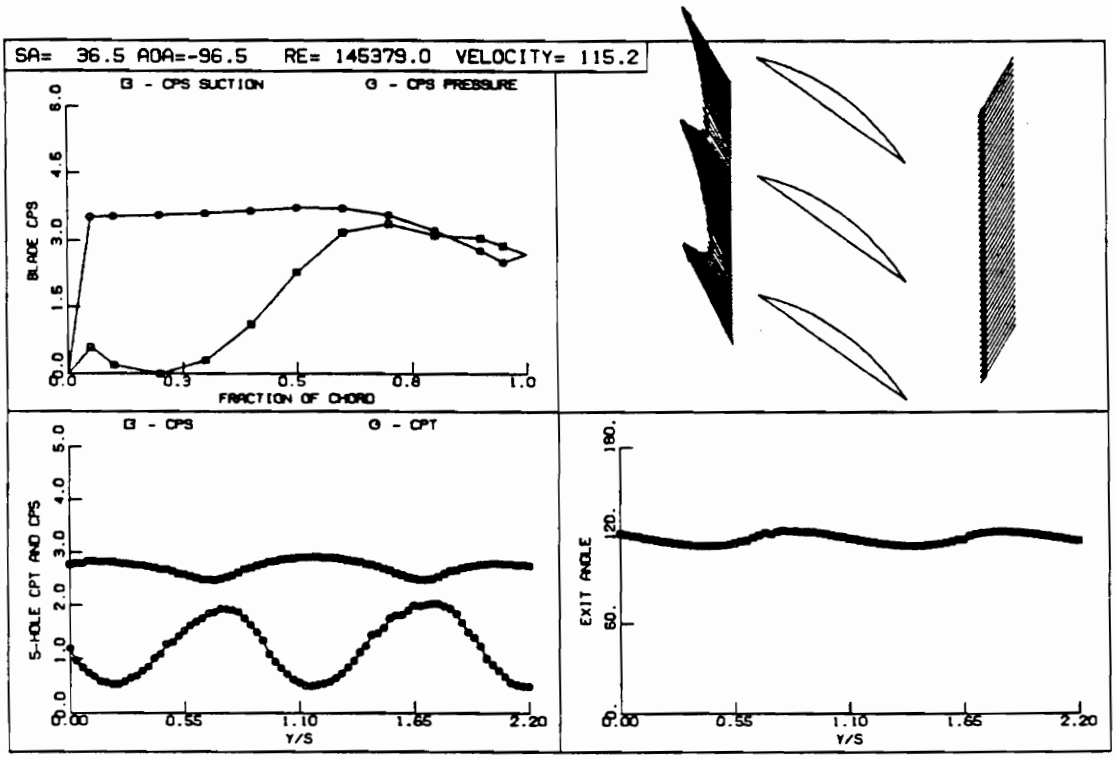

Figure 24. Individual Test Result, SA=36.5, AOA=-96.5

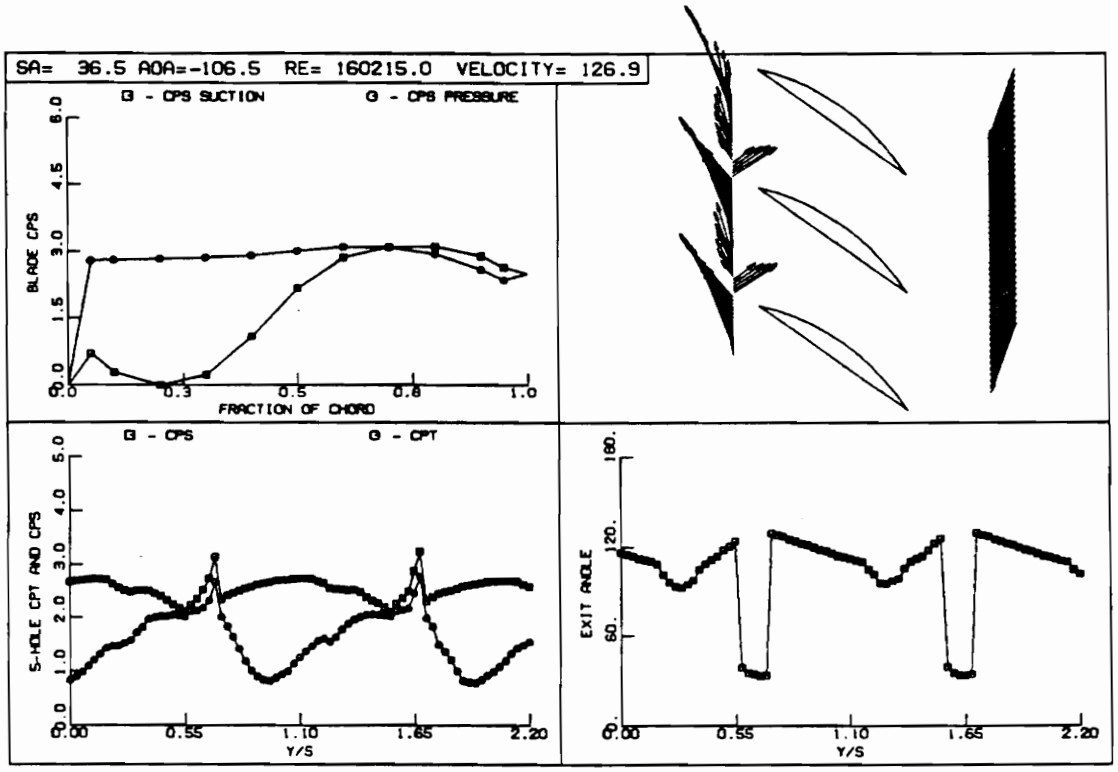

Figure 25. Individual Test Result, SA=36.5, AOA=-106.5

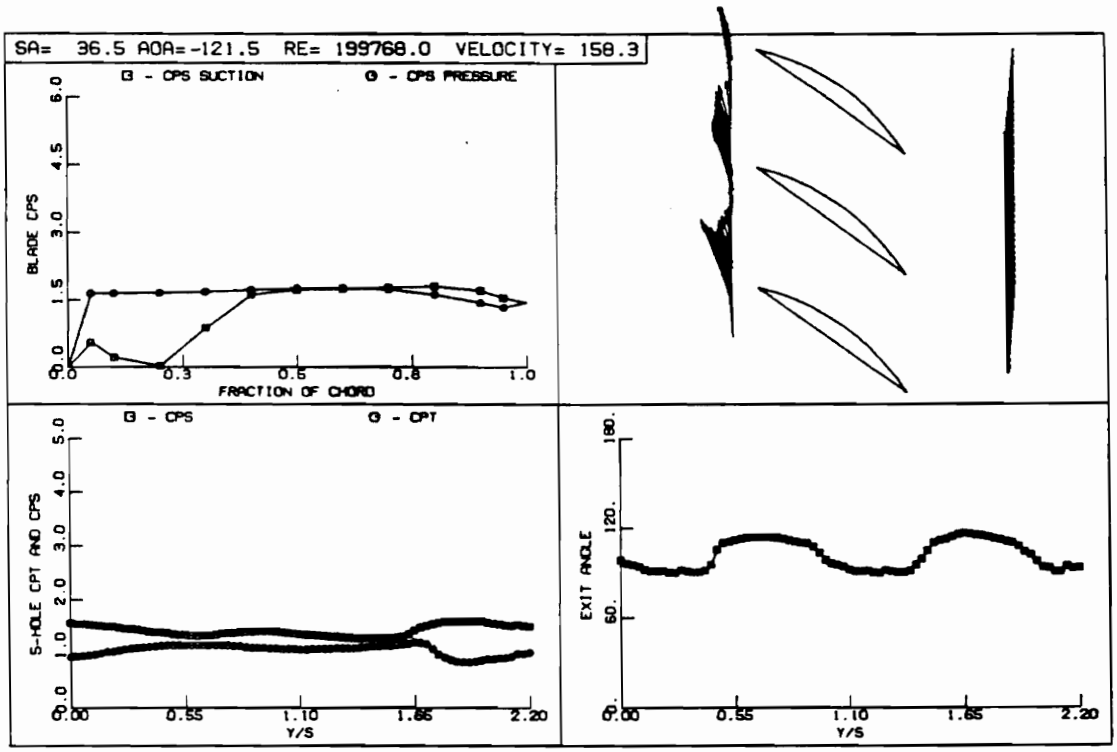

Figure 26. Individual Test Result, SA=36.5, AOA=-121.5

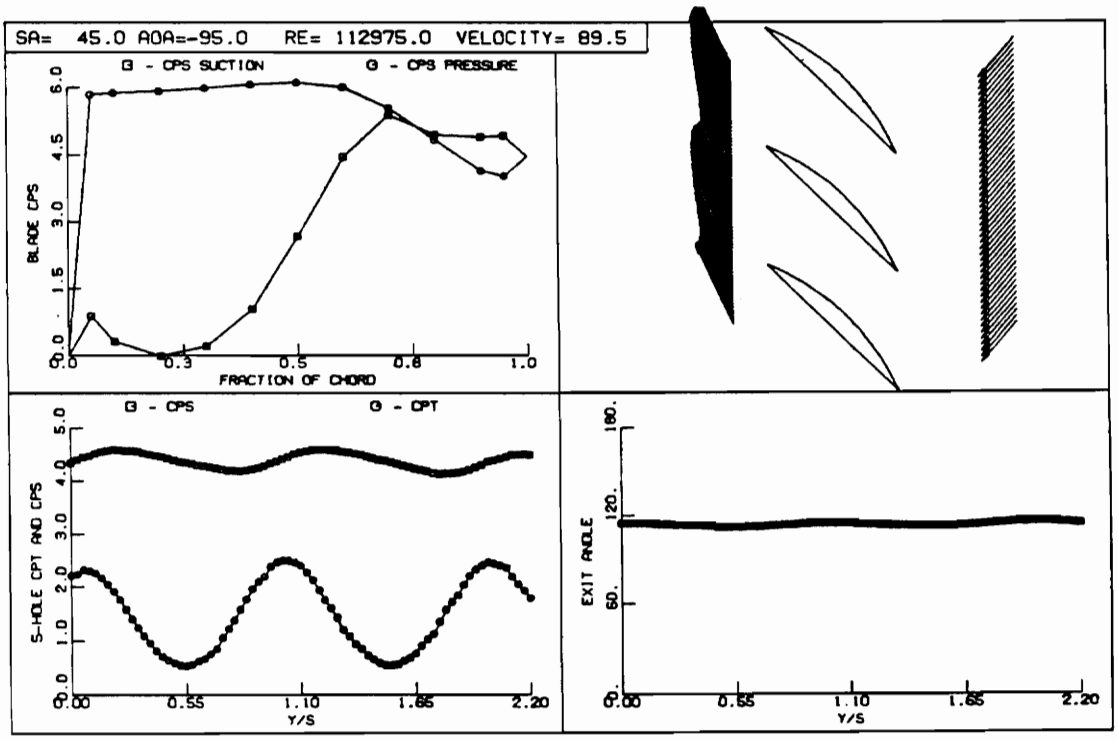

Figure 27. Individual Test Result, SA=45, AOA=-95

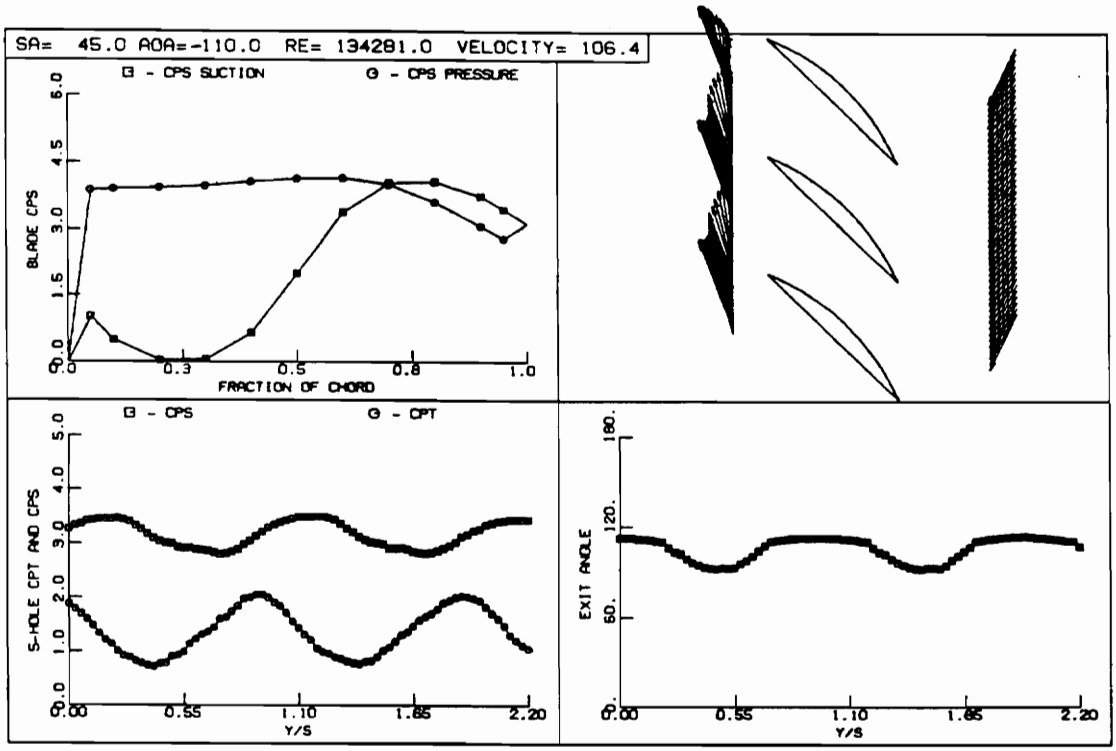

Figure 28. Individual Test Result, SA=45, AOA=-110

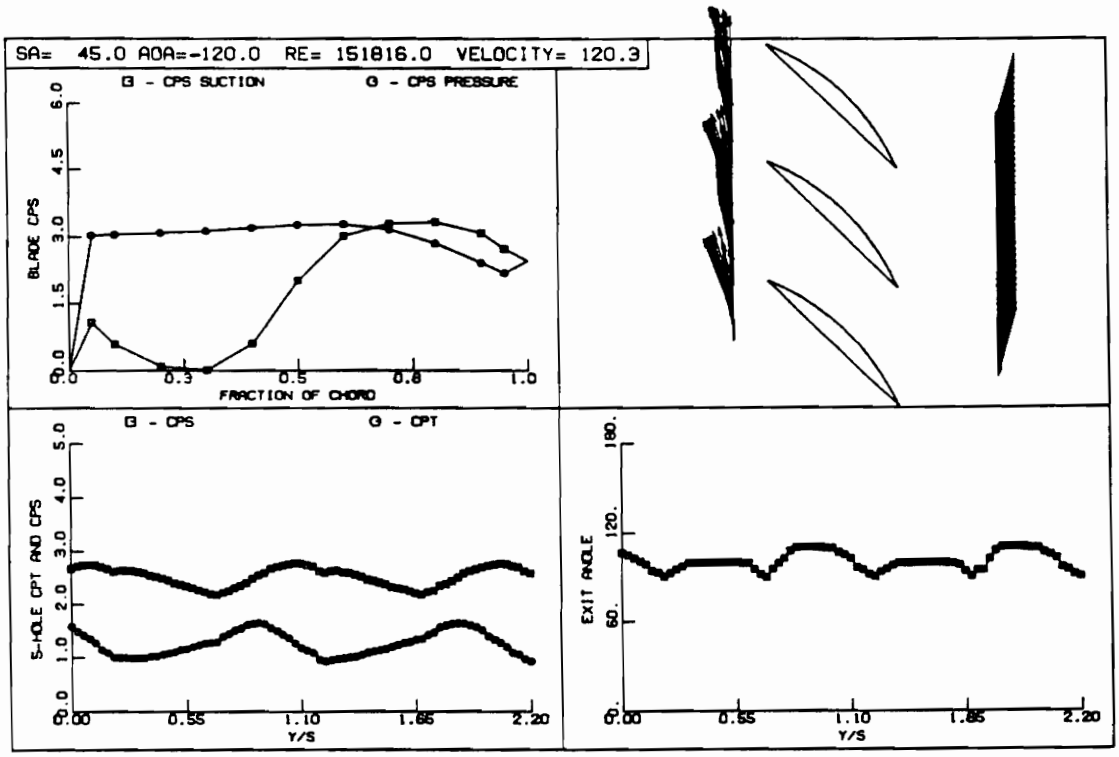

Figure 29. Individual Test Result, SA=45, AOA=-120

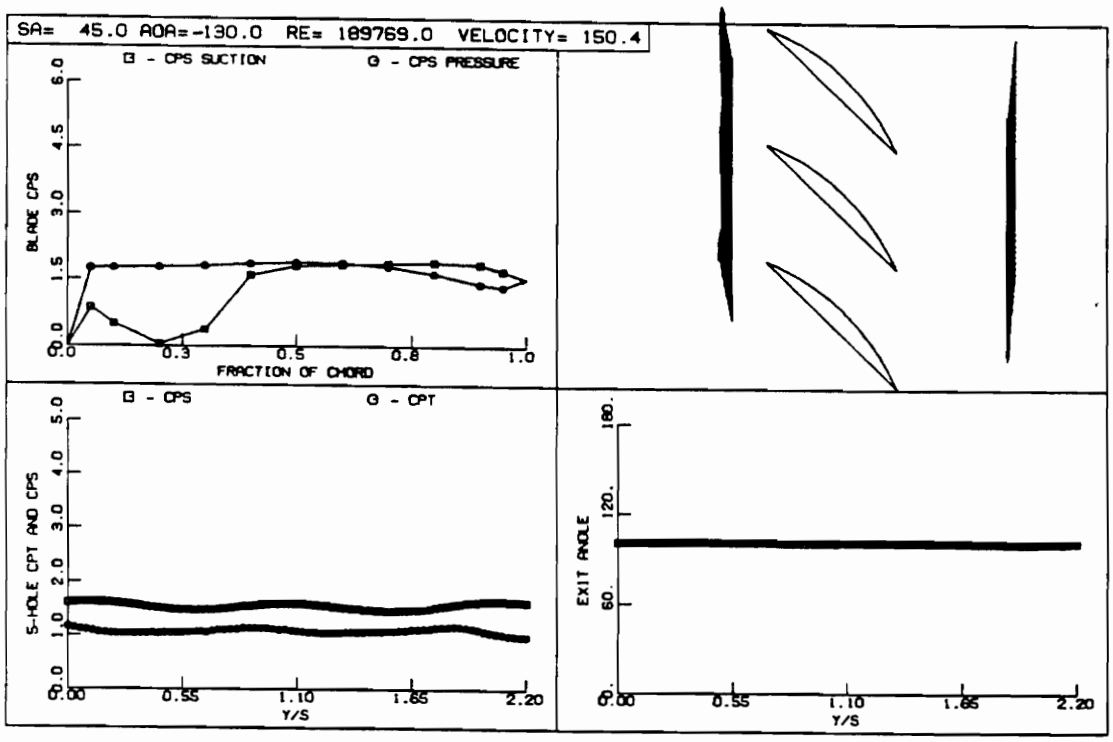

Figure 30. Individual Test Result, SA=45, AOA=-130

7.0 CALCULATED RESULTS FOR CASCADE PERFORMANCE

Following the arrangement used in Chapter 6, the calculated flow results were organized into two groups:

Group I) data for negative stagger angle and positive angle of attack.

Group II) data for positive stagger angle and negative angle of attack.

Each group includes calculated results presented as seven aerodynamic performance parameters that were defined in Section 3.4 versus angle of attack. Each point on the aerodynamic performance parameter graphs is the result of computations using reduced data from the previously presented individual test results.

A summary of observed trends in the calculated results is presented in Table II.

The aerodynamic performance parameter graphs for Group I are seen in Figures 31 through 37. Group II aerodynamic performance parameter graphs are shown in Figures 38 through 44.

Rotor station 2 mass averaged total pressure loss is plotted versus Reynolds number in Figure 45. Calculations for three different stagger angles and three angles of attack per stagger angle are plotted. The effect of Reynolds number upon the calculated losses is negligible for this range of Reynolds number. This result is typical for all other performance parameters discussed, and therefore it was decided not to include other graphs.

In 31 through 44, NSA in figure titles means negative stagger angle. PSA in

figure titles means positive stagger angle. MATPL in the title of Figure 45 means mass averaged total pressure loss.

Discussion of the results follows in Chapter 8.

Table II. Summary of Calculated Results

TEST GROUP I **Summary of Negative Stagger Angle Calculated Results**	
Parameter	**Effect**
increasing negative stagger angle	decreasing ω_2
	increasing ω_3
	decreasing ε_2, ε_3
	increasing C_{Fn}
increasing angle of attack	increasing ω_2
	decreasing ω_3
	increasing ε_2, ε_3
	decreasing C_{Fn}

TEST GROUP II **Summary of Positive Stagger Angle Calculated Results**	
Parameter	**Effect**
increasing positive stagger angle	increasing ω_2, ω_3
	decreasing ε_2, ε_3
	increasing C_{Fn}
increasing negative angle of attack	no discernable trend for ω_2
	decreasing ω_3
	increasing ε_2, ε_3
	decreasing C_{Fn}

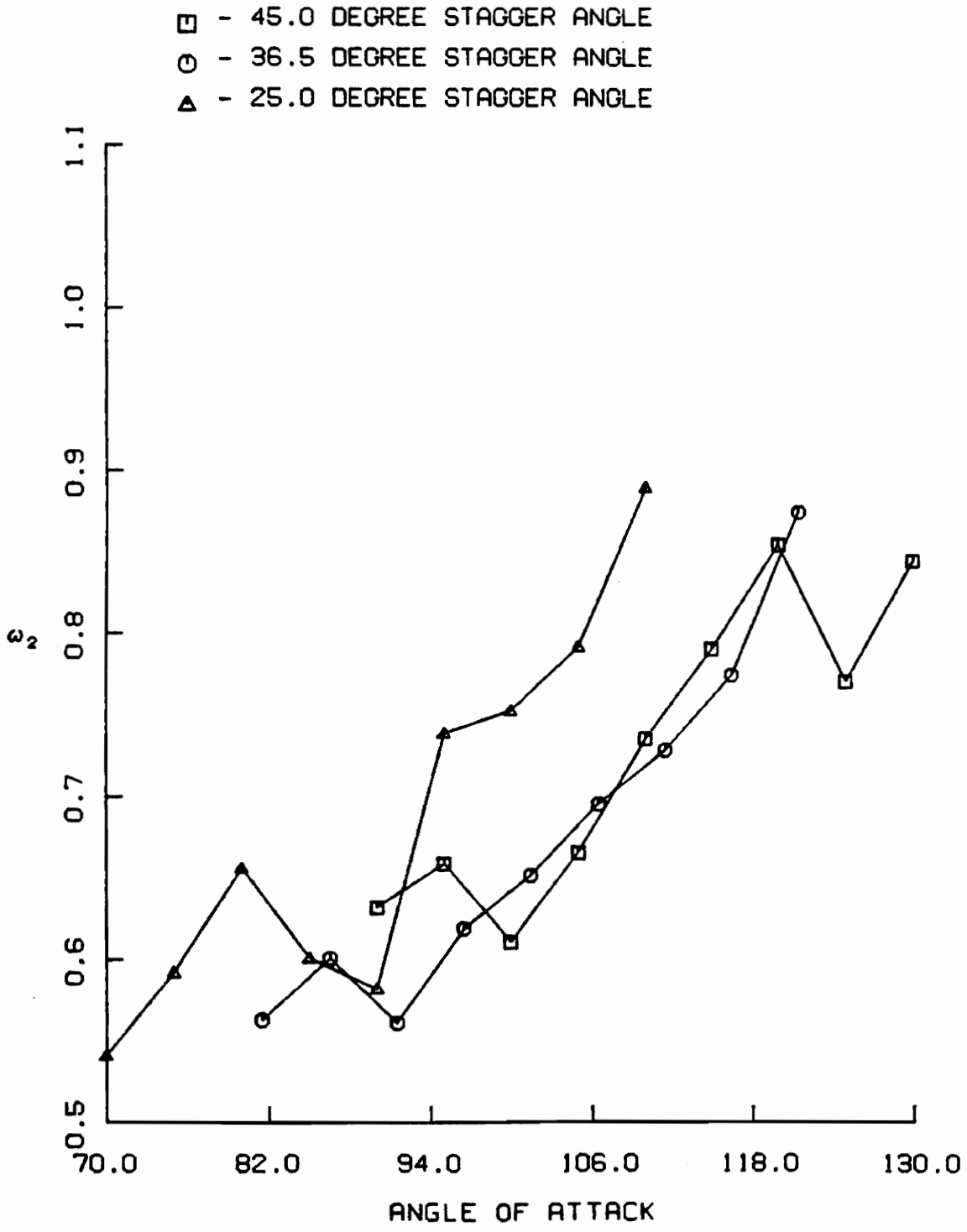

Figure 31. NSA Station 2 Mass Averaged Total Pressure Loss

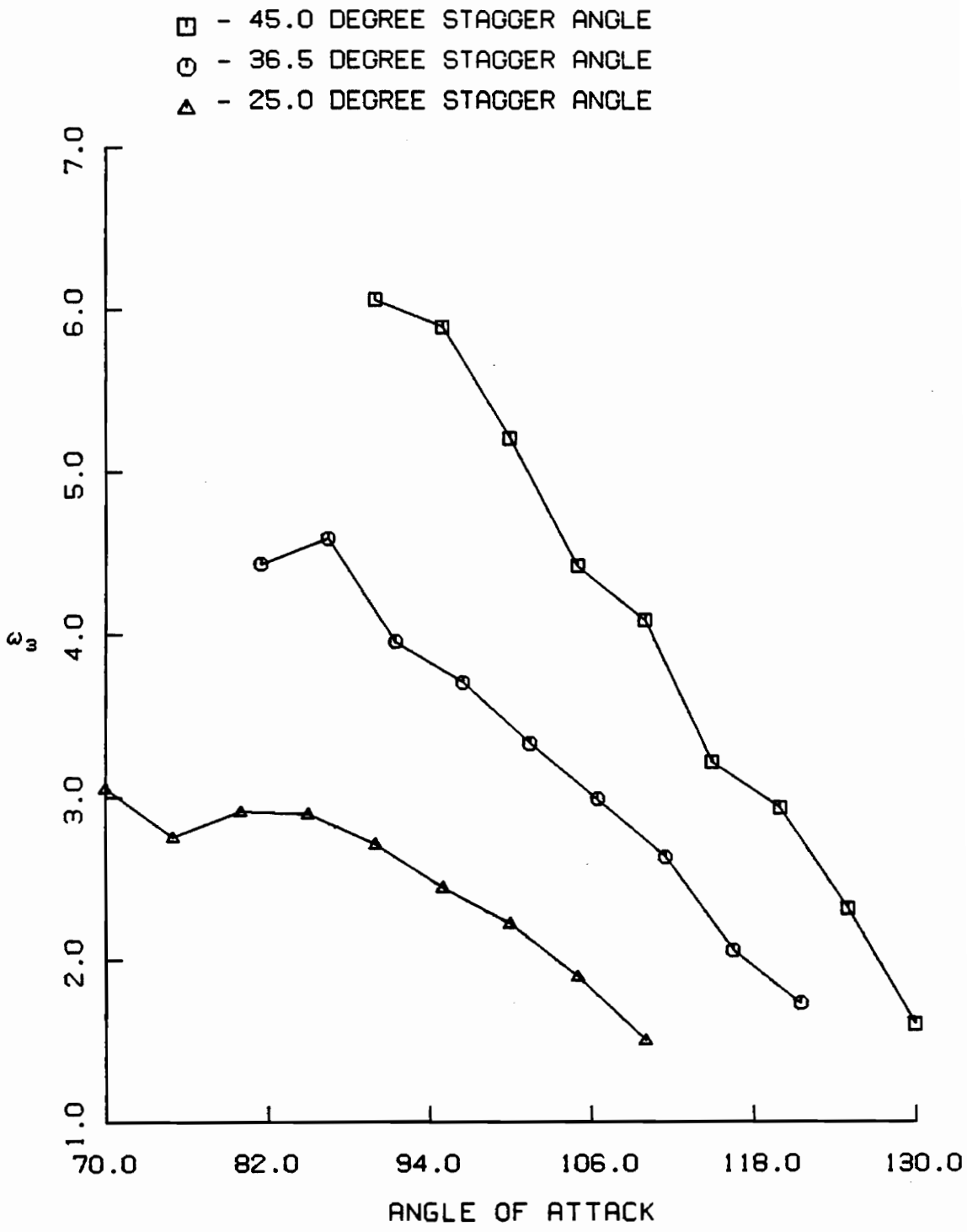

Figure 32. NSA Station 3 Mass Averaged Total Pressure Loss

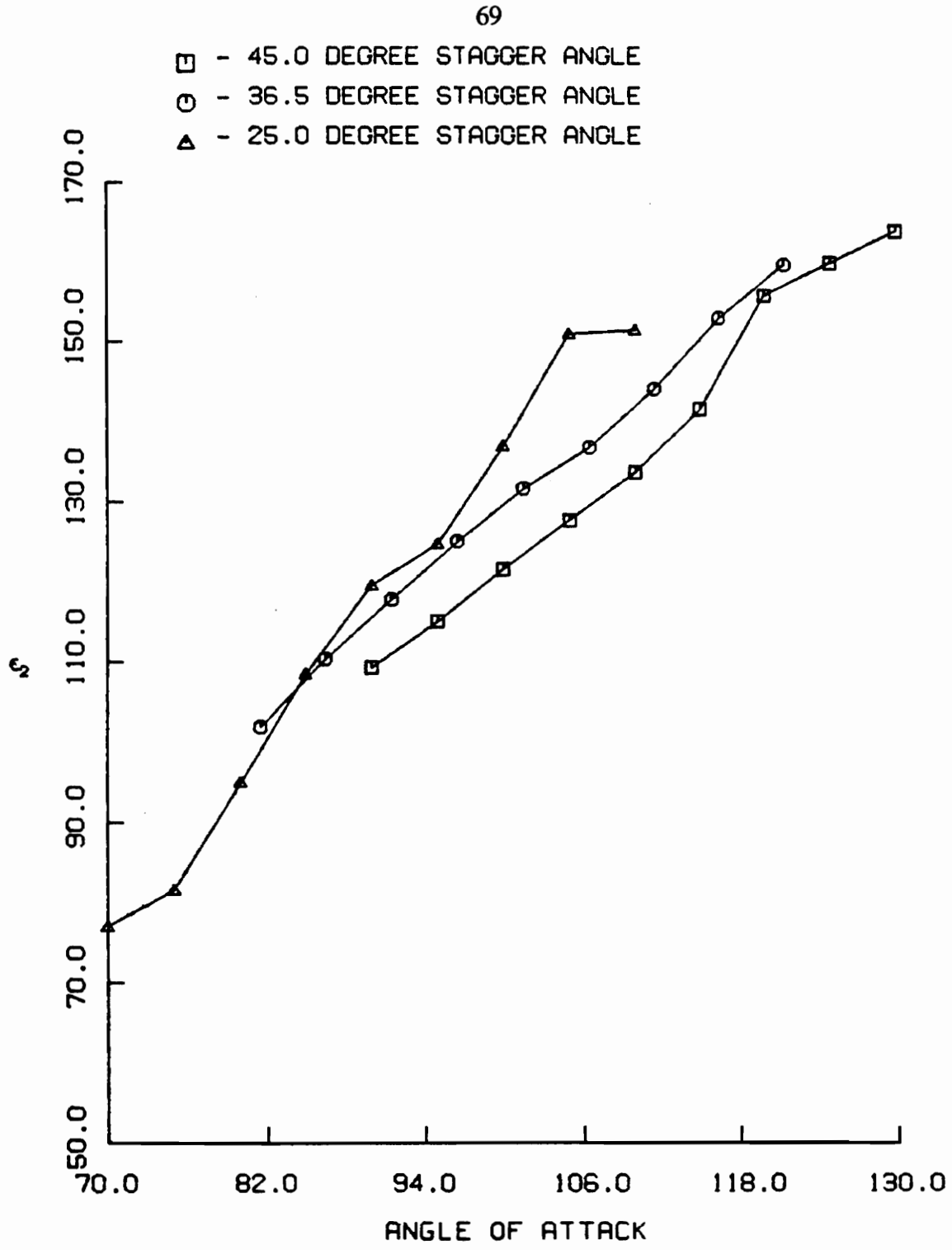

Figure 33. NSA Station 2 Mass Averaged Turning Angle

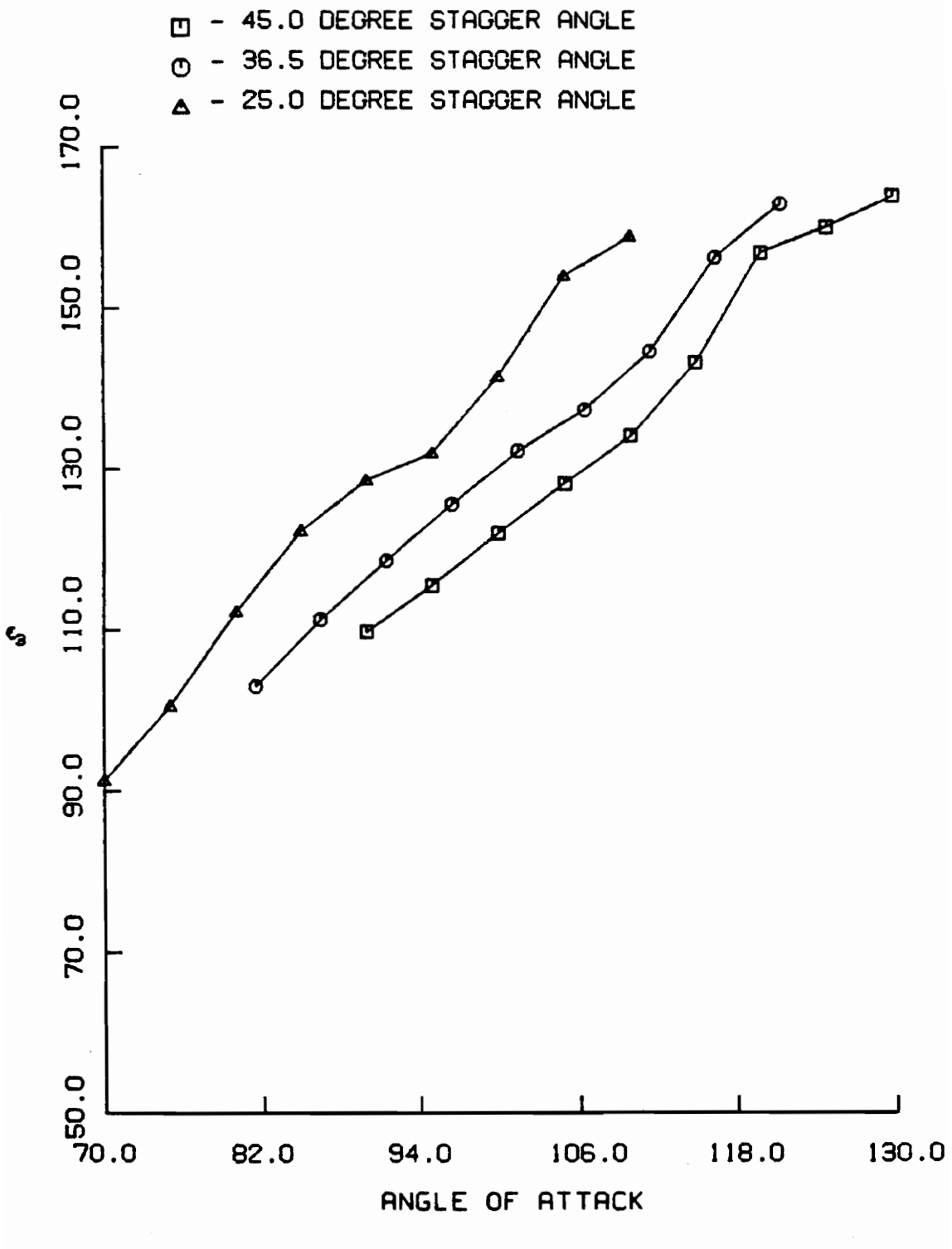

Figure 34. NSA Station 3 Mass Averaged Turning Angle

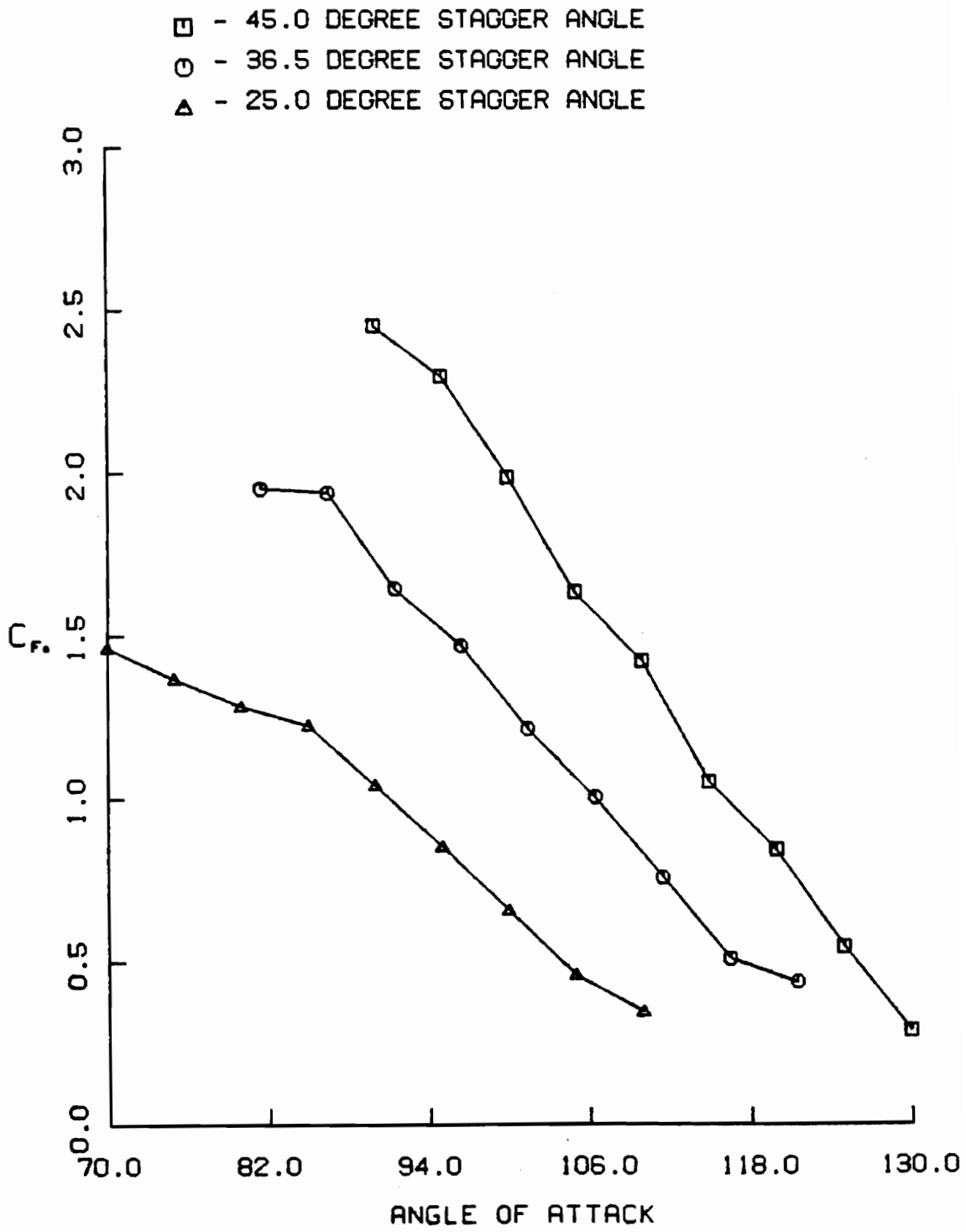

Figure 35. NSA Blade Tap Normal Force Coefficient

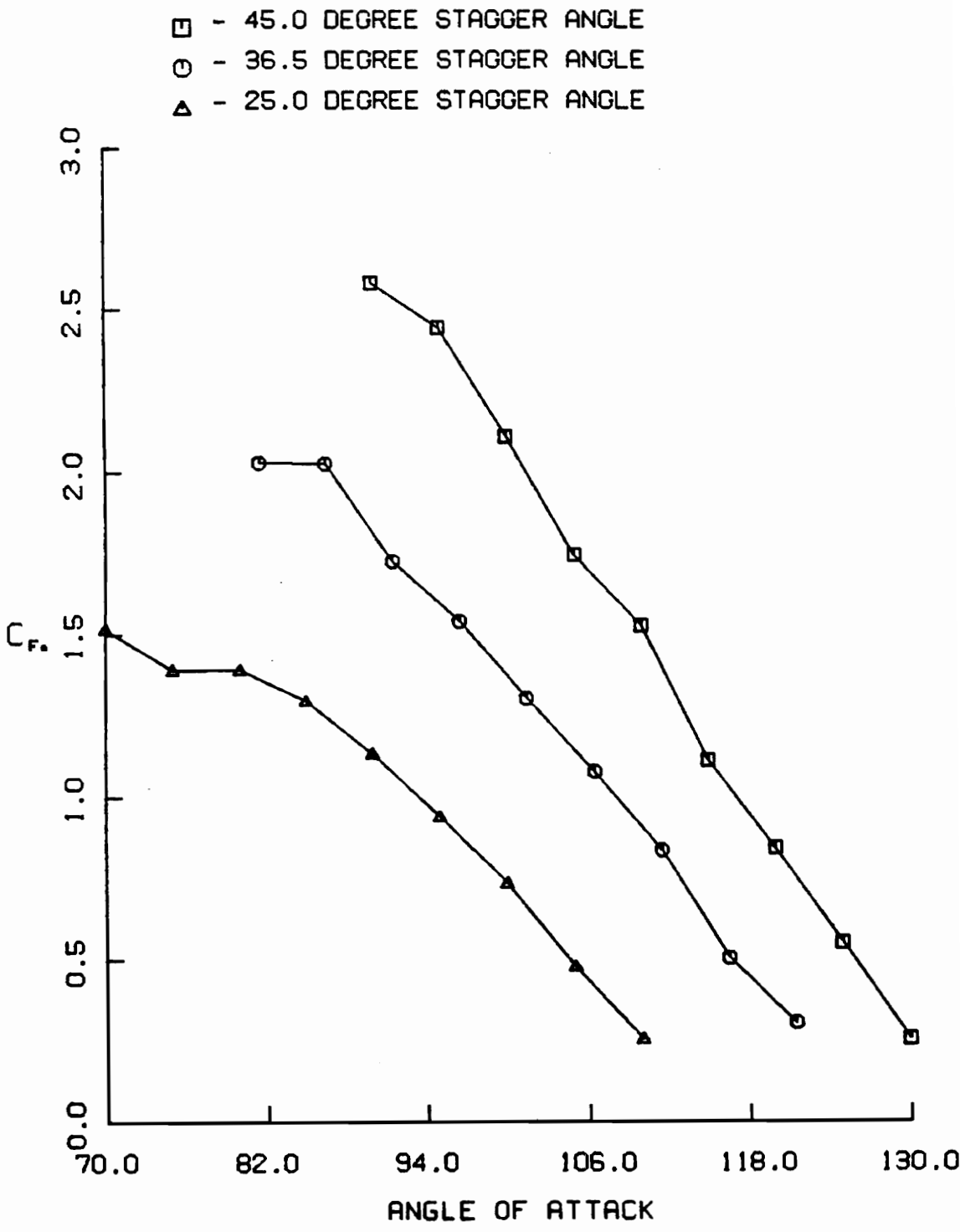

Figure 36. NSA Momentum Equation Normal Force Ceofficient

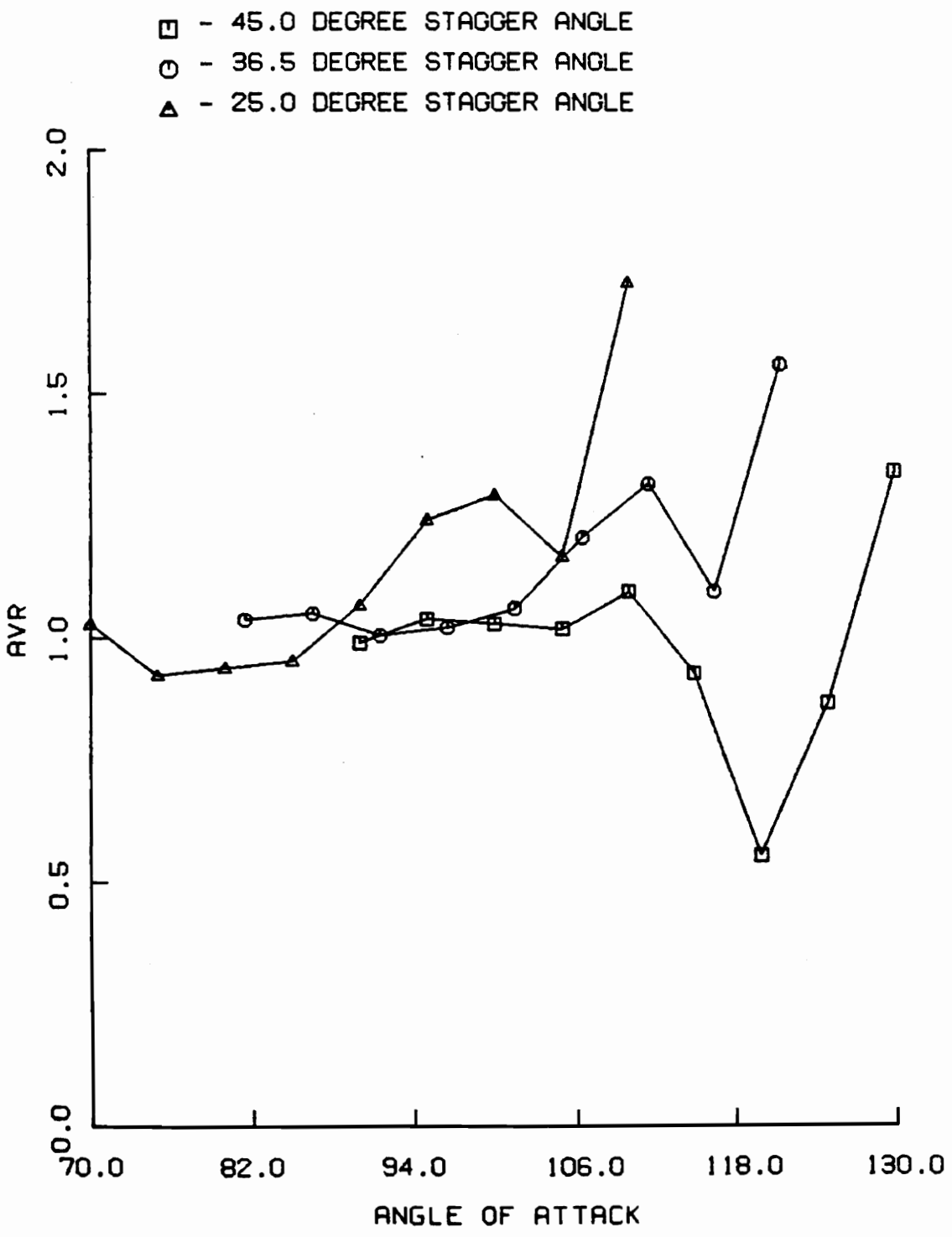

Figure 37. NSA Axial Velocity Ratio

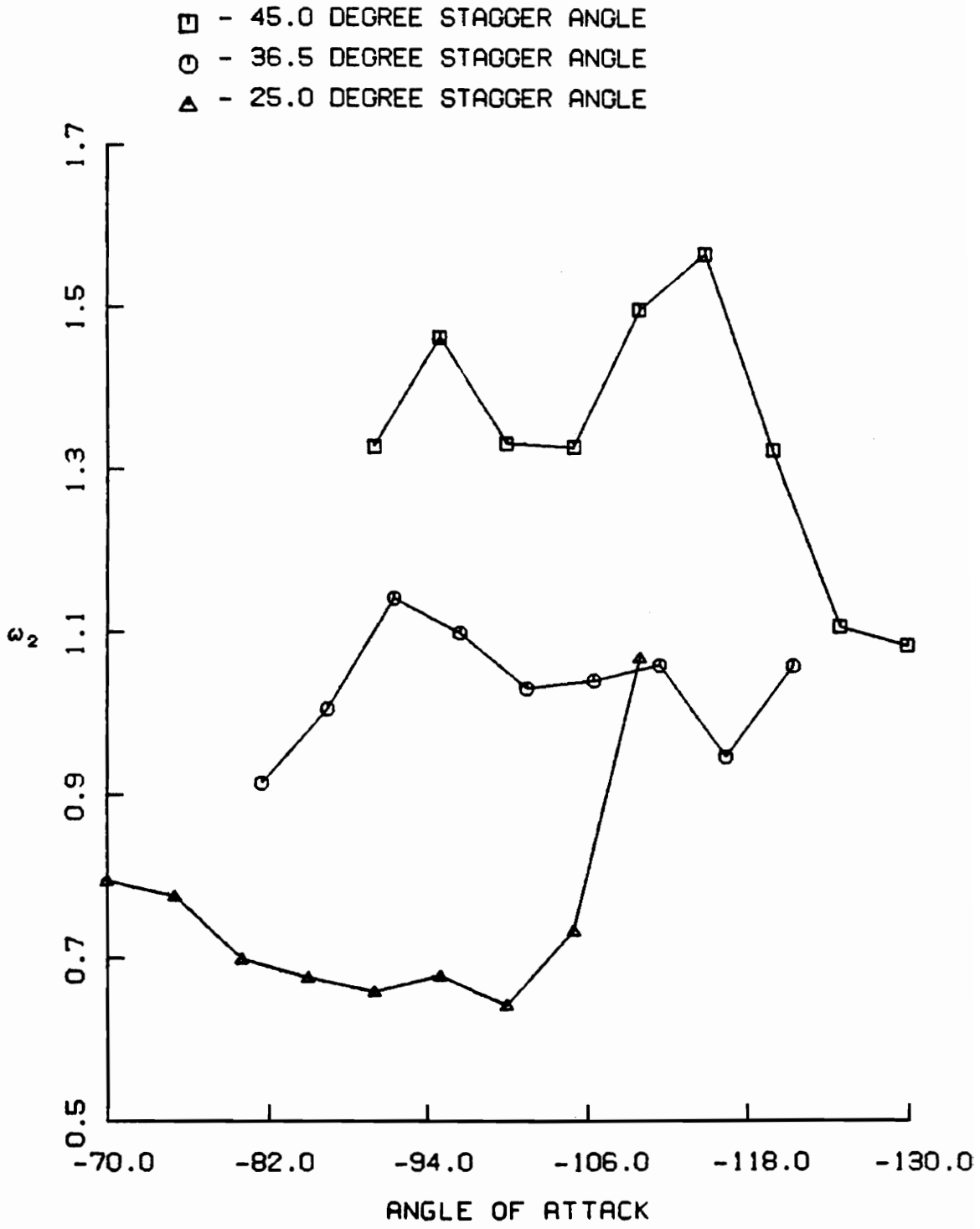

Figure 38. PSA Station 2 Mass Averaged Total Pressure Loss

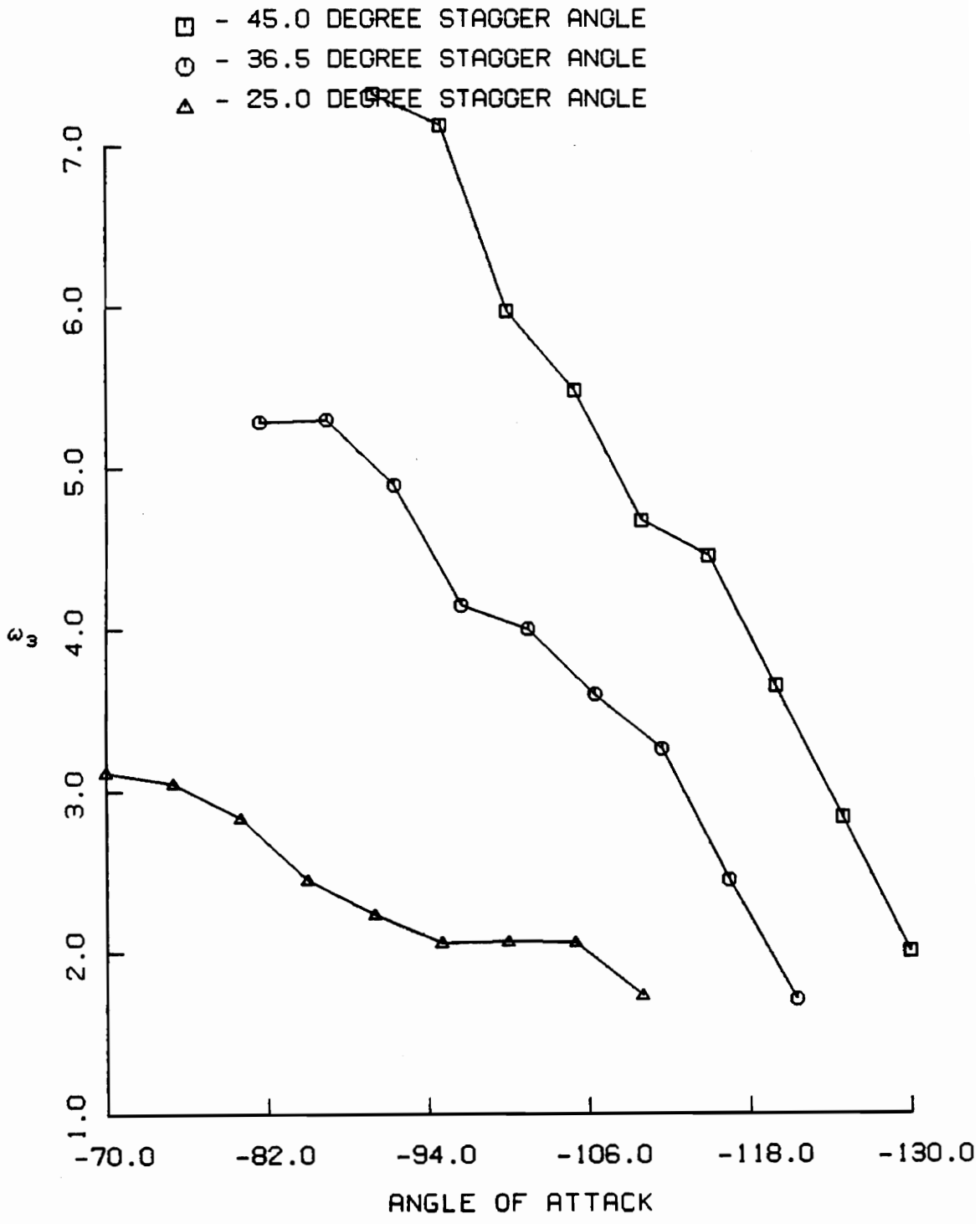

Figure 39. PSA Station 3 Mass Averaged Total Pressure Loss

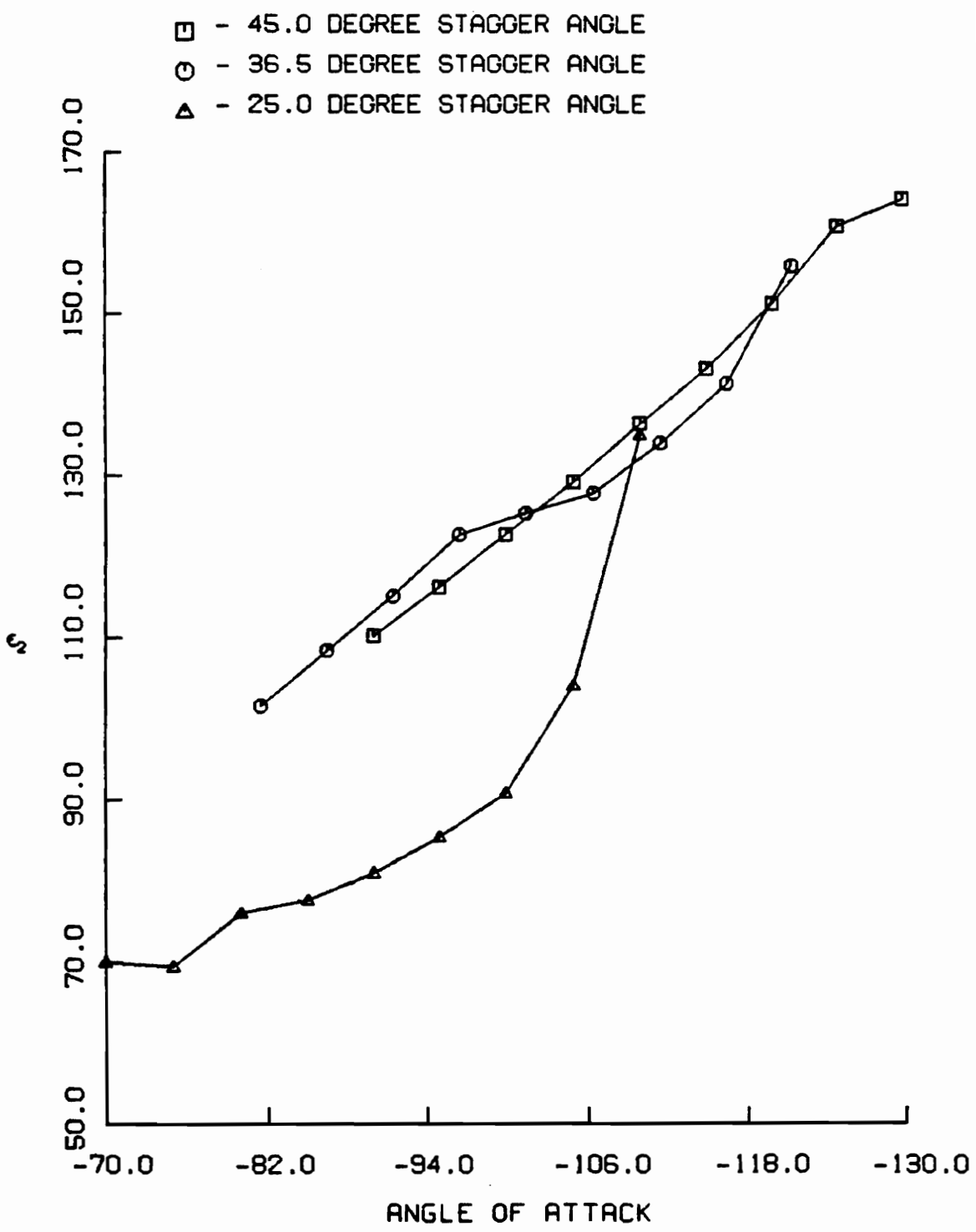

Figure 40. PSA Station 2 Mass Averaged Turning Angle

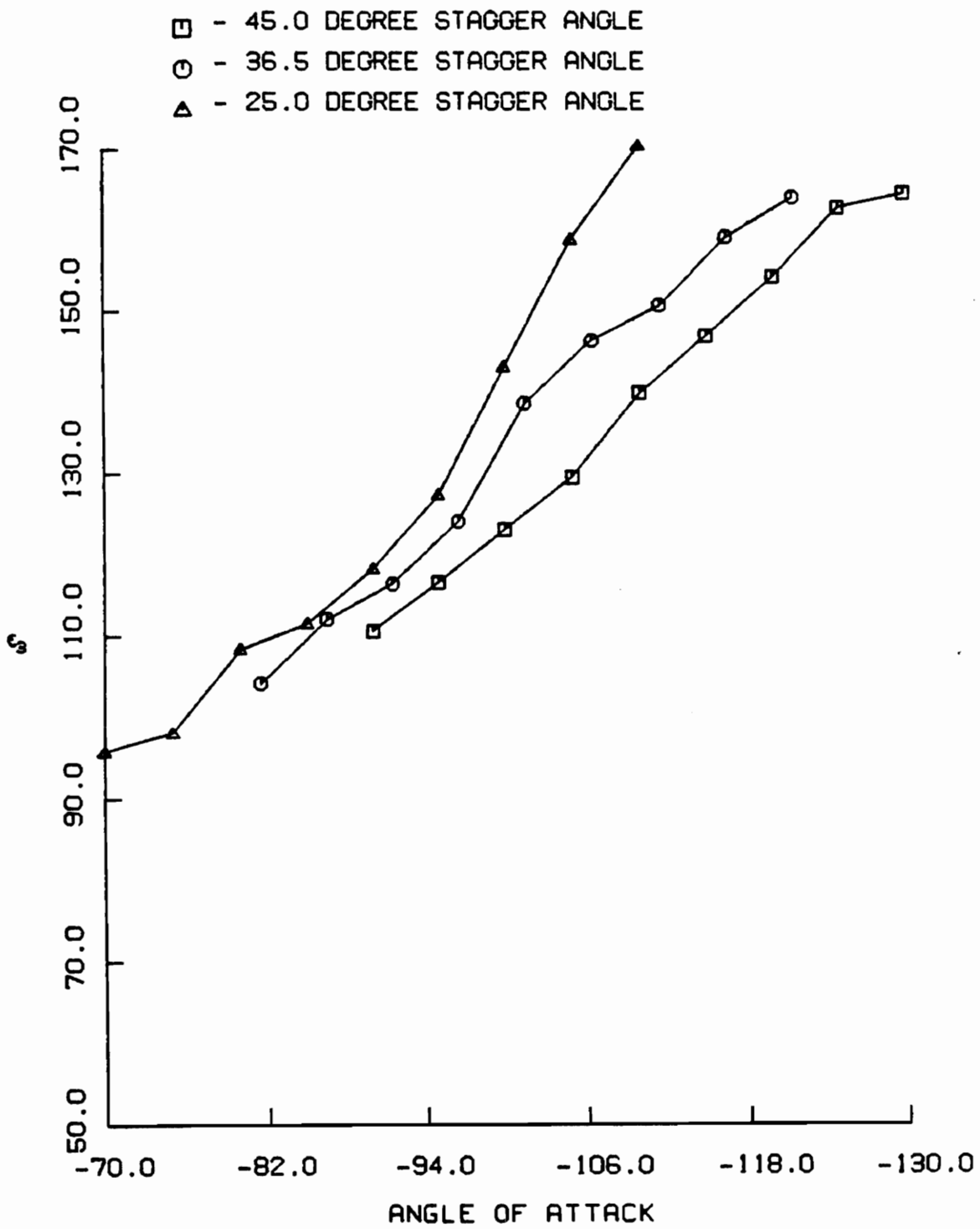

Figure 41. PSA Station 3 Mass Averaged Turning Angle

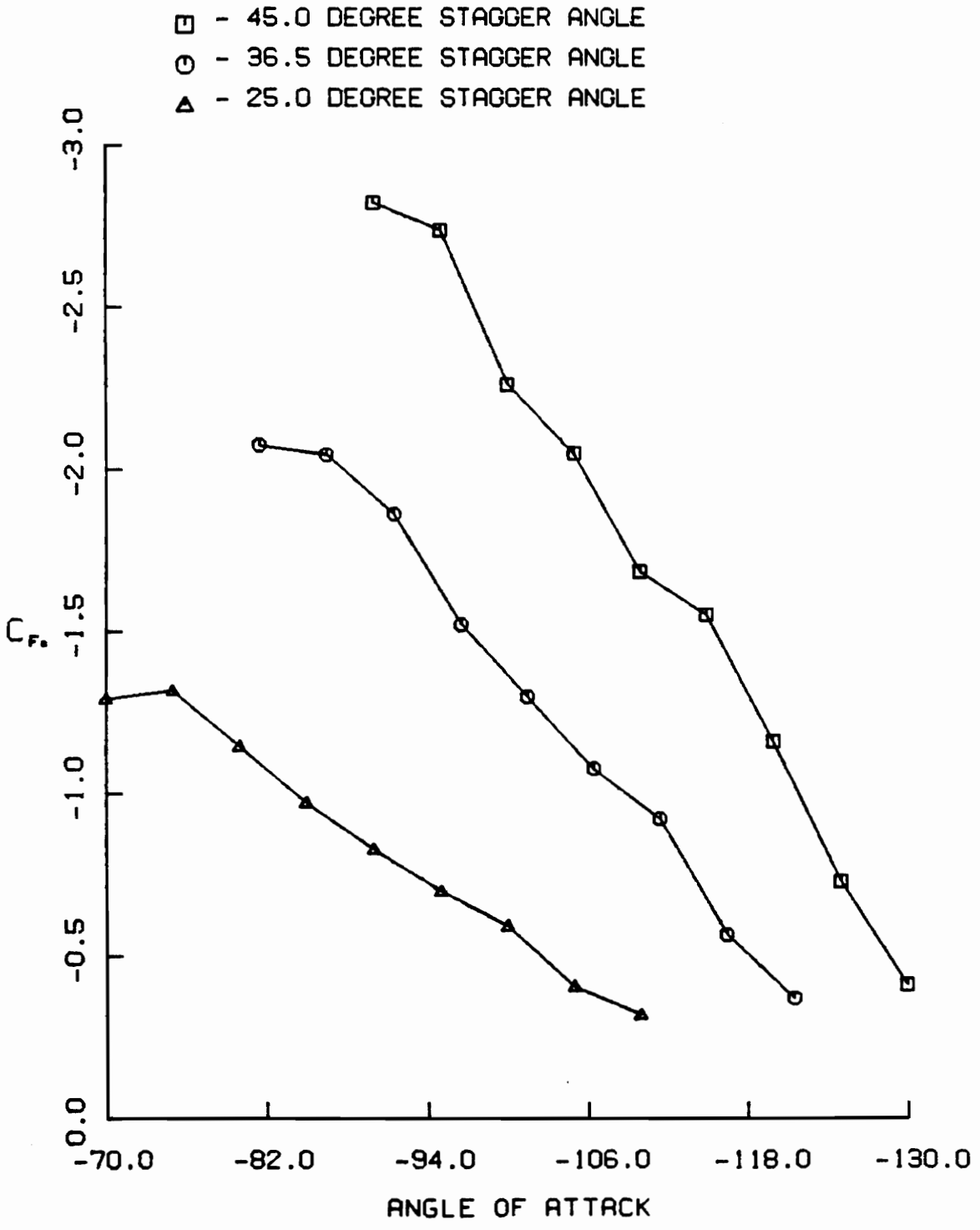

Figure 42. PSA Blade Tap Normal Force Coefficient

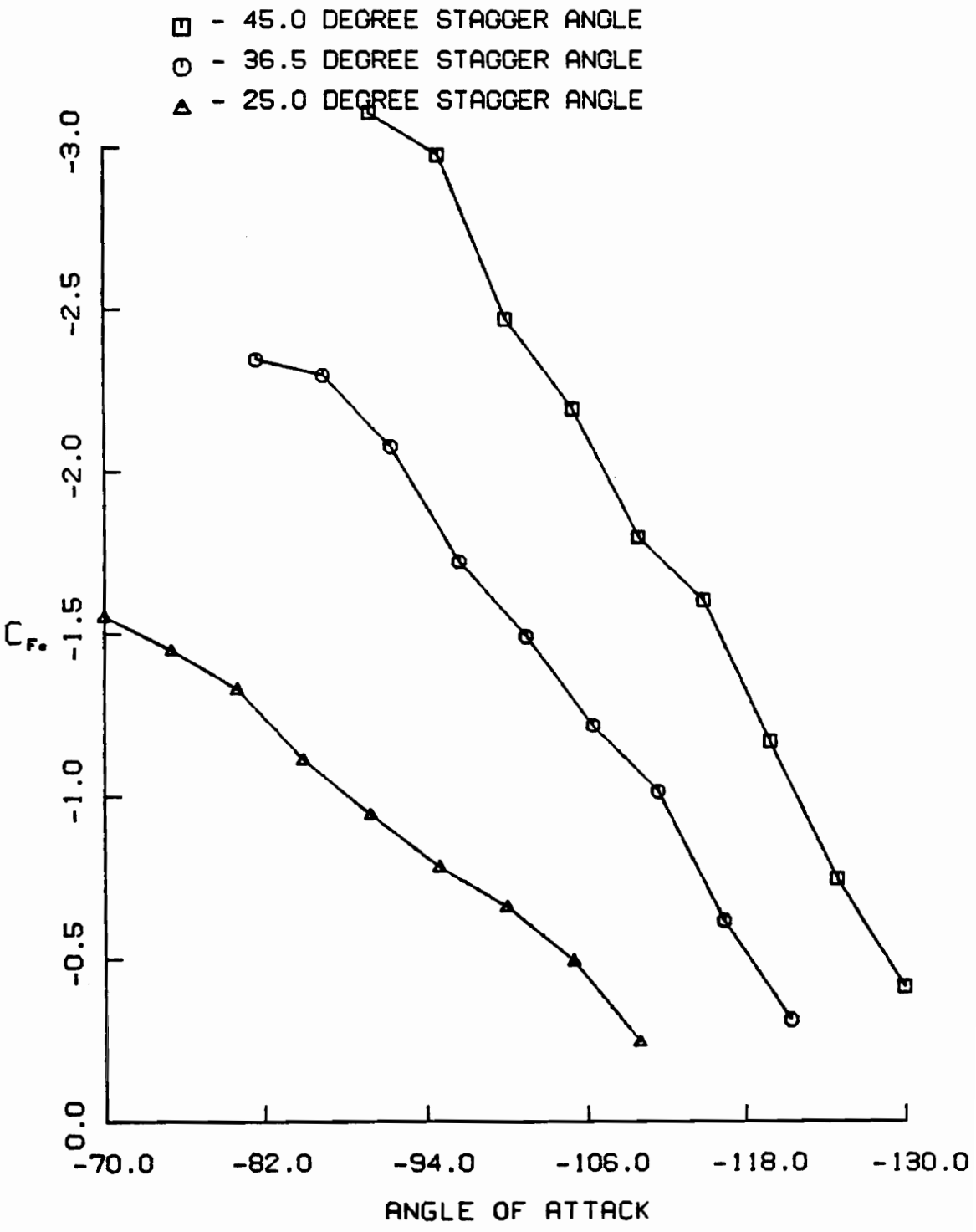

Figure 43. PSA Momentum Equation Normal Force Ceofficient

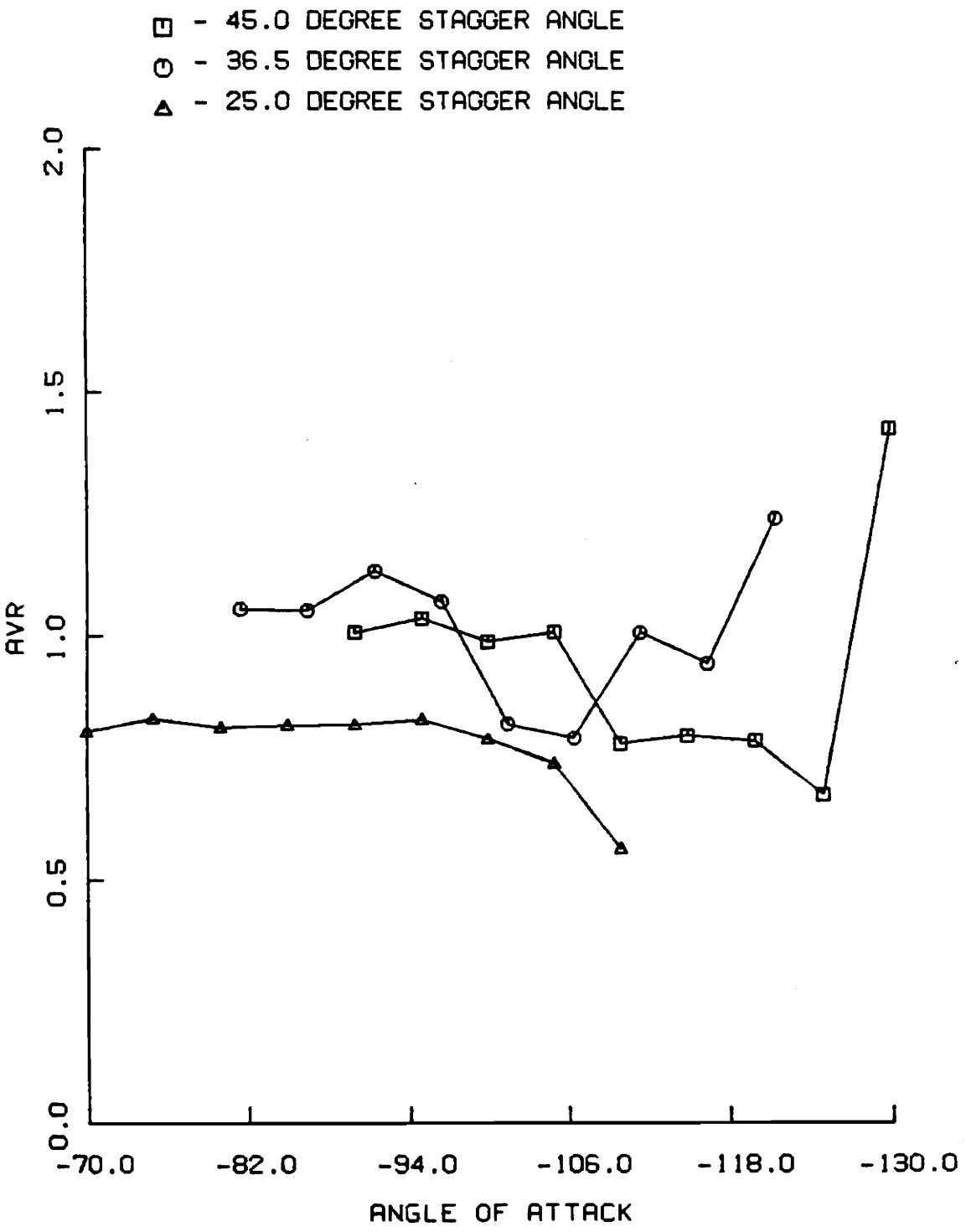

Figure 44. PSA Axial Velocity Ratio

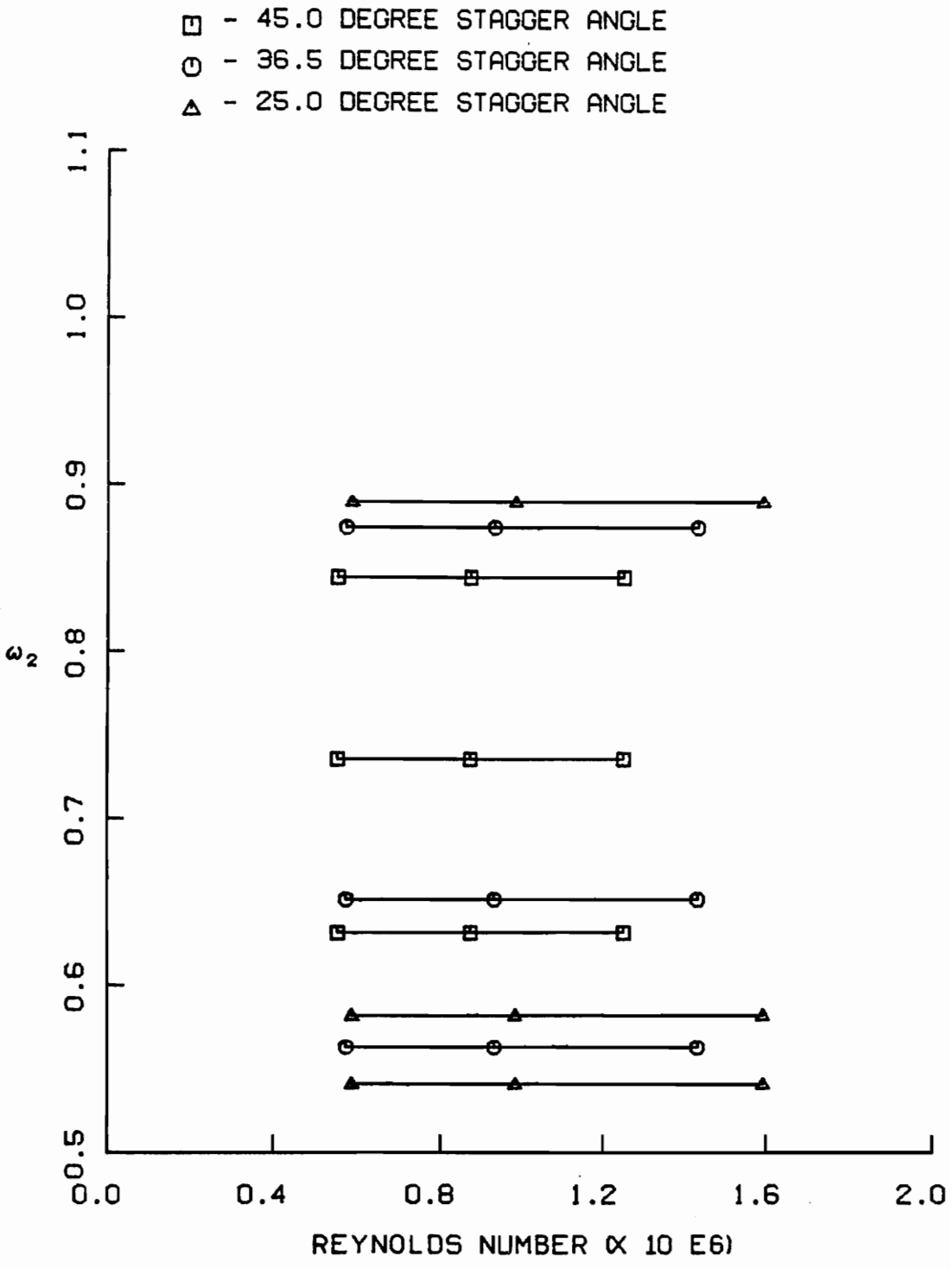

Figure 45. NSA Station 2 MATPL versus Reynolds Number

8.0 DISCUSSION OF RESULTS

The discussion of results is an attempt to interpret the calculated results in terms of individual test results and to explain observed trends based on established flow behavior.

The discussion will make several references to the individual test results, the calculated test results and the aerodynamic performance parameters.

First, a simplified model of a cascade is discussed to show what type of flow behavior might be expected.

Following the arrangement used in Chapters 6 and 7, the discussion of calculated flow data is organized into two groups:

Group I) data for negative stagger angle and positive angle of attack.

Group II) data for positive stagger angle and negative angle of attack.

After the Group I and Group II discussion, the station 3 mass averaged total pressure loss is compared with experimental data from another source.

8.1 SIMPLIFIED CASCADE MODEL

A discussion of a simplified model of a cascade is presented to show what type of flow behavior might be expected from a cascade in reversed flow. Referring to Figure 46 and Figure 47, the flow enters the cascade through area A_1, and exits through area A_2. It is suggested that the area ratio, A_2/A_1, links the behavior of certain aerodynamic performance parameters.

Figure 46 shows the simplified model with a relatively small area ratio (A_2/A_1)

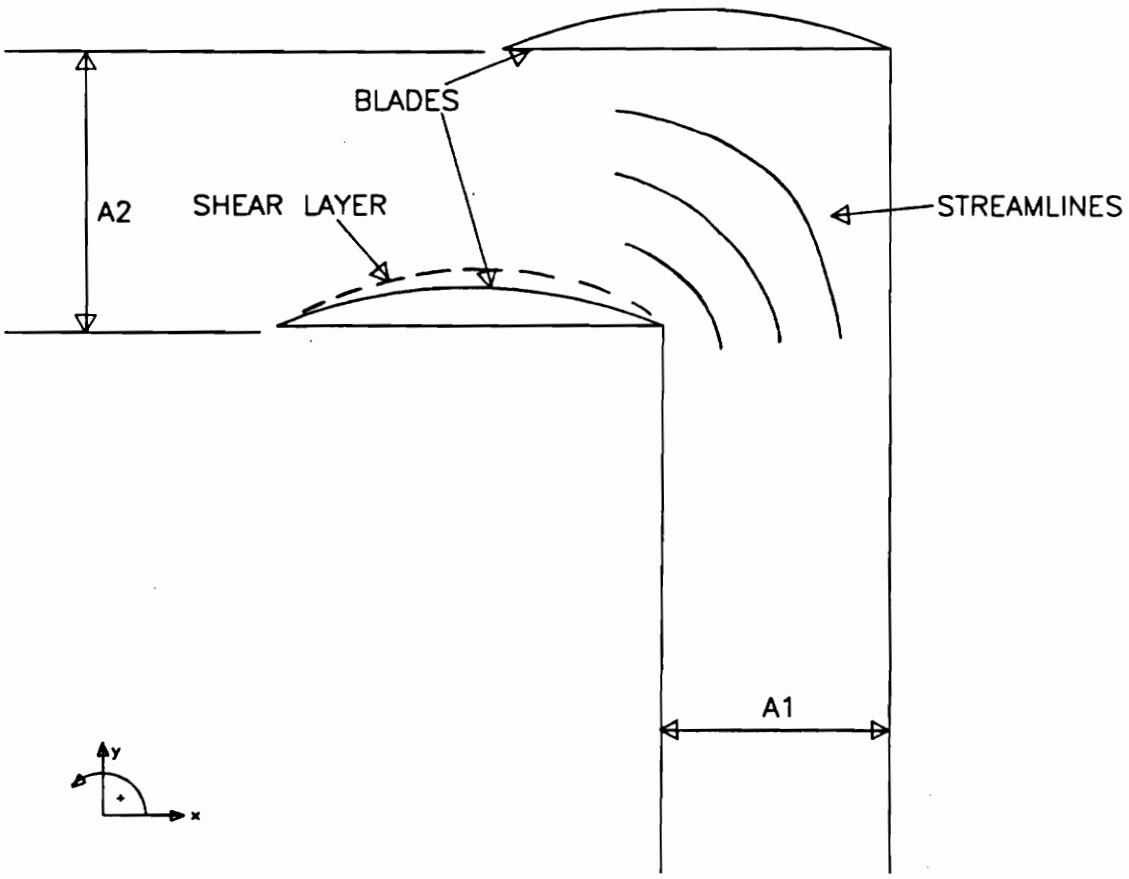

Figure 46. Simplified Cascade Model; A_2/A_1 is Small

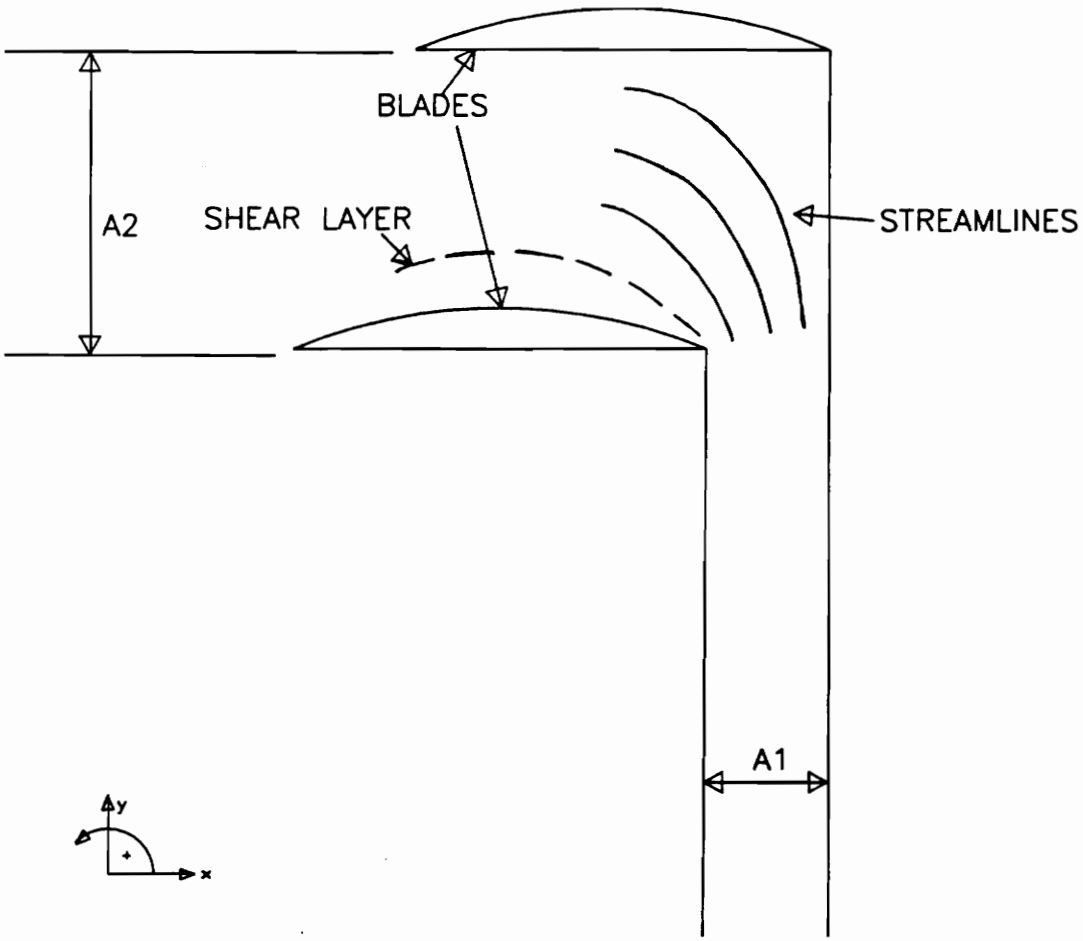

Figure 47. Simplified Cascade Model; A_2/A_1 is Large

compared to Figure 47. The inlet flow enters the blade passage through area A_1. Since the area ratio is relatively small and the flow is not throttled (jetted), there is little total pressure loss and expansion at the blade entrance, compared to a model with a higher area ratio. This low pressure loss leads to a smaller shear layer in the blade passage, but also produces a high total pressure gradient (in the y-direction) at the blade passage exit, compared to a model with a higher area ratio.

As seen in Figure 46, the area ratio is relatively large, compared to Figure 47. Since the area ratio is relatively large and the flow is throttled (jetted), there is more total pressure loss and more expansion at the blade entrance, compared to a model with a lower area ratio. The high pressure loss leads to a larger shear layer in the blade passage, while producing a lower total pressure gradient at the blade passage exit, compared to a model with a lower area ratio.

Figure 48 displays the geometry for the visualization of cascade area ratio versus angle of attack and stagger angle. For a given angle of attack, as stagger angle increases, the area ratio decreases (F/E<B/A). For a given stagger angle, as angle of attack increases, the area ratio increases(D/C>B/A).

The general trends of aerodynamic performance parameters may be related to the flow behavior seen in the simplified model as follows. Mass averaged total pressure loss at station 2 is related to the total pressure loss at the blade entrance. An increase in blade entrance total pressure loss should produce an increase in station 2 mass averaged total pressure loss. A larger shear layer in the blade passage should make the flow turn more

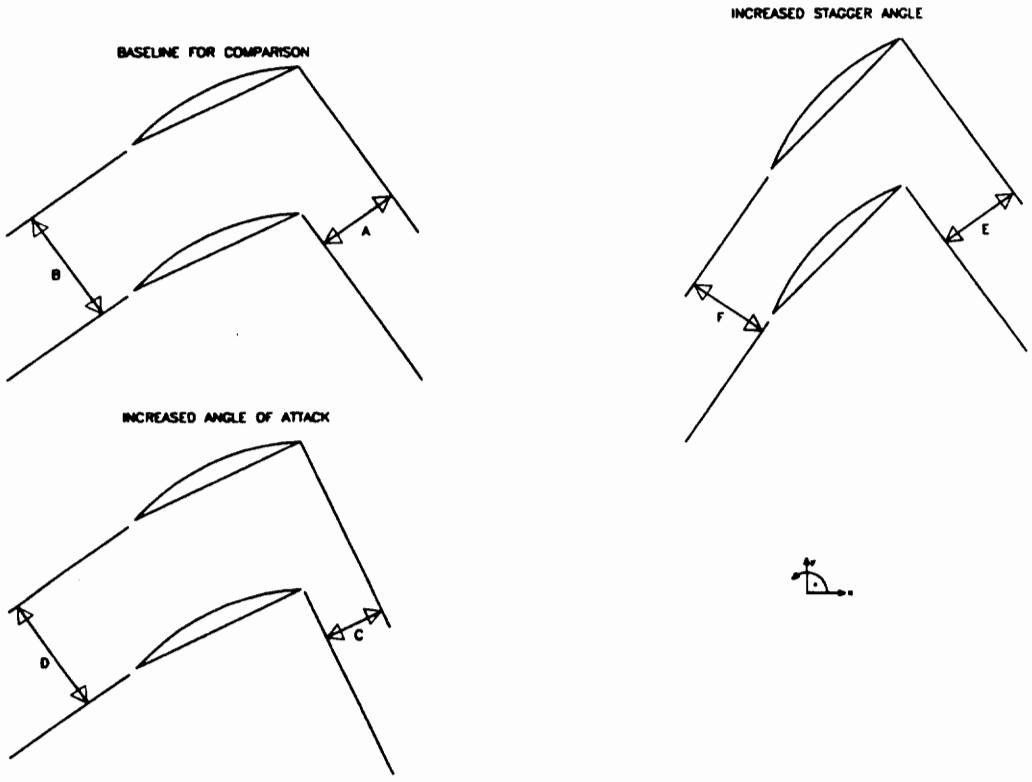

Figure 48. Cascade Area Ratio

in the blade passage. A higher pressure gradient at the blade passage exit should increase the possibility of backflow at the blade passage exit. This increase in backflow should in turn increase station 3 mass averaged total pressure losses.

Assuming the flow through area A_1 is at a constant velocity, then the mass flow though a smaller area will be less than through a larger area, from the continuity equation (density is constant). Less mass flow will in turn mean lower normal force coefficients, C_{Fn}, from the momentum equation.

By combining the effects of area ratio on the simplified model flow behavior, the effects of stagger angle and angle of attack on the simplified model area ratio, and the effects of the simplified model flow behavior on aerodynamic performance parameters, the effects of stagger angle and angle of attack on the performance parameters for the simplified model can be stated. Station 2 mass averaged total pressure loss should increase with increasing angle of attack, and decrease with increasing stagger angle. Turning angles should increase with decreasing stagger angle. Station 3 mass averaged total pressure loss should increase with decreasing angle of attack and increase with increasing stagger angle. Finally, normal force coefficients should decrease with increasing angle of attack.

8.2 NEGATIVE STAGGER ANGLE (GROUP I)

Station 3 mass averaged total pressure loss, ω_3, is considered the best measurement of cascade losses. Station 2 mass averaged total pressure loss is a measure of total pressure loss directly after the cascade, where wakes and backflow exist. Although ω_2

measures the total pressure loss, it does not account for backflow losses. Station 3 mass averaged total pressure loss accounts for these backflow losses since the flow is mixed-out to a uniform velocity and pressure profile. Without the wakes and backflow, ω_3 has the added advantage of being directly comparable to total pressure loss data from other cascades.

The station 2 mass averaged total pressure loss trends match those expected from the simplified cascade model. Therefore, the observed ω_2 trend is thought due to the initial expansion (jetting) in the entrance to the blade passage.

The trend of ω_3 versus angle of attack and stagger angle is related to the amount of backflow in a cascade. The possibility of backflow increases with increased pressure gradient in the direction of flow. As can be seen in the blade suction side C_{ps}, the pressure gradient decreases with increasing angle of attack, thereby indicating less backflow. Less backflow means lower losses, therefore it is expected that ω_3 would decrease with increasing angle of attack. This trend matches the expected flow behavior from the simplified cascade model.

Also, the blade suction side C_{ps} gradient increases with increasing negative stagger angle, thereby indicating more backflow at higher negative stagger angles. Therefore it is expected that ω_3 would increase with increasing negative stagger angle. This agrees with the trend expected from the simplified cascade model.

Station 2 and station 3 mass averaged turning angle results, ε_2 and ε_3, respectively, can be explained as follows. The more the geometry requires turning

(increased the angle of attack), the more the flow will turn (increased ε_2 and ε_3). Therefore it is logical that the calculated results of ε_2 and ε_3 increase with increasing angle of attack.

The ε_2 and ε_3 results versus stagger angle match the trend predicted by the reasoning associated with the simplified cascade model. Therefore, the explanation for increased turning with decreased negative stagger angle is increased turning within the blade passage at lower negative stagger angles.

The calculated momentum equation normal force coefficient results correspond to the trends set by the normal force coefficient calculated from the blade pressure tap measurements. Corresponding trends between results calculated from different experimental data is a good indication of the integrity of the calculated results.

Both normal force coefficients agree with the expected results of decreasing C_{Fn} with increasing angle of attack. This is a result of less mass flow through the blade at higher angle of attacks.

The axial velocity ratio is an indication of the three dimensionality of the flow. If the axial velocity ratio remains near the desirable value of one, the flow is interpreted to be two dimensional. At high angles of attack, the axial velocity ratio departs from the desirable value of one for all negative stagger angles. This would indicate three dimensional flow at high angles of attack. Since high angles of attack mean low non-dimensional axial velocity, Vx/U, an indication of three dimensional flow is seen at a low Vx/U. Three dimensional flow behavior at low Vx/U is acknowledged as an expected

situation from other research[13].

8.3 POSITIVE STAGGER ANGLE (GROUP II)

In general, the positive stagger angle calculated results behave in the same manner as the negative stagger angle calculated results with a few exceptions, which will be pointed out.

The lack of trend for ω_2 versus angle of attack is not understandable and perhaps due to the large amount of backflow occurring in the 25 and 36.5 degree positive stagger angles.

The trend of ω_3 versus angle of attack and stagger angle is related to the amount of backflow in a cascade. The possibility of backflow increases with increased pressure gradient in the direction of flow. As can be seen in the blade suction side C_{ps}, the pressure gradient decreases with increasing negative angle of attack, thereby indicating less backflow. Less backflow means lowers losses, therefore it is expected that ω_3 would decrease with increasing negative angle of attack. This trend matches the expected flow behavior from the simplified cascade model.

Also, the blade suction side C_{ps} gradient increases with increasing stagger angle, thereby indicating more backflow at higher stagger angles. Therefore it is expected that ω_3 would increase with increasing stagger angle. This agrees with the trend expected from the simplified cascade model.

Station 2 and station 3 mass averaged turning angle results, ε_2 and ε_3, respectively, can be explained as follows. The more the flow geometry requires turning

(increase the angle of attack), the more it will turn (increased ε_2 and ε_3). Therefore it is logical that the calculated results of ε_2 and ε_3 increase with increasing negative angle of attack.

The ε_2 and ε_3 results versus stagger angle match the trend predicted by the reasoning associated with the simplified cascade model. Therefore, the explanation for increased turning with decreased positive stagger angle is increased turning within the blade passage at lower positive stagger angles.

The odd trend for the 25 degree positive stagger angle ε_2 versus angle of attack is probably due to the large amount of backflow occurring in the 25 degree positive stagger angle tests.

The calculated momentum equation normal force coefficient results correspond to the trends set by the normal force coefficient calculated from the blade pressure tap measurements. Corresponding trends between results calculated from different experimental data is a good indication of the integrity of the results.

Both normal force coefficients agree with the expected results of decreasing C_{Fn} with increasing angle of attack. This is a result of less mass flow through the blade at higher angle of attacks.

The axial velocity ratio is an indication of the three dimensionality of the flow. If the axial velocity ratio remains near the desirable value of one, the flow is interpreted to be two dimensional. At high negative angles of attack, the axial velocity ratio departs from the desirable value of one for all positive stagger angles. This would indicate three

dimensional flow at high negative angles of attack.

The odd trend for the 25 degree positive stagger angle axial velocity ratio versus angle of attack is probably due to the large amount of backflow occurring in the 25 degree positive stagger angle tests.

8.4 DISCUSSION OF MASS AVERAGED LOSS ω_3

The determination of the mass averaged losses, ω_3, is very important to the application of the results of this thesis. In Figure 49, the entire set of ω_3 results (non-dimensionalized by compressor wheel speed instead of cascade inlet velocity) is plotted with Vx/U as abscissa, as would be seen for a compressor characteristic. Values for Vx/U and ω_{3corr} were determined from velocity triangles and angle of attack values, following Figure 5 and Appendix B. Note that the curves are similar except for the 25 degree positive stagger angle. This is a fortunate result, since the blade rows of a compressor may be treated as nearly-equal loss producers, simplifying the use of ω_3 for reversed flow characteristic predictions. An example of this use and a comparison with experimental data is given in Section 8.4.1.

8.4.1 EXPERIMENTAL COMPARISON

Comparison of the experimental results presented in this thesis is limited due to the lack of experimental reversed flow literature. The ω_3 results from this thesis are compared with results from the Gamache[5] dissertation. Gamache[5] defines a total pressure coefficient,ψ_{tt}, and a torque coefficient, ψ_τ, as follows:

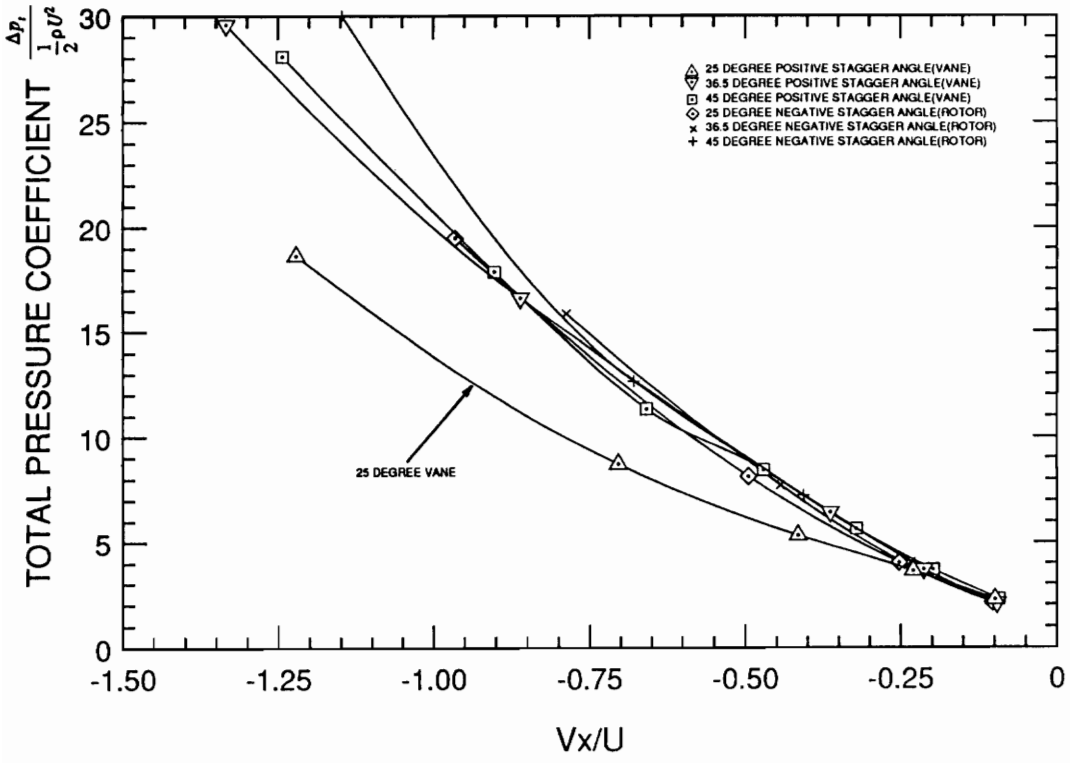

Figure 49. Corrected Loss Coefficient ω_3 Results

$$\psi_{tt} = \frac{\Delta p_t}{\frac{1}{2}\rho U^2} \qquad \psi_\tau = \frac{\tau}{\frac{1}{2}\rho U^2 A_c R_m}$$

where τ is the torque input to the compressor, Ac is the compressor annulus area, Rm is the mean radius, and U is the mean compressor wheel speed.

Using the total pressure coefficient graph, ψ_w, and the torque coefficient, ψ_τ, provided in the Gamache[5] dissertation, a pressure loss can be calculated in the following way. The energy input into the compressor, ψ_τ, produces an ideal temperature rise across the compressor, which is calculated by:

$$\psi_\theta = \frac{\psi_\tau}{\left(\frac{V_x}{U}\right)} = \frac{\Delta T_t}{\frac{1}{2}\frac{U^2}{C_p}}$$

where ψ_θ is the temperature coefficient and Cp is the specific heat capacity at constant pressure.

Assuming that the state of air is known to be atmospheric at the compressor exit (normally the compressor inlet, state 1) during reversed flow (while the compressor system is in surge), the ideal temperature for the entering reversed flow can be calculated:

$$T_{t2} = T_{t1} + \frac{1}{2}\frac{U^2}{C_p}\psi_\theta$$

Therefore, from the relation of isentropic processes:

$$p_{t2s} = p_{t1}\left(\frac{T_{t2}}{T_{t1}}\right)^{\frac{\gamma}{\gamma-1}}$$

the ideal pressure, p_{t2s}, can be found. From this information, a non-dimensional ideal pressure coefficient:

$$\psi_{ideal} = \frac{\Delta p_t}{\frac{1}{2}\rho U^2}$$

can be calculated. By knowing the measured total pressure coefficient ψ_{tt} and the ideal pressure coefficient ψ_{ideal}, the total pressure loss coefficient ψ_l is calculated as follows:

$$\psi_l = \psi_{ideal} - \psi_{tt}$$

The loss coefficient ψ_l is not directly comparable to the mass averaged total pressure loss presented earlier, ω_3. The loss coefficient ψ_l is a total loss across a 3-stage compressor, whereas ω_3 is a loss across one blade row. Therefore, the losses across a 3-stage compressor must be predicted from the ω_3 data.

First, ω_3 must be calculated in terms of Vx/U and non-dimensionalized by the compressor wheel speed instead of the cascade inlet velocity, which is detailed in Appendix B, giving ω_{3corr}. A prediction for the losses across a 3-stage compressor can be

found by multiplying the losses across one blade row by the number of blade rows in a three stage compressor. Gamache's[5] three stage compressor had an inlet guide vane, three rotors and three stators. The inlet guide vane may be approximated as a stator in reversed flow. This assumption is supported by Figure 49 where positive stagger angle (vane) results are similar to the negative stagger angle (rotor) results. The reversed flow entering the third stage stator of the Gamache[5] 3-stage compressor meets the last stator blade at a relatively low angle of attack (approximately 20 degrees), therefore it is assumed that the losses of this blade row should not be considered. From these arguments, the effective number of blade rows in the 3-stage compressor is six. Therefore, the predicted loss ω_{3pr} should be equal to six times the corresponding ω_{3corr} loss value.

Figure 50 compares the ω_{3pr} loss predictions developed by the above method with the losses calculated from the Gamache[5] dissertation results for the limited range of compressor reversed flow data. The results are considered similar in trend and magnitude. For this compressor, use of the present cascade results provides a reasonable approximation of the measured reversed flow losses.

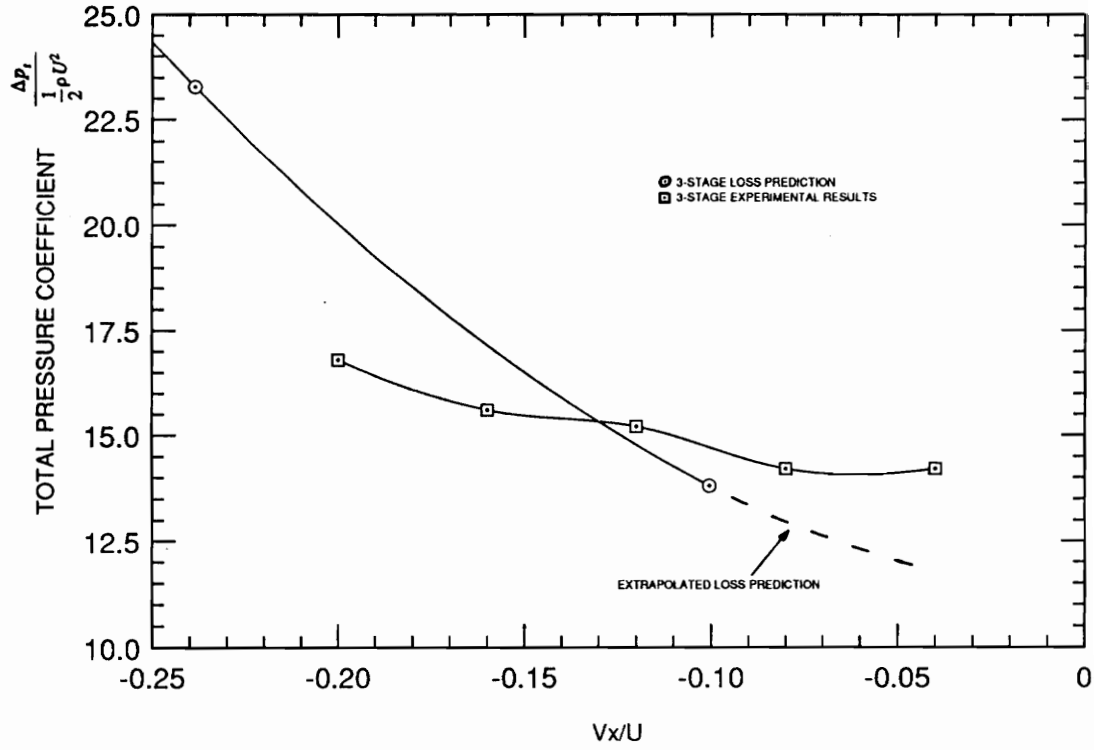

Figure 50. Comparison of Loss Predictions with Experimental Results

9.0 CONCLUSIONS

The effect of stagger angle on negative stagger angle performance of the cascade at these extremely high angles of attack is evident from a study of the results. The higher negative stagger angles produce increased mixed-out total pressure losses and increased blade loading with respect to lower negative stagger angles, while the turning angles are lower.

The effect of angle of attack on negative stagger angle performance is as follows. The higher angles of attack have decreased mixed-out total pressure losses and increased turning angles with respect to lower angles of attack, while the blade loading is lower due to less mass flow though the blade passage.

The effect of stagger angle on positive stagger angle performance of the cascade is apparent. The higher positive stagger angles have increased mixed-out total pressure losses and increased blade loading with respect to lower positive stagger angles, while the turning angles are lower.

The effect of negative angle of attack on positive stagger angle performance is as follows. The higher negative angles of attack have decreased mixed-out total pressure losses and increased turning angles with respect to lower negative angles of attack, while the blade loading due to less mass flow though the blade passage is lower. There was no noticeable trend of unmixed total pressure losses versus negative angle of attack.

In general, the negative stagger angle calculated results show the same trends as the positive stagger angle calculated results, as might be expected for these very high

angle of attack flows.

Agreement between blade tap and momentum equation normal force coefficient trends is good, indicating integrity of the calculated results.

Reynolds number had no effect on the calculated values of the aerodynamic performance parameters for the range of 60000 to 200000, based on blade chord.

Agreement of ω_{3corr} curves suggests that blade rows of a compressor subjected to reversed flow may be treated as nearly equal loss producers.

A comparison was made between total pressure loss coefficients of this investigation and experimental compressor performance. The total pressure loss coefficients compared favorably in magnitude and curve shape.

10.0 RECOMMENDATIONS

This investigation has revealed a number of areas of research that would further support the findings in this report.

Flow visualization was attempted on this investigation using the technique of smoke illuminated with laser light. Due to insufficient light levels no results were forthcoming. Since the smoke injection apparatus is present on the cascade, finding a light source capable of providing enough light for high speed motion pictures is pertinent. Once these motion pictures can be taken, the actual mechanisms of boundary layer separation can be seen.

The main outcome of these tests is to provide reversed flow stage characteristics for computer models. These models rely on stage characteristics to emulate real time performance. Using these performance parameters versus angle of attack, a stage characteristic can be generated by converting angle of attack to flow coefficient, Vx/U. This is done using the geometry and velocity vector triangles of the model in use. This process is detailed in Appendix B.

The agreement of ω_{3corr} curves in Figure 49 suggests that a fundamental theory should exist predicting the losses encountered during reversed flow. The determination of this theory should receive attention.

REFERENCES

1. Emmons, H.W.; Pearson, C.E.; and Grant, H.P.; "Compressor Surge and Stall Propagation", *Transactions of the American Society of Mechanical Engineers*, April 1955, No.77, p 455-469

2. Greitzer, E. M.,; "Surge and Rotating Stall in Axial Flow Compressors, Part 1: Theoretical Compression System Model", ASME Paper No. 75-GT-9, 1975

3. Greitzer, E.M.; "Surge and Rotating Stall in Axial Flow Compressors, Part 2: Experimental Results and Comparison with Theory", ASME Paper No. 75-GT-10, 1975

4. Turner, R.C., and Sparkes, D.W.; "Complete Characteristics for a Single-Stage Axial Flow Fan", Thermodynamics and Fluid Mechanics Convention, Paper 29, Apr. 1964

5. Gamache, R.N.; "Axial Compressor Reversed Flow Performance", Ph.D. Dissertation, MIT, May 1985.

6. Koff, S.G., and Greitzer, E.M.; "Axisymmetrically Stalled Flow Performance for Multistage Axial Compressors", ASME Journal of Turbomachinery, Vol. 108, October 1986, p 216-223

7. Davis, M. W. Jr.; "A Stage-by-Stage Post-Stall Compression System Modeling Technique: Methodology, Validation, and Application", Ph.D. Dissertation, VPI&SU, December, 1986.

8. Boyer, K.M., and O'Brien, W.F.; "Model Predictions for Improved Recoverability of a Multistage Axial-Flow Compressor", AIAA Paper No. 89-2687, 1989

9. Copenhaver, W.W.; "Stage Effects on Stalling and Recovery of a High-speed 10-stage Axial-flow Compressor", Ph.D. Dissertation, Iowa State University, October 1989

10. Yocum, A.M.; "An Experimental and Numerical Investigation of the Performance of Compressor Cascades with Stalled Flow", Ph. D. Dissertation, Mechanical Engineering, VPI&SU, May 1988

11. Ainslie, W.E.; "The Effect of Solidity on the Pre- and Post-Stall Flow in a Linear Compressor Cascade", M.S. Thesis, Mechanical Engineering, VPI&SU, August 1988

12. Tkacik, P.; "Cascade Performance of Double Circle Arc Compressor Blades at High Angles of Attack", M.S. Thesis, Mechanical Engineering, VPI&SU, 1982

13. O'Brien, W. F.,private communication, May 1990.

APPENDIX A

Due to the variance in cascade frontal area, a further contraction of the wind tunnel was needed. The design was required to satisfy the following criteria:

1) the contraction exit must be adjustable.

2) it must contract the flow smoothly.

3) it must provide a uniform velocity profile.

4) the boundary layers must be small so the test section center sees a uniform velocity profile.

The design for a third nozzle, shown in Figure 52, satisfies all of these criteria. Using a flexible plate that follows the contraction of the second tunnel, mounted flush to the second nozzle, provides smooth contraction of the flow with adjustability. The plate shape is shown in Figure 52. The plate is 0.032 inches thick which allows flexibility, but is stiff enough not to buckle when the wind tunnel is running. The flexible plates are mounted to an aluminum positioning block which is moved relative to the plate using two threaded rods and four nuts. The plate, detailed in Figure 52, has slots milled into it to allow the rods to move forward and backward. This is necessary to mount the flexible plate to the second nozzle.

Once the desired nozzle area is set, the nuts are tightened against each other causing the positioning block to be rigidly mounted to the plate. The plate is rigidly mounted to a connecting flange, and therefore to the wind tunnel itself.

Boundary layer tests were run on the tunnel when the flow was contracted to a

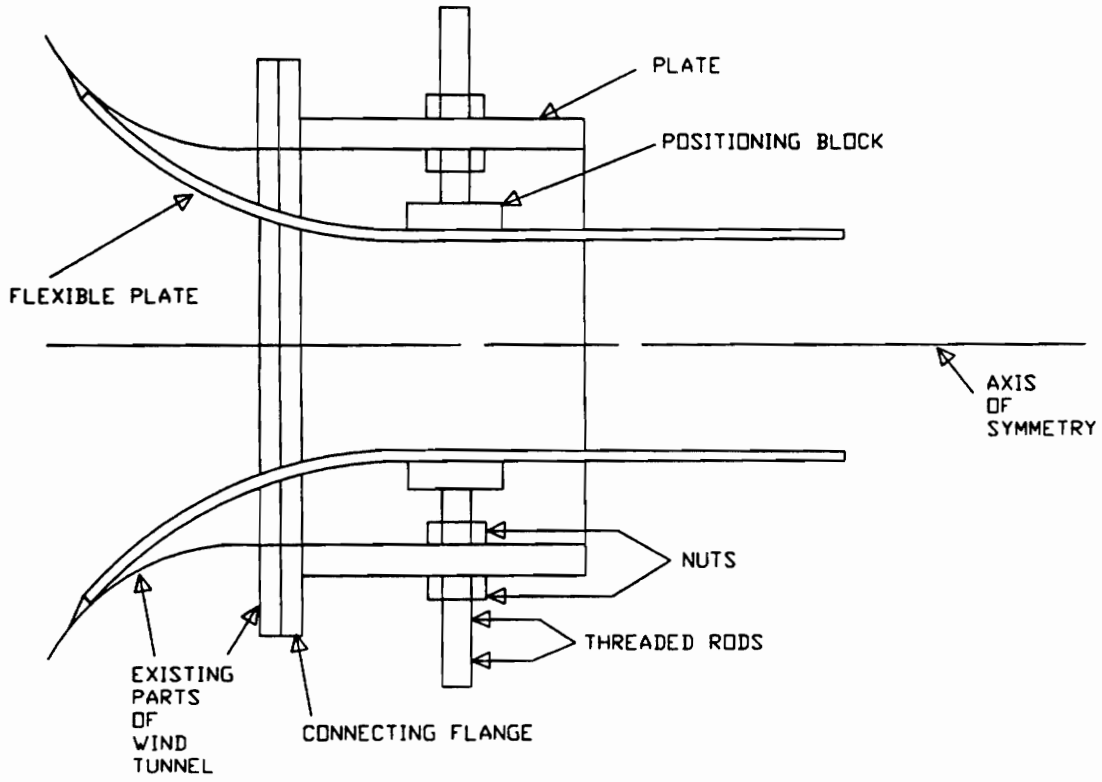

Figure 51. Variable Contraction Nozzle

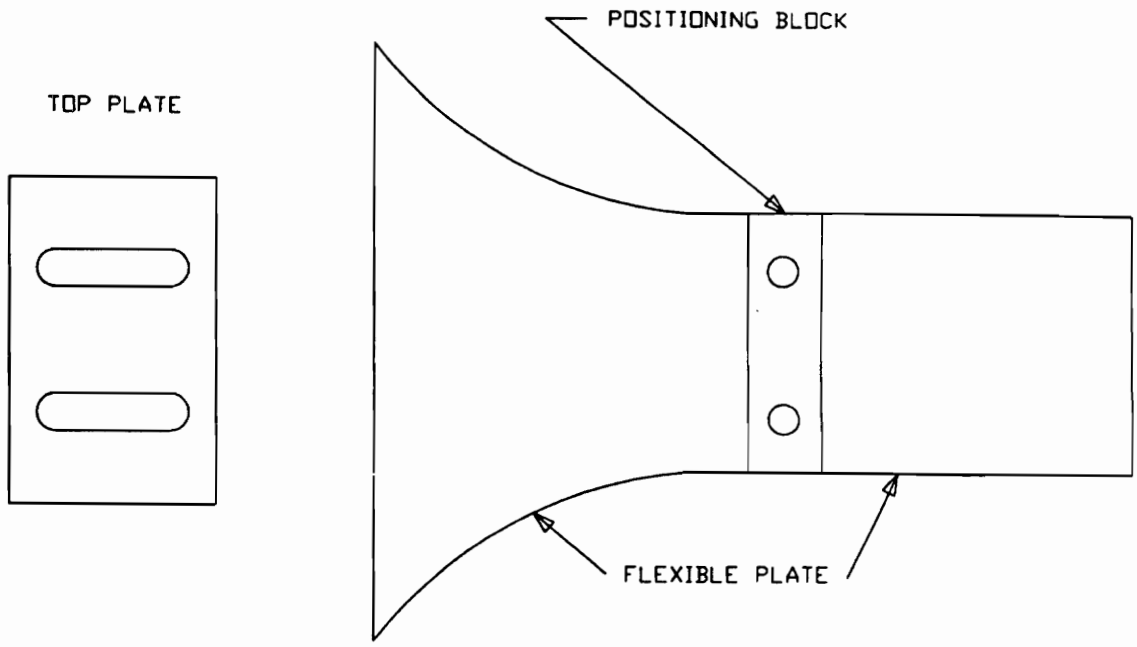

Figure 52. Variable Contraction Nozzle Details

nozzle height of 79.69 mm. Measurements were made 0.609 m downstream of the positioning blocks, and results are presented in Figure 53. As can be seen, the boundary layer has a thickness of 15.24 mm on both sides, leaving 49.21 mm of uniform flow in the center of the nozzle.

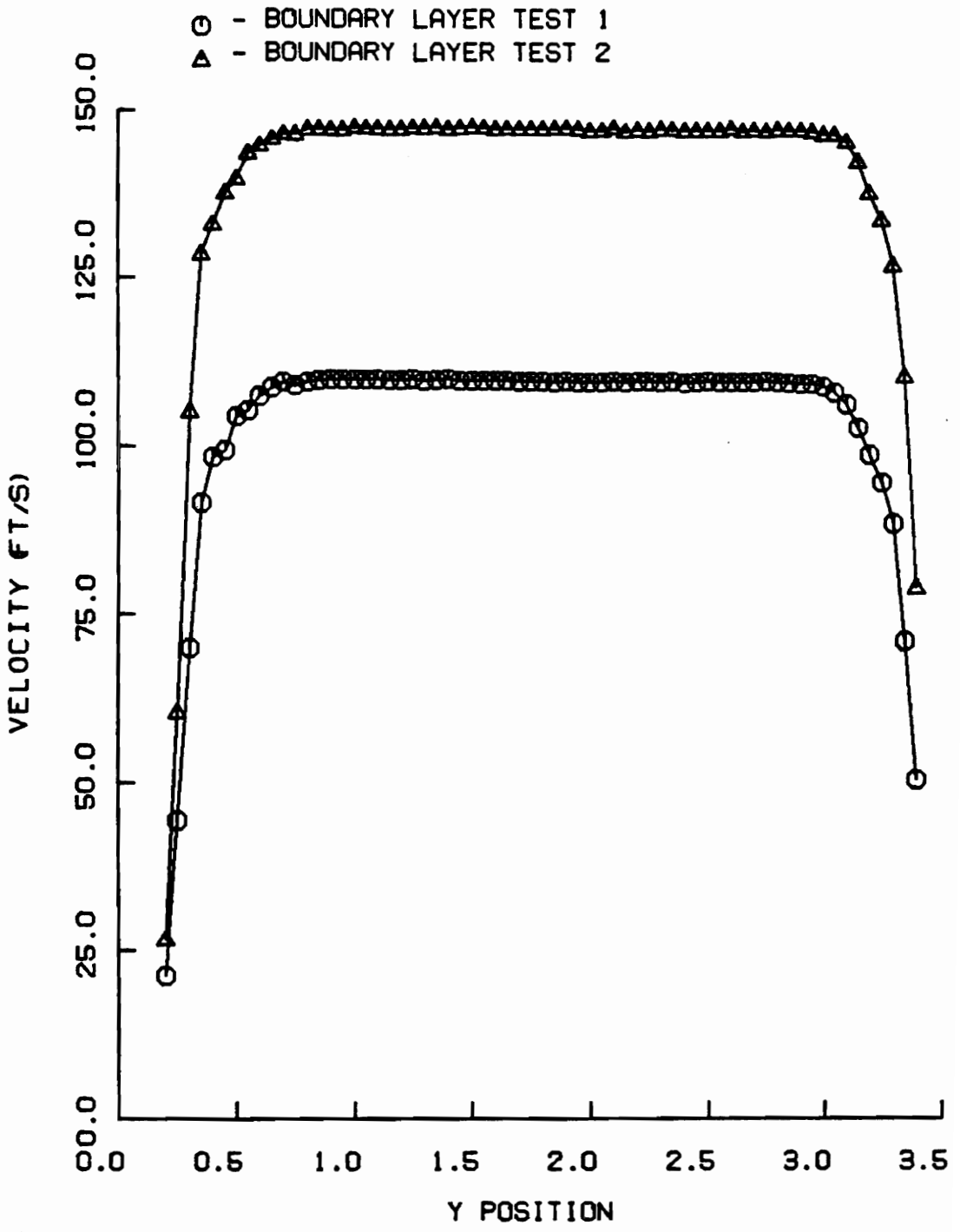

Figure 53. Variable Contraction Nozzle Boundary Layer Results

APPENDIX B

Obtaining aerodynamic performance parameters versus non-dimensional axial velocity requires using the geometry seen in Figure 5. Using the velocity triangle for reversed flow into the rotor, a value of Vx/U can be developed for use with cascade data. Defining:

$$V_{x2} = W_2 \cos(\beta_2)$$

where

$$\beta_2 = \alpha - \gamma$$

gives the quantity V_{x2}. From geometry, the compressor wheel speed U is calculated:

$$U = W_2 \sin(\beta_2) - V_{x2} \tan(\alpha_2)$$

Since V_{x2} and U are known, the flow coefficient Vx/U is known.

Since ω_3 is non-dimensionalized by the inlet relative velocity, W_2, a corrected value ω_{3corr} is presented since ω_{3corr} is the standard loss coefficient for comparison with the flow coefficient, Vx/U. The corrected total pressure loss coefficient is defined as follows:

$$\omega_{3corr} = \omega_3 \left(\frac{W_2^2}{U^2} \right)$$

which is readily calculated from the above values of W_2 and U.

APPENDIX C

Calibration of the split film and 5-hole probes was required for this investigation. The calibration procedures are described and the calibration curves are presented below.

C.1 Split Film

The split film probe works on the principle of heat transfer from a cylinder. Since heat transfer is a function of Reynolds number, measuring the heat transfer from the probe will give an indication of velocity. With two films split at 180 degrees, angular indications can be found knowing that the heat transfer is greater at the leading point of the probe (stagnation point) than at the trailing point of the probe. By calibrating the probe to Reynolds number and angle, the flow velocity and angle can be found.

The split film probe used was a TSI model 1287 connected to a TSI intelligent flow analyzer model IFA-100. The probe had a diameter of 0.14 mm and was operated in constant temperature mode. The IFA-100 uses a 4 resistor bridge with the probe acting as one of the resistors. It also has signal processing capabilities to modify the output of the bridge to meet data acquisition demands. The signal processor was set to a gain of 1, a DC offset of 1 volt, and the low pass filter was set to 4 Hz. The gain and DC offset settings allow maximum resolution when the signal is read by a 5 volt analog to digital converter. The low pass filter rejects frequencies above 4 Hz allowing only steady state measurements to be taken.

The probe was mounted in the center of a calibration section which attached to the second nozzle of the wind tunnel. The calibration section was a constant area device that included a probe mount with the ability to rotate 360 degrees. The angle measurement had an accuracy of 0.1 degrees. To read static pressures, the section had three static pressure taps.

The split calibration was performed at angles ranging from 90 to 450 in increments of 10 degrees, and at 5 different Reynolds numbers (based on probe diameter) ranging from 0 to 447. The split film angles relative to the flow are shown in Figure 54. At each angle and Reynolds number, the probe and IFA-100 produced two voltages, one voltage for each sensor in the split film. These voltages were denoted E1 and E2, respectively.

To construct a calibration curve that represented logically, the voltages were added and subtracted. In theory, adding the voltages gives a value that is a function of Reynolds number only. Subtracting the voltages gives a value that is a function of angle only. Since the world is not perfect, E1+E2 is strongly dependent on Reynolds number and slightly dependent upon angle. Likewise, E1-E2 is strongly dependent upon angle and slightly dependent upon
Reynolds number. This can be seen in Figure 55 and Figure 56.

The curves show Reynolds number and angle as a function of E1-E2 and E1+E2. Reynolds numbers are labeled across the top ranging from 0 to 447. Angles are labeled on the right ranging from 90 to 270 on calibration curve 1, and ranging

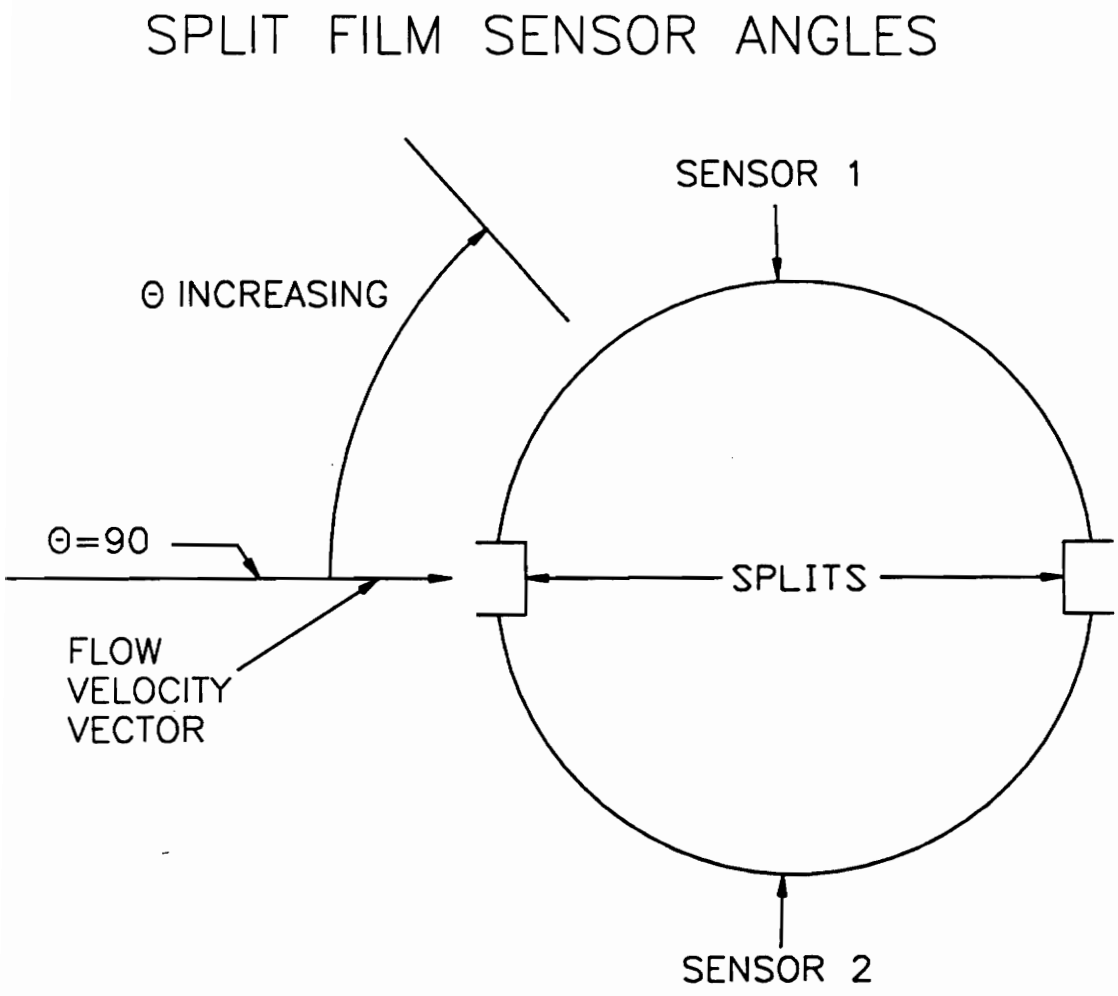

Figure 54. Split Film Probe Angles

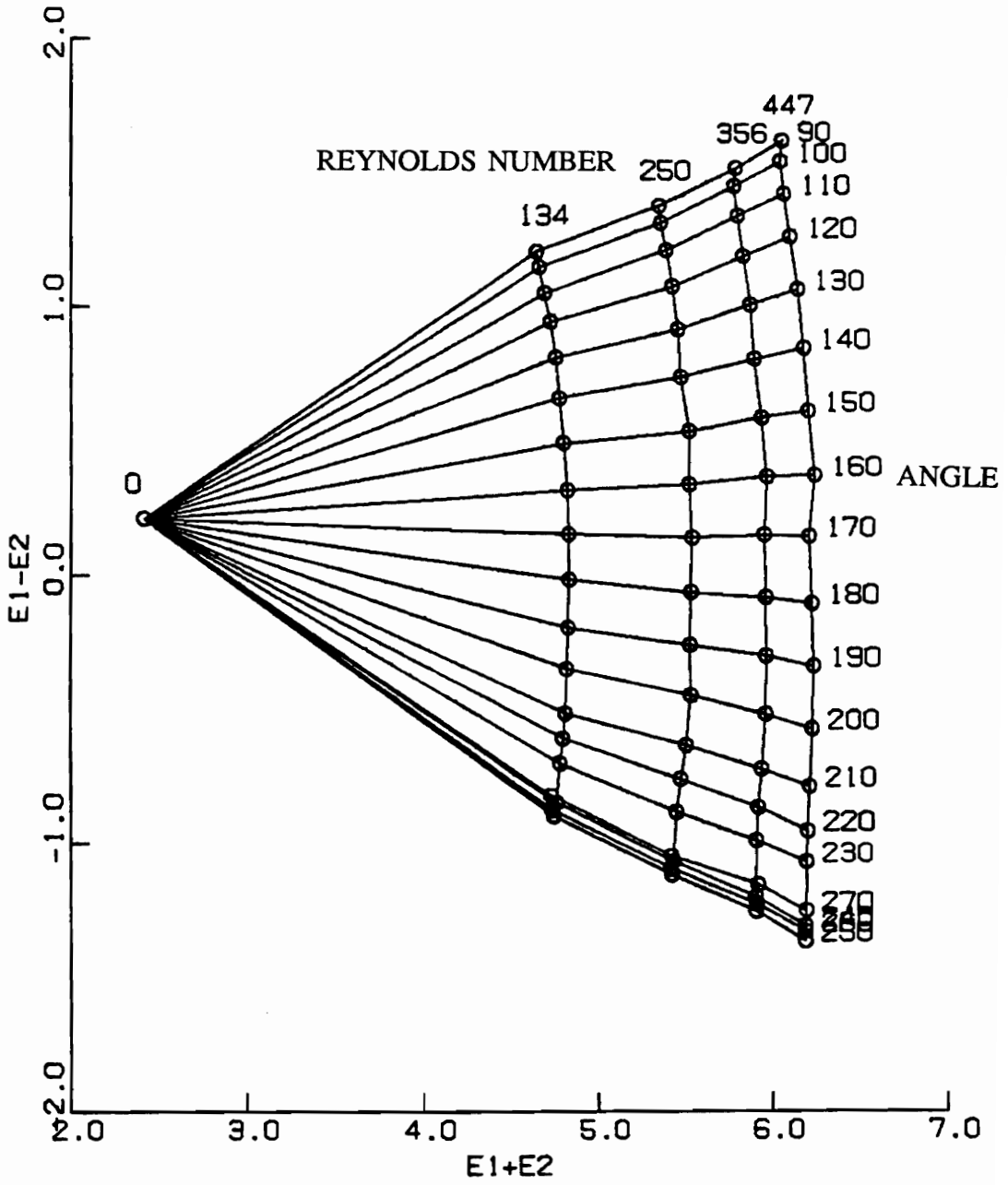

Figure 55. Split Film Calibration Curve 1

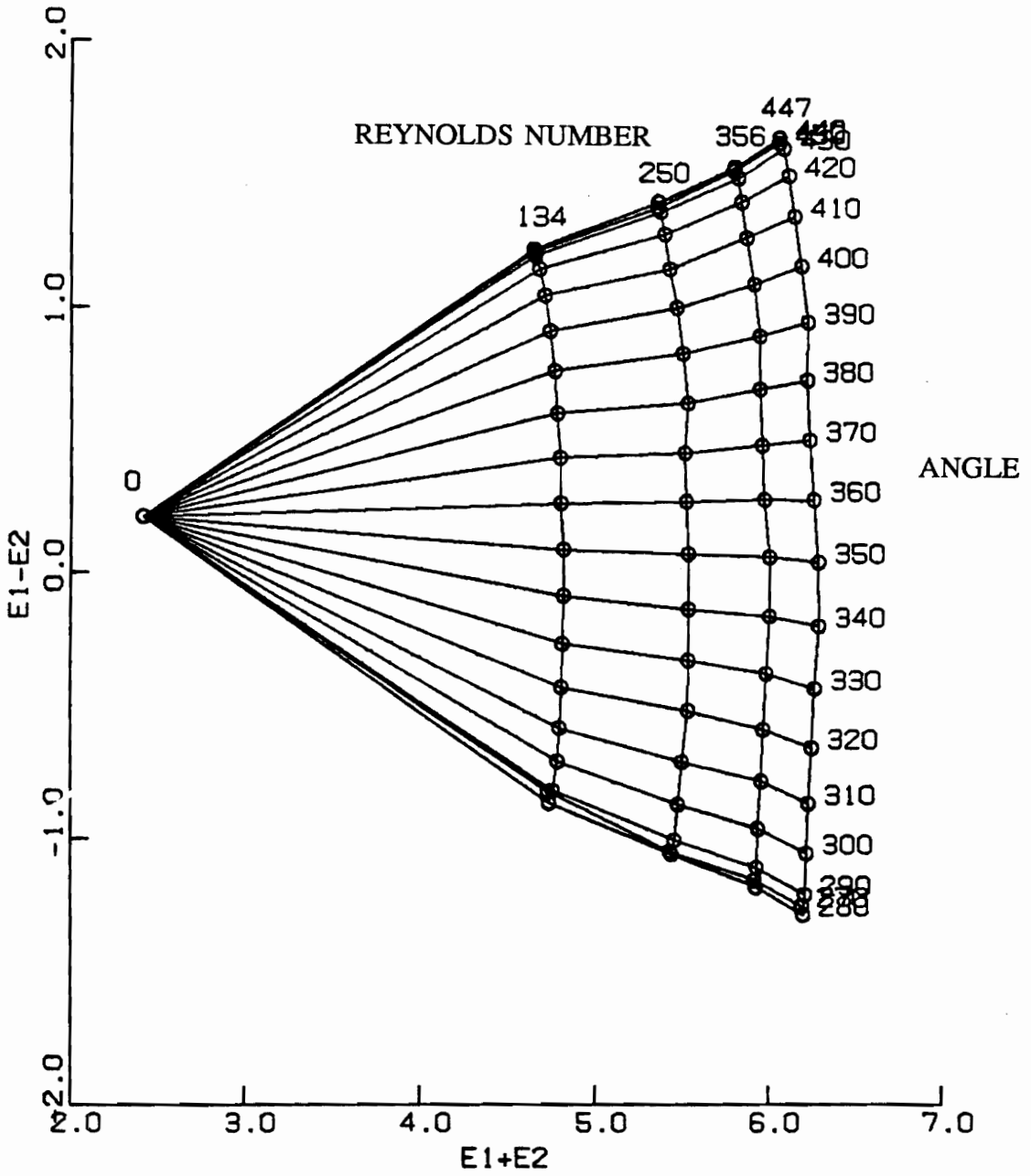

Figure 56. Split Film Calibration Curve 2

from 270 to 450 on calibration curve 2.

C.2 5-Hole Probe

The 5-hole probe, a United Sensor model DC-125, had one total pressure hole and 4 static pressure holes mounted on a goose neck. All pressure measurements were made using one pressure transducer, a Scanivalve model SCSG/D ±5V/VG signal conditioner, and five Scanivalve model W1260/12P-12T fluidic switches. A total of 48 pressure tubes were connected to the 12 ports of four fluidic switches, and the four outputs were connected to the fifth fluidic switch. The output of the fifth switch connected to the pressure transducer. The output of the transducer was linearized by the signal conditioner. The computer read the voltage from the signal conditioner and converted this voltage into pressure.

The 5-hole probe, seen in Figure 57, was calibrated using the same calibration section described in C.1. The calibration was performed at 4 different Reynolds numbers (based on blade chord), and for an angle range of -50 to 50 in increments of 5 degrees. The zero angle on the 5-hole probe was set by operating the wind tunnel and rotating the probe until static taps p_2 and p_3 read the same pressure. At each angle and Reynolds number, the computer read the voltage from the total pressure tap, p_1, and the two static taps in the pitch plane, p_4 and p_5, and the total and static taps in the calibration section,$p_{t\ true}$ and $p_{s\ true}$. The pressures were reduced to a non-dimensional form, Cpt and Cps, defined as:

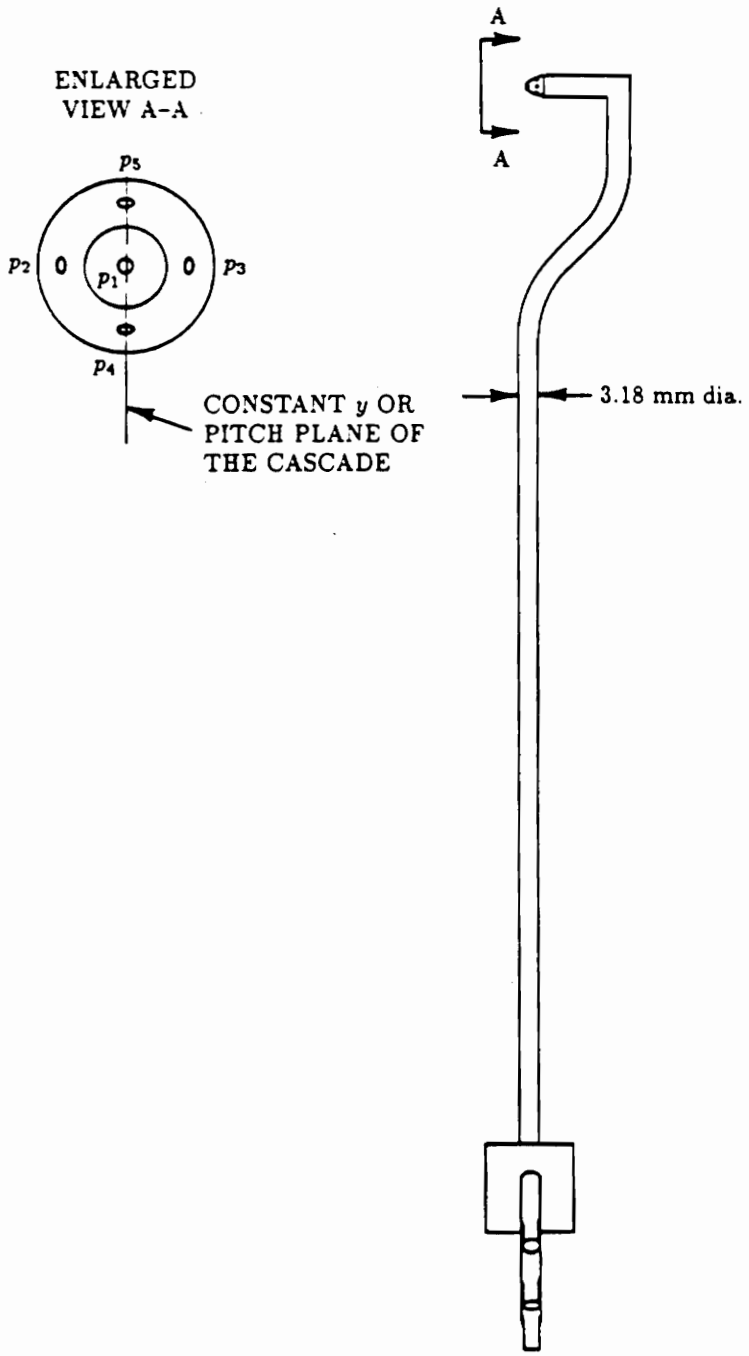

Figure 57. 5-Hole Probe Sketch

$$C_{pt} = \frac{p_1 - p_{t\ true}}{p_1 - p_{s\ ind}} \qquad C_{ps} = \frac{p_{s\ ind} - p_{s\ true}}{p_1 - p_{s\ ind}}$$

where:

$$p_{s\ ind} = \frac{p_4 + p_5}{2}$$

The total and static calibration curves are shown in Figure 58 and Figure 59. As can be seen, the 5-hole probe calibration curves are not influenced by Reynolds number effects.

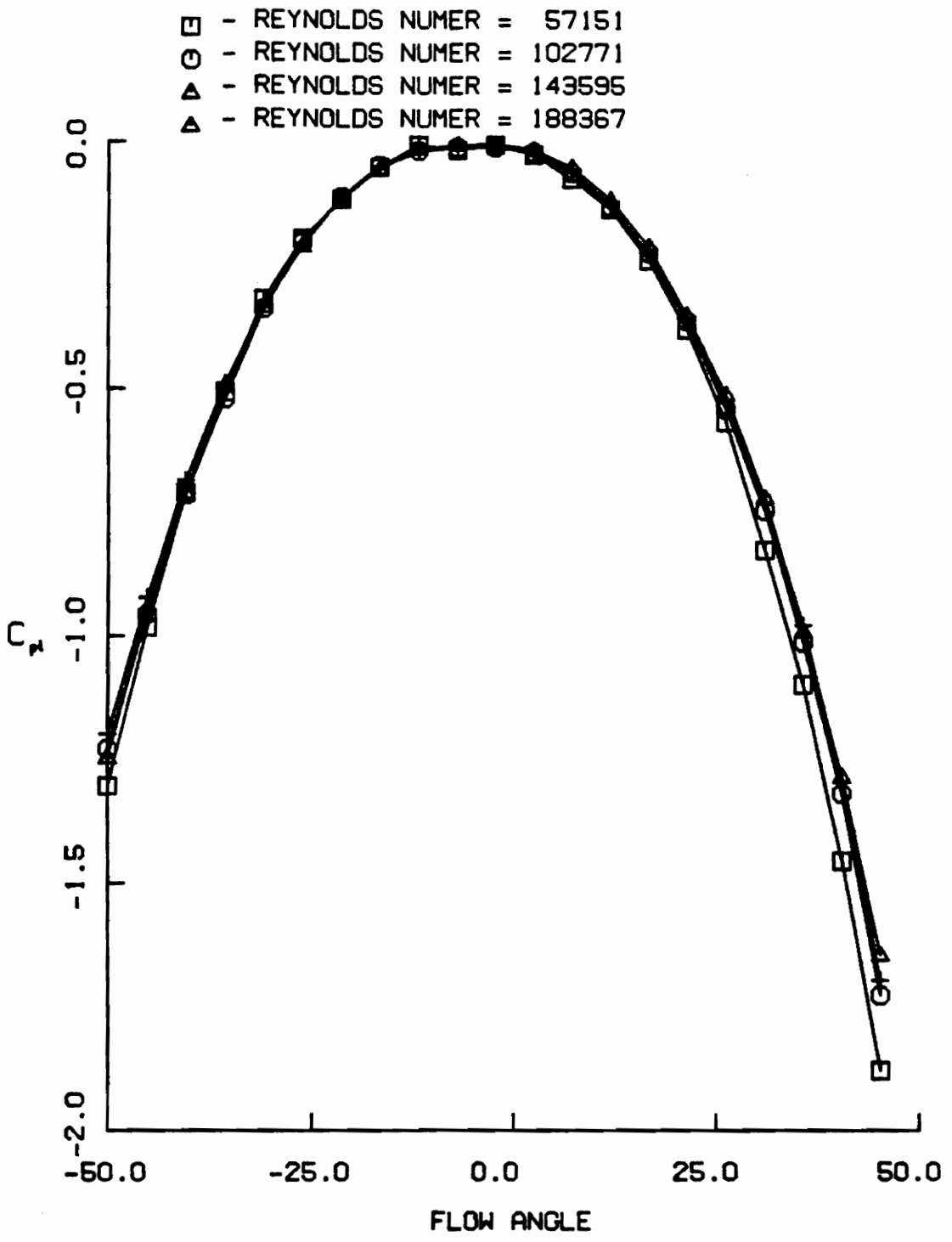

Figure 58. Five Hole Total Pressure Calibration Curve

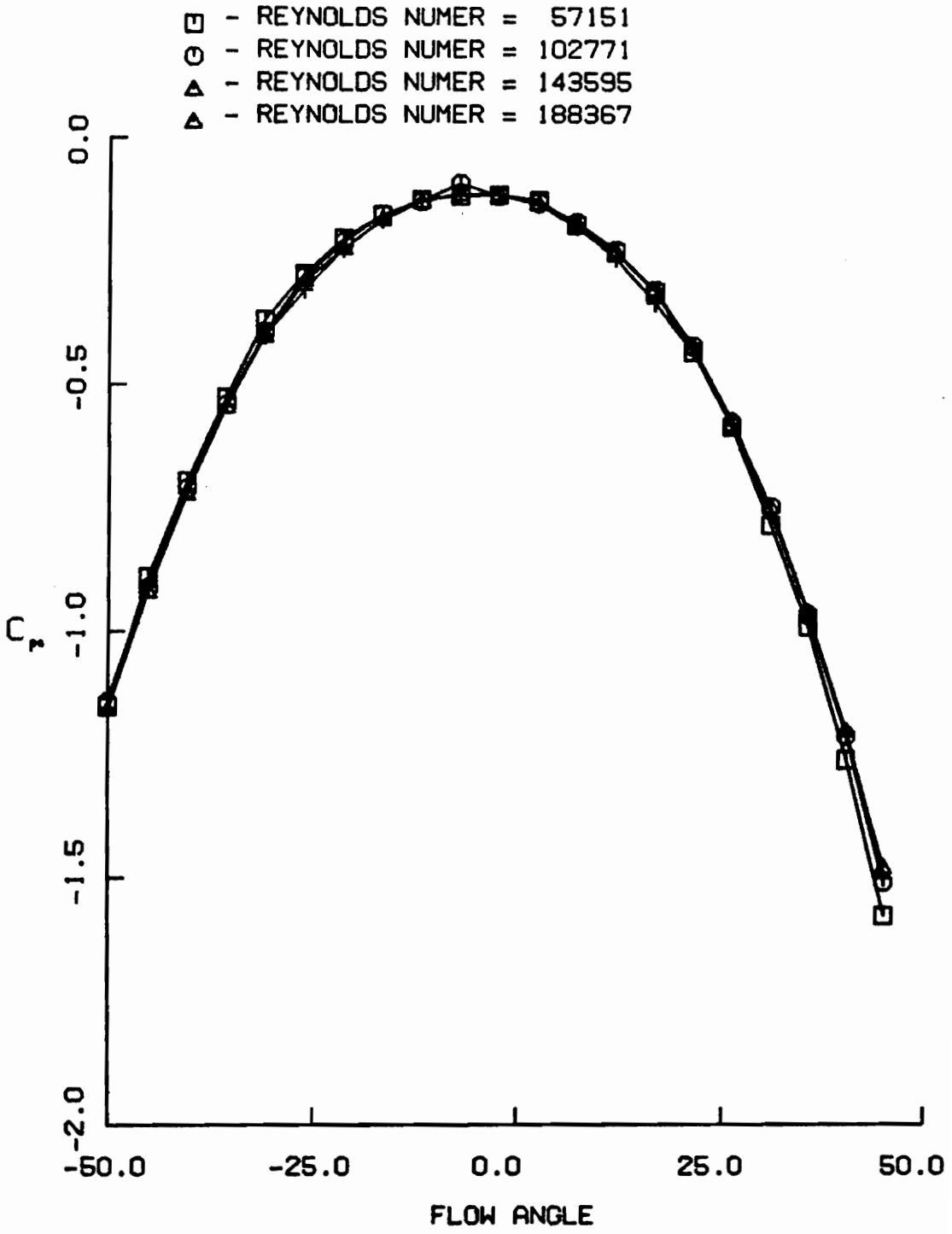

Figure 59. Five Hole Static Pressure Calibration Curve

VITA

The author, James P. Carneal, was born in Richmond, Virginia on September 23, 1965. He graduated from Patrick Henry High School in May, 1983. After graduating with a Bachelor of Science from the Mechanical Engineering Department at Va. Tech in August 1988, he entered Graduate school in the same department. After completion of his Master of Science degree, he plans to go to the beach and have fun, then ride his motorcycle to Phoenix, Arizona with several serious detours. In Phoenix, he plans to design the best gas turbine compressors in the world at Garrett Gas Turbine.

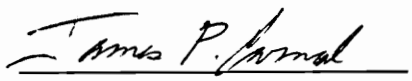

James P. Carneal